

https://dspace.org/

Determining the optimal technique for early detection of broken rotor bars in medium voltage squirrel cage induction motors during operation

Thusi, Lourenco Mafika

2010-04-06T10:12:00Z
http://hdl.handle.net/10539/7940

Downloaded from a DSpace repository. https://dspace.org/

DETERMINING THE OPTIMAL TECHNIQUE FOR EARLY DETECTION OF BROKEN ROTOR BARS IN MEDIUM VOLTAGE SQUIRREL CAGE INDUCTION MOTORS DURING OPERATION

Lourenco Mafika Thusi

A research report submitted to the Faculty of Engineering and Built Environment, University of Witwatersrand, Johannesburg, in partial fulfilment of the requirements for the degree of Master of Science in Engineering.

Johannesburg, 2009

DECLARATION

I declare that this research report is my own, unaided work, except where otherwise acknowledged. It is being submitted as a partial fulfilment for the degree of Master of Science in the University of Witwatersrand, Johannesburg. It has not previously been submitted for any degree or examination in any other university.

……

L.M. Thusi

Signed on this ……day of …….2009

ABSTRACT

Electric motors play a pivotal role in various industrial plant processes for electrical to mechanical energy conversion. As a result their reliability and availability is of utmost importance to industries. The reliability and availability of plant electric motors can be achieved by early detection of any developing fault by performing condition monitoring and preventative maintenance on motors. An important motor failure mode, which has been quite challenging to detect, is cracking and subsequent breaking of rotor bars in induction motors.

The existing condition monitoring techniques are incapable of positively detecting a cracked or single bar problem during operating conditions. Bars have broken, lifting out of the rotor slots and damaging all stator coils, consequently forcing the removal of the motor during plant operation and a complete rewind of the stator.

This research is being conducted to ascertain, from existing conventional techniques, an optimal technique for the detection of a cracked rotor bar or a completely broken single rotor bar in induction motors under operating conditions. Furthermore, it explores non-conventional techniques, which can assist in detection of broken rotor bars.

The report starts by presenting the literature on stator current and axial vibration analysis which are conventional rotor bat detection techniques. Thereafter, the Maxwell 2D simulation results which indicate stator current broken rotor bar detection frequencies are discussed, followed by the experimental measurement results and discussions. The conclusion drawn from the experimental results is that the stator current analysis is, presently, the optimal technique to detect a single broken rotor bar during a medium voltage induction motor operation. The axial vibration analysis is recommended as a secondary monitoring technique to solidify the stator current diagnosis. The shaft voltage analysis is introduced as a non-conventional technique and the shaft voltage results are discussed.

DEDICATION

To my parents V.O. Thusi and J.D. Thusi

ACKNOWLEDGEMENTS

The author would like to thank the following for their guidance, assistance and patience during the course of this research work:

- Professor W.A. Cronje, my supervisor for his assistance and guidance over the duration of this research project.

- Mohamed Ahmed, Eskom CED Electric Machines Consultant for initiating the project to me and together with Associate Professor A. Meyer for assistance, guidance and advise in performing this research project.

- Daniel de Cahna and Kahesh Dhuness, Fellow Postgraduates from University of Witwatersrand and University of Johannesburg respectively, for their assistance in experimental and simulation parts of the project and willingness to give up their time to help me when necessary.

- Eskom - ERID and Eskom - Generation - Arnot Power Station respectively, for their financial assistance in making this project possible and for providing the motors for experimental work on the project.

- Marthinusen & Coutts (M&C) Management and Test Bay personnel, CMM Consultants (Pty) Ltd and Westward Electric Co. (Pty) Ltd for their patience and for assisting in performing the tests and part taking in the investigations.

- Lastly, my family, my wife and friends for helping me through difficult patches and for giving me moral support.

CONTENTS

		Page
DECLARATION……..		(i)
ABSTRACT……..		(ii)
ACKNOWLEDGEMENTS……..		(iv)
CONTENTS……..		(v)
LIST OF FIGURES……..		(ix)
LIST OF TABLES……..		(xii)
LIST OF SYMBOLS……..….		(xiii)
1.	**INTRODUCTION**	**1**
1.1	Broken Rotor Bar Failure Mechanisms……	3
1.2	Structure of the Research Project ……	4
2.	**BACKGROUND ON DETECTION OF BROKEN ROTOR BARS**	**6**
2.1	The Interbar Currents Phenomenon ..……	6
2.2	Factors Influencing Detection of Broken Rotor Bars ……	7
2.3	Axial Vibration Monitoring……..	9
2.4	Thermal Consideration due to Interbar Currents ……..	9
2.5	Other Research Work and Case Studies ……...	10
3.	**BROKEN ROTOR BAR DETECTION TECHNIQUES**	**13**
3.1	Interbar Currents ……	13
3.2	Axial Vibration Monitoring..……..	15
3.3	Stator Current Monitoring..…….	18
3.4	Flux Monitoring……..	21
3.5	The Effects of Load..……..……	22
4.	**MAXWELL 2D SIMULATION OF A BROKEN ROTOR BAR**	**24**
4.1	Induction Motor Simulation Parameters ……	24
4.1.1	Creating the Model…….	26

4.1.2 Materials Setup……. 27
4.1.3 Boundary and Sources Setup……. 28
4.1.4 Setup Solution…… 29
4.1.5 Solution Options…… 30
4.1.6 Motion Setup…….. 30
4.1.7 Signal Processing…….. 31
4.2 Induction Motor Simulation Results …… 31
4.3 Induction Motor Simulation Conclusion…….. 34

5. EXPERIMENTAL VALIDATION TESTING DETAILS AND METHODS 35
5.1 Experimental Test Details ……... 35
5.2 Experiment Measuring Instruments …….. 37
5.2.1 Current Transducer……... 37
5.2.2 Vibration Sensors…… 39
5.2.3 Speed Sensor: Tachometer……. 40
5.3 Data Acquisition and Processing ……... 41
5.3.1 dSpace: DS1104 R&D Controller Board…… 41
5.3.2 Signal Processing…….. 43
5.3.3 Selection of FFT parameters……. 46

6. INDUSTRIAL EXPERIMENTAL RESULTS AND DISCUSSION 48
6.1 Experiment Results Introduction ……. 48
6.2 Stator Current Analysis ……. 48
6.2.1 Motor A Stator Current Analysis…… 50
6.2.2 Motor B Stator Current Analysis…… 57
6.3 Axial Vibration Analysis..……. 60
6.3.1 Motor A Axial Vibration Analysis…… 60
6.3.2 Motor B Axial Vibration Analysis…… 65
6.4 Other detection technique: Shaft Voltage Analysis…..…….. 68
6.4.1 Motor A Shaft Voltage Analysis…….. 69

6.4.2 Motor B Shaft Voltage Analysis……. 75
6.5 The Effects of Load..……. 76
6.5.1 Motor A Load Effects Comparison……. 76
6.6 Experiment Results Summary…… 78
6.7 Experiment Results Conclusion …… 79

7. CONCLUSION AND RECOMMENDATIONS 80
7.1 Research Report Summary…….. 80
7.2 Research Report Conclusion…… 81
7.3 Recommended Future Work……. 82

APPENDIX A: MAXWELL 2D: INDUCTION MOTOR SIMULATION 84
A.1 General Procedure for creating and solving a 2D Model…….. 84

APPENDIX B: DS1104 R&D CONTROLLER BOARD SPECIFICATIONS 88

APPENDIX C: DATA PROCESSING MATLAB CODES 90
C.1 The Matlab FFT Function used for data processing [47]…… 90
C.2 Measured Signal Processing…….. 91

APPENDIX D: ADDITIONAL THEORETICAL AND INDUSTRIAL MEASUREMENTS RESULTS 93
D.1 Stator Current Analysis…… 93
D.2 Axial Vibrations Analysis……. 96

APPENDIX E: ADDITIONAL BROKEN ROTOR BAR DETECTION INSTRUMENTS 98
E.1 CSMeter…… 98
E.2 CSI 2130 Machinery Health Analyser…….. 101
E.3 Current Clamps…… 102
E.4 Flux Coil…… 102

APPENDIX F: CMM CONSULTANTS EXPERIMENT REPORT **105**

APPENDIX G: IRIS POWER EXPERIMENT REPORT **117**

REFERENCES **131**

LIST OF FIGURES

		Page
3.1	Kerszenbaum and Landy's model of the broken bar region.....	14
3.2	Production of axial force model by Muller……..…...	16
4.1	The geometric model of the simulated induction motor…….	26
4.2	Maxwell 2D model materials description……..	27
4.3	Maxwell 2D simulation mesh……..	30
4.4	Simulated stator current at the 5th harmonic……...	31
4.5	Simulated stator current at the 17th harmonic……..…..	32
4.6	Normalised simulated stator current results……	33
5.1(a)	Half broken rotor bar……...	36
5.1(b)	One fully broken rotor bar……...	36
5.2	LEM-flex RR3030 AC current probe…….	38
5.3	Connection of accelerometers for vibration measurements…….	39
5.4	Digital Tachometer RM-1501 for speed measurement…….	40
5.5	An overview of the architecture and functional units of the DS1104	41
5.6	dSpace Control Desk setup for experimental work……	42
5.7	Summarised signal processing process …….	45
6.1	Motor A stator current at the1st harmonic (50 Hz)……..	50
6.2	Motor A stator current at the 3rd harmonic (150 Hz)……..	51
6.3	Motor A stator current at the 5th harmonic (250 Hz)……..	51
6.4	Motor A stator current at the 7th harmonic (350 Hz)……..	52
6.5	Motor A stator current at the 9th harmonic (450 Hz)……..	52
6.6	Motor A stator current at the 11th harmonic (550 Hz)……	53
6.7	Motor A stator current at the 23rd harmonic (1150 Hz)…….	53
6.8	Motor A stator current at the 25th harmonic (1250 Hz)……..	54
6.9	Motor A stator current at the 43rd harmonic (2250 Hz)……..	54
6.10	Normalised stator current for Motor A at different harmonics……..	55
6.11	Motor B stator current at the 1st harmonic (50 Hz)……..	57
6.12	Motor B stator current at the 5th harmonic (250 Hz)……..	57
6.13	Motor B stator current at 11th harmonic (550 Hz)…….……....	58

6.14 Motor B stator current at 23rd harmonic (1150 Hz)……. 58
6.15 Motor B stator current at 25th harmonic (1250 Hz)……. 59
6.16 Motor A 1st group of axial vibrations fault frequencies…….. 61
6.17 Motor A 2nd group of axial vibrations fault frequencies……. 61
6.18 Motor A 3rd group of axial vibrations fault frequencies…….. 62
6.19 Motor A 4th group of axial vibrations fault frequencies……. 62
6.20 Motor A 5th group of axial vibrations fault frequencies…….. 63
6.21 Motor A 6th group of axial vibrations fault frequencies…….. 63
6.22 Motor A 7th group of axial vibrations fault frequencies…….. 64
6.23 Motor A 8th group of axial vibrations fault frequencies…….. 64
6.24 Motor A 9th group of axial vibrations fault frequencies…….. 65
6.25 Motor B 4th group of axial vibrations fault frequencies…….. 66
6.26 Motor B 5th group of axial vibrations fault frequencies…….. 67
6.27 Motor A shaft voltage at 50 Hz (1st harmonic)……. 69
6.28 Motor A shaft voltage at 150 Hz (3rd harmonic)…….. 69
6.29 Motor A shaft voltage at 250 Hz (5th harmonic)…….. 70
6.30 Motor A shaft voltage at 350 Hz (7th harmonic)……. 70
6.31 Motor A shaft voltage at 450 Hz (9th harmonic)…….. 71
6.32 Motor A shaft voltage at 1050 Hz (21st harmonic)…….. 71
6.33 Motor A shaft voltage at 1350 Hz (27th harmonic)…….. 72
6.34 Motor A shaft voltage at 1950 Hz (39th harmonic)…….. 72
6.35 Motor A shaft voltage at 2250 Hz (45th harmonic)…….. 73
6.36 Motor A shaft voltage at 2850 Hz (57th harmonic)…….. 73
6.37 Normalised shaft voltage for Motor A at different frequencies……. 74
6.38 Motor B shaft voltage at 150 Hz (3rd harmonic)……. 75
6.39 Motor B shaft voltage at 450 Hz (9th harmonic) …….. 75
6.40 (a) and (b): Stator current at different motor loads…….. 76
6.41 (a) and (b): Stator current for Motor A at different loads……. 77
6.42 (a) and (b): Axial vibrations at different motor loads…… 77
6.43 (a) and (b): Shaft voltage at different motor loads…… 78

A.1 XY and RZ geometric model planes……. 85
A.2 Flow diagram of creating and solving a Maxwell 2D Model……. 87
E.1 CSMeter…… 99
E.2 CSI2130 Machine Health Analyser…….. 101
E.3 Current Clamps…… 102
E.4 Flux Coil…… 102

LIST OF TABLES

Page

3.1 Axial vibration frequencies due to broken rotor bars when interbar currents are present by Muller…… 17

4.1 Arnot Power Station ID Fan Induction Motor Dimensions……. 25

4.2 Material Set-up of the Simulated Motor……..……..….. 28

4.3 Comparison of theoretical and simulated stator currents for s = 0.004 …… 32

5.1 Arnot Power Station ID Fan Induction Motor Specifications used for experimental measurements……. 36

5.2 LEM-flex RR3030 Specifications…….. 38

5.3 Digital Tachometer RM-1501 Specifications…… 40

6.1 Theoretical calculation of stator current fault frequencies for s = 0.004 …… 49

6.2 Stator current rotor bar fault frequencies as in [40]…… 50

6.3 Stator current for Motor A at 65 %…… 56

6.4 Motor A theoretical results of axial vibrations by Muller [26]…… 60

6.5 Shaft voltage rotor bar detection frequencies…..…… 68

B.1 The data sheet of the DS1104 R&D Controller Board…….. 88

D.1 Theoretical Stator Current for 65% Load at s = 0.0047…… 94

D.2 Theoretical Stator Current for 70% Load at s = 0.0053…… 95

D.3 Theoretical Axial Vibration at 65% Load with s = 0.0047……..….. 96

D.4 Theoretical Axial Vibration at 70% Load with s = 0.0053……. 97

LIST OF SYMBOLS

Arnot	Arnot Power Station is one of the Eskom: Generation: Power Station built in 1956 and situated in Middelburg, Mpumalanga.
B	flux density along a conductor
EMF	electromagnetic field
EPRI	Electric Power Research Institute
ESKOM	a major Electric Power Utility Corporation in South Africa
f	supply frequency ≈ fundamental frequency ≈ line frequency
f_{sb}	frequencies of sidebands due to broken rotor bars
f_{lsb}	lower sideband frequency
f_{usb}	upper sideband frequency
f_b	pole pass frequency
f_{slip}	slip frequency
$I_b(x)$	bar current distribution along the length bar
I_c	total interbar current flowing into the core
I_n	current in a healthy bar
I_t	total current flowing in the broken bar and two adjacent bars
k	1,2,3…n
l	length of the core
Majuba	Majuba Power Station is one of the Eskom: Generation: Power Station built during 2003 and situated in Volksrust, Mpumalanga.
MCSA	Motor Current Signature Analysis
MMF	magnetomotive force
n	estimate of the number of broken bars
N	average dB difference between the upper and lower sidebands and the supply component.
OEM	Original Equipment Manufacturer
p	pole-pairs
q_a	flux density harmonic in electrical measure

q_b	interbar current harmonic in electrical measure
s	slip frequency
R	number of rotor slots
$V_A(x)$	differential voltage drops along healthy bar
$V_B(x)$	differential voltage drops along broken bar
X	axial position along the rotor core from healthy side
Z_b	bar impedance
Z_c	interbar impedance

CHAPTER 1

INTRODUCTION

Electric motors play a pivotal role in various industrial plant processes for electrical to mechanical energy conversion. Industrial medium voltage electric motor applications mainly include driving pumps, conveyors, fans, mills and compressors. The induction motor is the most commonly used motor type of its strength, reliability, relatively high efficiency and lower maintenance demand.

An induction motor comprises of two essential components, a stator and a rotor. This research focuses on the rotor component of an induction motor. The rotor is composed of thin-slotted, highly permeable steel laminations that are pressed onto a shaft. There are two types of rotors: a squirrel cage rotor and a wound rotor but this research focuses on a squirrel cage rotor because of its construction. The squirrel cage rotor has conductors in the form of bars in the rotor slots and the bars are shorted together at each end of the rotor by an end ring to which the conductors are attached.

In an induction motor, the rotor rotates at a speed lower than the synchronous speed of the revolving field. The difference between the rotor speed and the synchronous speed is called the slip speed. The slip speed is commonly expressed in terms of slip, which is a ratio of the slip speed to the synchronous speed. The slip plays an important role in the diagnosis of faults in an induction motor, as it will be indicated in the analysis of results in this research.

Each motor is designed for a specific lifespan. Any failure during the stipulated lifespan has high financial implications in terms of loss of production and the cost of repairs. In an industry like Eskom, from which this research was initiated, medium voltage induction motors are mostly used in power generating stations and form the core of generating plant processes. Failure of some motors,

namely induced draught fan, forced draught fan and boiler feed pump motors lead to loss of power generation. Other motors, which are mill, primary air fan and ash pump motors operate on a redundant basis where one motor is on standby during normal operation but failure of more than one motor in the same generating unit can lead to loss of power generation. With Eskom presently, especially during winter seasons, experiencing high demand resulting in power shortages, generating plants reliability and availability is of utmost importance.

Reliability and availability of plant electric motors can be achieved by early detection of any developing fault by performing condition monitoring and preventative maintenance on motors. An important motor failure mode, which has been quite challenging to detect, is cracking and subsequently breaking of rotor bars in induction motors. Haji and Toliyat [10] state that broken rotor bar and end ring faults (rotor failures) account for 5-10% of the induction motor failures.

The existing condition monitoring techniques are unable to positively detect a cracked or single bar problem during operating conditions and bars have broken, subsequently lifting out of the rotor slots and damaging all stator coils. This forces the removal of the motor during plant operation and a complete rewind of the stator.

This research was conducted to ascertain from existing conventional techniques, an optimal technique for the detection of a cracked rotor bar or a completely broken single rotor bar in induction motors under operating conditions. Furthermore, it explores non-conventional techniques and highlights broken rotor bar condition monitoring guidelines which can assist in performing measurements in industries.

In addition, this research addresses the following questions raised in [1]:

- What equipment exists to detect broken rotor bars?

- Can the technique detect a cracked and one broken rotor bar on-line and immediately or periodic non-intrusive assessments are required?

1.1 Rotor Bar Failure Mechanisms

The frequent starting of a motor places the heaviest stress on the rotor bars because bars are carrying the highest current since the rotor is running at much lower than synchronous speed. The high currents cause heating and expansion of the bars relative to the rotor itself, and differences in electrical resistance of the individual bars result in uneven heating and uneven expansion. This leads to cracking of the joints where bars are joined to the short ring. This rotor bar failure phenomenon is called cyclic thermal stressing. Also, when the rotor is heated, the endring expands at a faster rate than the rotor core, creating additional stressing of the joint [27].

In addition the causes of bar cracks or breaks can be attributed to following reasons as indicated by Müller and Landy [26 - 27]:

- Bars in the region between the core and endring are exposed to large accelerating and decelerating forces. These centrifugal forces place excessive stress on the bars in the unsupported region – causing fatigue in the joint between the bar and the endring.
- When the motor is started, the current migrates to the top of the bar due to skin effect. This current migration creates temperature gradient over the depth of the bar because the top of the bar heats faster than the bottom of the bar. This uneven expansion stresses the joints at the endrings, and can cause the bar to separate from the endring.
- Manufacturing defects are a cause of broken rotor bars. Poor brazing of the bat onto the endring results in a weak joint. A weak joint along with the heating of the bar and large centrifugal forces can result in a cracked bar. A further cause of broken rotor bars due to manufacturing defects is loose rotor

bars. Rotor bars that are loose in the rotor core also place excessive stress on the endring joint.

1.2 Structure of the Research Report

Chapter 2 highlights previous researches conducted on detection of broken rotor bars which has assisted in better understanding of the existence of interbar currents and axial forces, factors influencing early detection of broken rotor bars and development of broken rotor bar detection techniques.

Chapter 3 discusses the literature and analysis of different broken rotor bar detection techniques. These detection phenomena originated from the researches presented in Chapter 2. The broken rotor bars identifying frequencies in each technique are presented.

Chapter 4 presents modelling of a broken rotor bar simulation using Maxwell 2D. The simulation was performed to investigate the induction motor stator current that is how the sidebands change in a single broken bar rotor with respect to a healthy rotor.

Chapter 5 discusses the experimental work conducted to validate the literature and practical implementation of the techniques. This chapter explains the measuring process and the set up of the equipment used in the experimental work, capturing and analysis of data.

Chapter 6 presents the experimental results from the industrial tests performed on the research with discussions of measurements taken. Finally, Chapter 7 presents the conclusion and recommendations on the effective technique on detection of broken rotor bars during operation.

The author hopes that the research report recommendations assist in early detection of a cracked and a single broken rotor bar on-line during operation without intrusion to the motor.

CHAPTER 2

BACKGROUND ON DETECTION OF BROKEN ROTOR BARS

A lot of research work and case studies have been performed and are still being performed on detection of broken rotor bars but the main problems seem to be analysis of the measurements and correct diagnosis especially for a cracked and one broken rotor bar. It is important to note that most techniques seem to detect broken rotor bars when many of the rotor bars have already broken, this is not effective as the damage is quite severe at that stage.

2.1 The Interbar Currents Phenomenon

Kerszenbaum [14, 15, 16] together with Landy introduced the concept that in an induction motor with rotor bars not insulated to the rotor core, interbar currents exist when there is a broken rotor bar. In the research, the following assumptions were made:

- The laminar currents flow only between the broken bar and the two immediately adjacent bars. (This assumption is valid when the endring impedance represents only a small part of the total secondary impedance, as is usually the case with large machines).
- The voltages induced in the three bars (broken bar and adjacent bars) are equal in magnitude and are in phase with one another. (This is valid when the number of rotor slots per pole is relatively high).
- The interbar impedance is mostly resistive at the frequencies dealt with. (This fact was verified by measurement).
- The end ring impedance between the bars is negligible.
- The portion of the bars between the end ring and the core is disregarded.

Kerszenbaum developed a term which describes the distribution of currents in an induction motor having a broken bar and experimentally showed that the

magnitude of the current flowing into the broken bar and the magnitude of the interbar currents varies with the slip. The theory was later expanded by Muller [26] who derived an equation for the interbar current density entering the rotor core. The derivation of the equations is discussed in details in Chapter 3.

2.2 Factor Influencing the Detection of Broken Rotor Bars

The early detection of broken rotor bars is mainly affected by the rotor and stator geometrical nonuniformities or asymmetries. Kliman *et.al.* [19] named these asymmetries as rotor quality, cage misalignment, variation of cage conductivity, bearing misalignment and magnetic orientation of the laminations. These asymmetries may create airgap disturbances which, as far as its fundamental field is concerned, cannot be distinguished from the broken bar effects. By investigating the airgap flux Kliman *et. al.* [19] showed that the magnitude of the line frequency sidebands due to asymmetries might be comparable to or larger than those due to broken rotor bar in the same motor. But the magnitudes of the asymmetry components decay much more rapidly in higher harmonics, than those of broken rotor bar.

Walliser [40] under the supervision of Landy undertook a research to investigate factors influencing detection of broken rotor bars. Walliser revisited the work done by Kliman *et. al.* [19] by showing the influences of the stator winding layout, the presence of other rotor asymmetries, the rotor inertia, and lastly the presence of interbar currents.

As it is not possible to measure the rotor bar current during operation, the fault measurements are taken from the stator winding. The fields produced by the fault will result in a flux linking with the stator windings, which will induce an EMF and consequently current in the stator winding. The layout of the stator windings will cancel the response to certain harmonic components that would normally exist in the airgap of the machine due to the fault. The magnitudes of the

harmonics that are able to induce currents in the stator are also modified by the stator structure.

Walliser [40] stated that due to short chording in the stator winding, which is done to reduce harmonic effects, the EMF the fault harmonics can induce in the stator can be reduce by a factor, known as the chording factor. Also the distribution of coils in one phase of the stator winding will result in the EMF, the fault harmonics can induce, requiring to be multiplied by a factor, called the distribution factor. Lastly, the other factor is the harmonic differential leakage coefficient. This is due to the fact that each harmonic voltage induced into the stator by the fault field, produces in turn its own set of harmonics. These harmonics act as an extra reactance to the induced current, and will thus reduce its magnitude.

The influence of the presence of interbar was demonstrated in [40] by testing an induction motor with a healthy cage, one broken uninsulated bar (interbar currents flow) and insulated bar (no interbar currents). Theoretically and experimentally, it was shown that interbar currents reduce the magnetic imbalance brought by a broken rotor bar and consequently the sidebands produced in the stator current spectrum. This then makes early detection of broken rotor bars more difficult especially if monitoring sidebands around the fundamental as sidebands may be reduced to levels due to other factors.

Kliman *et. al.* [19] then later Walliser [40] after further examination of the above mentioned factors recommended monitoring higher harmonic amplitudes asymmetries in the spectrum in conjunction with the sidebands around the fundamental, for correct diagnosis or early detection of broken rotor bar in a motor.

Another factor influencing the early detection broken rotor bars is the lack knowledge, by condition monitoring personnel on industrial plants, where

induction motors are being operated, on detection of broken rotor bars. The following questions were raised in Eskom [1]:

(i) What techniques and equipment exist to detect broken rotor bars on-line?

(ii) How to perform the rotor bar detection techniques i.e. where to measure to get optimum results?

(iii) What indicates a broken bar on any techniques' spectrum?

(iv) How often to perform broken rotor bar condition monitoring?

These questions prompted and are the basis of this research. The research tries to bridge the gap between researched detection techniques and utilization of these techniques in industrial plants. The author hopes all the research questions are answered and the gap will be bridge by this research.

2.3 Axial Vibration Monitoring

After realising that Kerszenbaum [15] and Hop [11] could not explain the origin of the axial vibrations that existed in a motor with broken rotor bars, Muller [26] under the supervision of Landy undertook a research to identify the origin of the axial forces. Mullers' research showed that interbar currents in the rotor do in fact produce an axial force at specific frequencies. The theory was verified by experimental measurements on several different motors and with this consolidated the technique of measuring these frequencies in the axial vibration as a reliable method to detect broken rotor bars.

The expressions for these axial vibration frequencies are discussed in Chapter 3.

2.4 Thermal Consideration due to Interbar Currents

One of the major factors which cause rotor bar failures is thermal stress but before Zachas [42] very little research work had been done to examine the effects or existence of heating in a motor with a broken rotor bar especially when

interbar currents are present. Zachas investigated the relationship between interbar currents and the thermal effects that might occur as a result of these currents.

Zachas derived calculations and developed models to predict the temperature distribution for various conditions a motor will be subjected to. Through experiments, a good correlation between heating and interbar currents was achieved and a conclusion was made. The conclusion drawn was that the heating follows the same distribution as the interbar currents and is concentrated at the unhealthy side of the broken rotor bar.

2.5 Other Research Work and Case Studies

EPRI [48] initiated research projects to study motor problems and how they can be detected, which provided intelligence that contributes to motor condition monitoring and a predictive maintenance strategy. One aspect of the research projects was detection of broken rotor bars with one rotor bar cut by 50%, same bar cut 100%, a second bar, located 180º degrees from the first bar, cut 100%, and lastly two additional bars were cut 100%. The two additional bars were located adjacent to the original cut bar, making four total bars cut. Each motor was run at 0%, 50%, and 100% and back down to 50% of rated load.

The tests performed or data collected on each motor were vibration data, motor current signature analysis data, power signature data and flux data which were done on-line at each of the data points with the motor circuit analysis data being collected off-line.

The EPRI research project results were analysed by each utility analyst for their respective equipment and also by the equipment vendors. A vendor and utility analyst was given a copy of only their data, without any information about the specific fault that were induced in each motor. The results, recommendations

and conclusions of the research project may be examined by obtaining Electric Motor Predictive Maintenance Program, TR-108773-V2 Final Report [48] but it must be highlighted that the research findings show that it is possible to perform early detection of broken rotor bars.

McCully and Landy [22] evaluated the on-line condition monitoring techniques for detecting broken rotor bars, by evaluating both current and vibration signals and taking cognisance of interbar currents. The conclusion on the evaluation was that measurement of both current and vibration signals taking cognisance of interbar currents can provide an accurate diagnosis of the condition of the bars in large squirrel cage induction machines.

Thomson and Fenger in [38, 39] discuss the development of a tool to detect faults in an induction motor using current signature analysis. Furthermore, using the developed tool performs case studies by performing current analysis on different motors. The tool was developed to include the following crucial features:

- Unambiguous diagnosis of a fault over a range of motor faults.
- Correct estimation of the slip for any given load conditions for a range of motor designs and power ratings.
- Clear discrimination between unique current signature patterns caused by a fault and any current components induced due to normal characteristics of the drive system.
- Current components caused by the effect of mechanical load must be reliably diagnosed since they can be misinterpreted as components from broken rotor bar.
- The goal is to eliminate the need for an expert to interpret the acquired data by applying reliable, advanced diagnostic algorithms to the spectra.

The tool developed in the research by Thomson and Fenger is the CSI Meter. The CSI Meter was used in the research and more detailed specifications are included in Appendix E.

CHAPTER 3

BROKEN ROTOR BARS DETECTION TECHNIQUES

3.1 Interbar Currents

As soon as a crack develops, the resistance of that bar increases, increasing its heating, and consequently worsening the crack. At the same time, the adjacent bars experience increased currents because of the reduced current in the cracked or broken bar.

Kerszenbaum and Landy [14, 15, and 16] proved that interbar currents exist when a rotor bar is broken in large copper bar squirrel cage induction motors with uninsulated rotor bars. Interbar currents can flow in the laminated core, perpendicular to the bars.

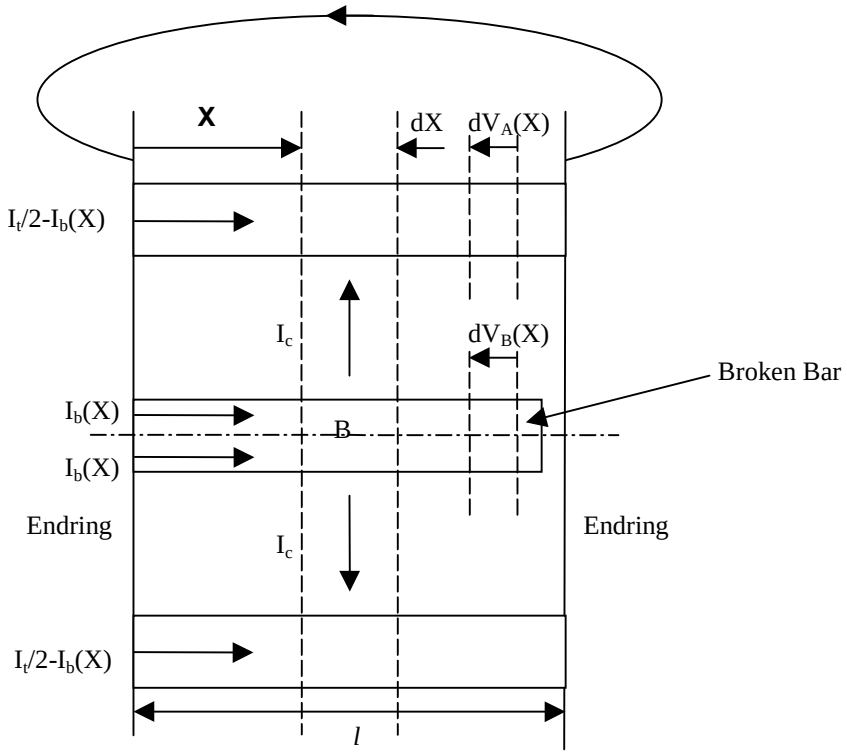


Figure 3.1: Kerszenbaum and Landy's model of the broken bar region [14]

The model assumes that the break occurs along the bar between the core and the endring. This is justified by realising that the most likely region of failure (weakest mechanical point) in the rotor is the joint between the bar and endring. Other assumptions, used to derive the expression for current distribution in the broken rotor bar, have been mentioned in the previous chapter in section 2.1.

The current distribution in the broken bar is based on the impedance distribution rather than the voltage distribution. This is justified by the assumption that the voltage across all three, i.e. the broken bar and the two adjacent bars, is constant. In the model, the total current flowing in all three bars is expressed by I_t with the current flowing in a healthy bar being I_n.

The current distribution along the broken bar length is thus given by:

$$I_b(x) = \frac{I_n}{2}\left[1 - \frac{\cosh(\lambda x)}{\cosh(\lambda l)}\right] \tag{3.1}$$

The magnitude and distribution of current in the broken bar depends on λ. λ is defined as the ratio of bar impedance (Z_b) to interbar impedance (Z_c). But due to the assumption that Z_c is mostly resistive at relevant frequencies, λ then becomes:

$$\lambda = \sqrt{3\left|\frac{Z_b}{R_c}\right|} \tag{3.2}$$

In order to determine the current entering the broken bar Kerszenbaum [14] considered the current distribution given in eq. 3.1 at x = 0. The current entering the broken bar thus becomes:

$$I_{bb} = 2I_b(0) = I_n\left[1 - \frac{1}{\cosh(\lambda l)}\right] = I_n\left[1 - \frac{1}{\cosh \lambda}\right] \tag{3.3}$$

The bar length is normalised since x = 0 and is omitted from the equation.

3.2 Axial Vibration Monitoring

The interaction between the stator flux and the interbar current produce an axial force. The interbar currents and stator flux both contain not only fundamentals, but also harmonic components, which interact with each other to produce a force.

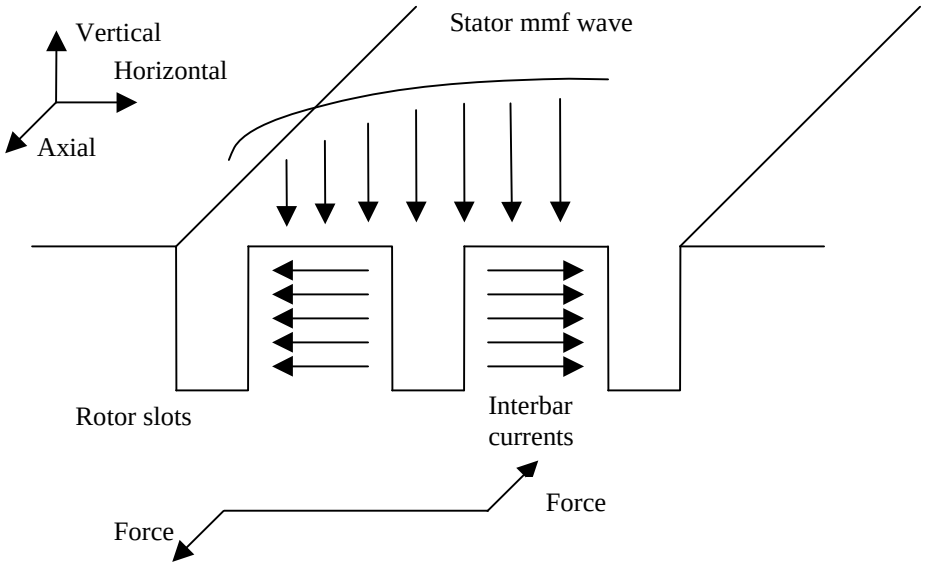


Figure 3.2: Production of axial force model by Muller [30]

Muller [25-26 and 28 - 30] used the following assumptions regarding the model:

- A linear system is assumed, where the principle of superposition applies and effects of saturation may be ignored.
- The interbar currents only flow between the broken bar and the two immediate adjacent bars. (The same assumption was made by Kerszenbaum).
- The normal bar current for these two adjacent bars is excluded. (These bar currents provide not relevant information about the axial force, and can be superimposed on the model at a later stage).

The axial-force frequencies are determined by realising that both the flux density and the interbar currents consist of time harmonics. Consequently the product of the flux density and the rotor currents yields an array of axial force frequencies.

The axial force frequencies used to diagnose interbar currents are [30]:

$$f_v = [(-q_a + q_b) + (q_a - q_b)s]f \tag{3.4}$$

or

$$[(2 - q_a - q_b) + (q_a + q_b)s]f \tag{3.5}$$

where

q_a, q_b = 1, 5, 7….,

f = supply frequency

s = per unit slip

The derived mathematical analysis of the frequency content of the axial force shows that the spectrum of the axial vibration is an array of frequencies. These frequencies are given in Table 2 below, where x is a multiple of 6.

Group	Frequency Component 1	Frequency Component 2	Frequency Component 3
1	-	2sf	-
2	(6-8s)f	(6-6s)f	(6-4s)f
3	(12-14s)f	(12-12s)f	(12-10s)f
4	(18-20s)f	(18-18s)f	(18-16s)f
5	(24-26s)f	(24-24s)f	(24-22s)f
6	(30-32s)f	(30-30s)f	(30-28s)f
7	(36-38s)f	(36-36s)f	(36-34s)f
8	(42-44s)f	(42-42s)f	(42-40s)f
-	-	-	-
n	(x-(x+2)s)f	(x-xs)f	(x-(x-2)s)f

Table 3.1: Axial vibration frequencies due to broken rotor bars when interbar currents are present by Muller [26].

3.3 Stator Current Monitoring

The stator current monitoring is the most commonly used method for detection of broken rotor bars. McCully and Landy in [22] explained why the stator winding is monitored. The positive-sequence supply voltage applied to the stator winding produces current in the stator winding. This stator phase current produces space harmonic fields in the airgap of an induction machine, which consist of either backward or forward rotating components.

Each of these space harmonic fields induces current components into the copper bars of the squirrel cage rotor. In turn, each of these rotor current components produces field components back into the airgap of the machine. These rotor produced fields induce current components back into the stator winding. Then depending on the condition of the rotor the following will occur:

- If the rotor of the machine is symmetrical (without any rotor fault), the forward rotating components will add and the backward components will sum to zero.

- However, if the rotor of the machine is asymmetrical (with a rotor fault), the backward rotating field components do not sum to zero. These backward rotating components produce sidebands around all the rotor produced current components in the stator winding.

The rotor produced fields' current components that are induced in the stator winding at frequencies given by:

$$f_{sb} = f\left(1 \pm 2s\right) \tag{3.6}$$

Kliman [19], Thomson [39], Elkasabgy [9] and Filipetti [3] used eq. 3.6 to analyse the motor supply current to detect broken bar faults. Their investigations involved investigating sideband components around the fundamental for

detecting broken bars. The lower sideband frequency component f_{lsb} is specifically due to the broken bar and the upper sideband frequency component f_{usb} is due to the consequent speed oscillation.

$$f_{lsb} = f\,(1-2s) \tag{3.7}$$

and

$$f_{usb} = f\,(1+2s) \tag{3.8}$$

Filipetti *et. al.* in [3] showed that broken bars actually give rise to a sequence of such sidebands given by:

$$f_{sb} = f\,(1\pm 2ks) \tag{3.9}$$

where k = 1, 2, 3,….

Kliman *et.al.* [19] expressed the frequencies that are present in the air gap flux due to broken bar faults and that can be observed in the stator current as:

$$f_{sb} = f\left[\left(\frac{k}{p}\right)(1-s)\pm s\right] \tag{3.10}$$

where

$\frac{k}{p}$ = 1, 3, 5…,

These are the high frequencies, which should be observed as the fundamental frequency may be influenced by other factors for early detection of broken rotor bars.

Benbouzid [4] upon reviewing the motor current signature analysis for fault detection suggested that the amplitude of the left sideband frequency component is proportional to the number of broken rotor bars. Then approximated the amplitude I_{brb} of frequency component $f_{lsb} = f(1-2s)$ by:

$$\frac{I_{brb}}{I_s} \cong \frac{\sin\alpha}{2p(2\pi-\alpha)} \tag{3.11}$$

where I_s = stator current fundamental frequency component

$$\alpha = \frac{2\pi R_b p}{R} \tag{3.12}$$

R = number of healthy rotor bars

R_b = number of broken rotor bars

Thomson *et.al.* [38] when developing the tool for detection of broken rotor bars used the equation of the estimation of the number of broken rotors (broken bar factor) as follows:

$$n = \frac{2R}{10^{\frac{N}{20}} + p} \tag{3.13}$$

where

n = estimate of the number of broken rotor bars

R = number of rotor slots

N = average dB difference between the upper and lower sidebands and the supply component

p = number of pole pairs

Walliser [40] then later Muller [26], with Landy highlighted that the fault frequencies in the stator current spectrum can also be calculated by:

$$f_s = n_r q_1 \pm sf \tag{3.14}$$

where

n_r = rotational speed of the rotor in rev./sec.

q_1 = harmonic in mechanical measure

The stator slot harmonics are calculated according to

$$q_1 = S_1 \pm p \tag{3.16}$$

where

S_1 = number of stator slots

p = number of pole pairs

3.4 Flux Monitoring

Kliman *et.al.* [19], and Tavner and Penman [37] state that axial leakage flux occurs in all electrical machines due to the fact that no machine can be constructed perfectly symmetrical. Kliman *et.al.* [19] by mounting an external axial flux coil around the shaft of the motor, determined that the axial gap flux frequencies that are present due to machine asymmetrices can be expressed by eq. 6 with k = harmonic index = 1, 2, 3, …. There were two important features noted by Kliman *et. al*:

- The magnitude of the line frequency sidebands due to asymmetries may be comparable to or larger than those due to a broken rotor bar in the same motor, and
- The magnitudes of the asymmetry components decay much more rapidly, in the higher harmonics, than those for a broken rotor bar.

Two conclusions were drawn from the above features; the first conclusion to be drawn is that there is real possibility that, with sensitivity sufficient to detect a single broken rotor bar, manufacturing or other asymmetries may give rise to a false broken bar indication. The second conclusion that may be drawn is that by examination of the higher harmonic amplitudes asymmetries may be distinguished from broken bars, hence the development of eq. 10 to monitor these higher harmonic asymmetries.

Milimonfared *et. al.* [13] stated that the reaction by $(1 \pm 2s)f$ sideband harmonics of the stator current with the rotor produces currents with the frequency of $3sf$.

As a result of rotor asymmetry, the stator currents contain harmonic components of by $(1 \pm ks)f$ and the rotor currents contain harmonic components of $\pm ksf\,(k = 1,3,5..)$. These harmonic components are the sources of MMF harmonics and, consequently the flux harmonics in the motor structure. Under the rotor asymmetry, these MMF harmonics produce shaft fluxes with the harmonic components of $\pm ksf\,(k = 1,3,5..)$.

The results in [13], after testing by inserting four search coils in a three phase six-pole induction motor, showed the existence of sf, $3sf$, $5sf$ and $7sf$ voltage harmonics in the search coil surrounding the shaft at the faulty end due to the rotor asymmetry.

Even though the commonly used method of broken rotor bar detection is stator current monitoring, the stator current broken rotor bar fault frequencies can be applied to flux monitoring. Walliser [40] holds the same opinion since in the stator current monitoring; the stator winding acts as a coil whereas with flux monitoring an external mounted coil can be used. Walliser suggests that the points applicable to current monitoring technique can be applied to flux monitoring technique.

3.5 The Effects of Load

Kilbey [17] assessed the effect of the load on detection of broken rotor bars and concluded the following:

- The degree to which the motor is loaded affects the temperature of the motor which in turn affects thermal expansion of cracks and breaks. Reduced load may not produce enough heat to open cracked bars.

- Load also affects the speed of the motor. As the motor becomes more heavily loaded, the rotational frequency slows and the slip frequency increases. The

greater the slip, the greater is the frequency separation that can be observed between sideband and line frequency. The lighter the load, the larger the ratio between line frequency amplitude and that of the sideband; especially, as load moves below 50 percent of full load. From 50 to 100 percent load this effect is less significant.

Schoen and Habetler [33] investigated the effects of time-varying loads on rotor fault detection and observed that if the load torque varies with the rotor position, the current spectral harmonics, produced by the load, contain the spectral components, which coincide with those caused by a fault condition. Schoen and Habetler then recommended monitoring of multiple frequency signatures and identifying those components not obscured by the load effect. Benhouzid and Kliman [5] expanded on this, suggesting that broken rotor bars detection is still possible since the current typically contains higher order harmonics than those induced by the load.

CHAPTER 4

MAXWELL 2D SIMULATION OF A CRACKED AND BROKEN ROTOR BAR

The simulation involved analysis of a cracked and single broken rotor of the squirrel cage induction motor using Maxwell 2D Field Simulator. Maxwell 2D Field Simulator is an interactive software package that uses finite element analysis to solve two-dimensional (2D) electromagnetic problems. In performing the simulation to analyse a problem, an appropriate geometry, material properties and excitation for a device or system of devices need to be specified.

4.1 Induction Motor Simulation Parameters

This section presents quantities and parameters used in creating and solving the induction motor for this research. A general procedure for creating and solving a Maxwell 2D model is presented in Appendix A. The simulation was done using guidelines in [2], especially on material, boundary and sources setup and the setup solution.

The induction motor simulated for this research has similar characteristics as the motors used in the industrial motor testing in Chapter 5. The physical motor dimensions measured and used in the simulation are tabulated in Table 4.1.

Stator Dimensional Details	
Description	**Dimension**
Stator Lamination OD to inner casing	18 mm
Stator Lamination ID	888 mm
Stator Winding Depth (1 coil)	45 mm
Stator Winding Thickness	20 mm
Stator Winding Slot	100 mm
Coil Span	6 slots (1-7)
Stator Core Length	980 mm
Stator Winding + Overhang Length	1400 mm
Stator Wedge Depth	5 mm
Stator Wedge Thickness	15 mm
Rotor Dimensional Details	
Rotor Lamination OD	884 mm
Rotor Length	890 mm
Rotor Slot Type	T-bar
Rotor Lip Depth	13 mm
Rotor Lip Width	7.5 mm
Rotor Lip Depth	25 mm
Rotor Lip Width	13 mm
Rotor Bridge Depth	4 mm
Endring Width	50 mm
Endring Thickness	18 mm
Endring ID	764 mm
Calculated Endring Circumference	2400 mm
Support Limp Thickness x 6	52 mm
Support Limp Depth x 6	200 mm
Rotor Shaft OD	176 mm

Table 4.1: Arnot Power Station ID Fan Induction Motor Dimensions

4.1.1 Creating the Model

The solver used for the simulation is the Transient with the model drawn on the XY plane using the dimension in table 2.1. The 2D Modeler was used to create a two dimensional geometric model shown in Fig. 2.3.

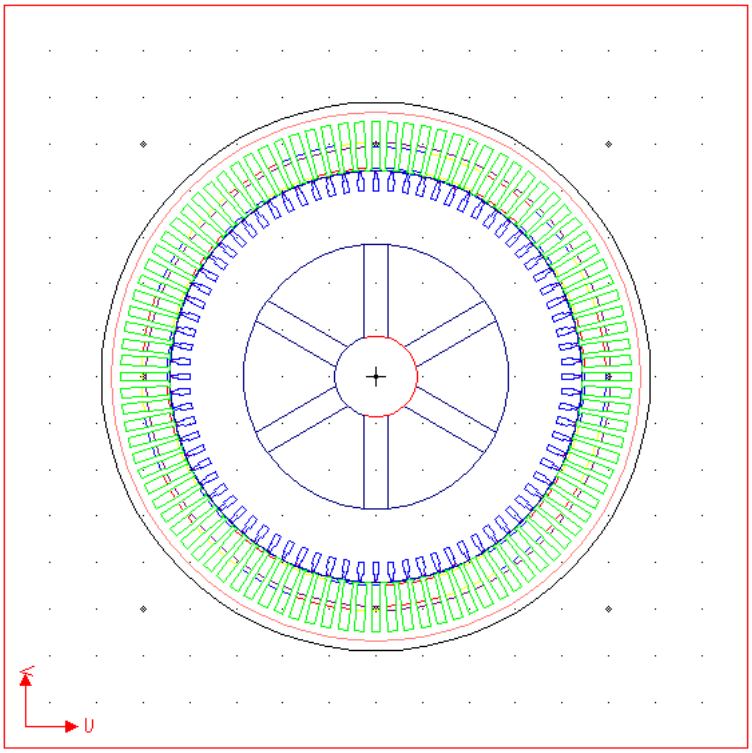


Figure 4.1: The geometric model of the simulated induction motor

The only assumption made in the model is that the casing of the motor is where cooling pipes are in the industrial motors used in the experiment. This was done in order to optimise the model as this has no major impact on the simulation.

The step by step drawing of the model was done using Maxwell 2D User Manual and Training Models. In drawing the model, stator and rotor slots as well stator coils and rotor bars were drawn as single objects then duplicated around origin (0, 0). This process was also performed for drawing of the rotor support limp objects. Otherwise, the other motor simulation objects, like motor casing and airgap band, were drawn using 2D Modeler/Object/Circle.

After finalising the model, the created objects were grouped using Define Model/Group Objects with respect to their functions and stator-winding layout. The 80 rotor bars were grouped as Rotor_Bars, support limps as Rotor_Spider, winding insulation as Winding_Insulation, stator slots as Stator_Core, rotor slots as Rotor_Core and finally the stator coils (windings) were grouped in phases and with respect to flow current direction e.g. PhaseAn (phase A negative) and PhaseAp (phase A positive).

4.1.2 Materials Setup

The next step, in simulating the motor in Maxwell 2D after grouping the objects, is assigning the materials. The materials were assigned as follows:

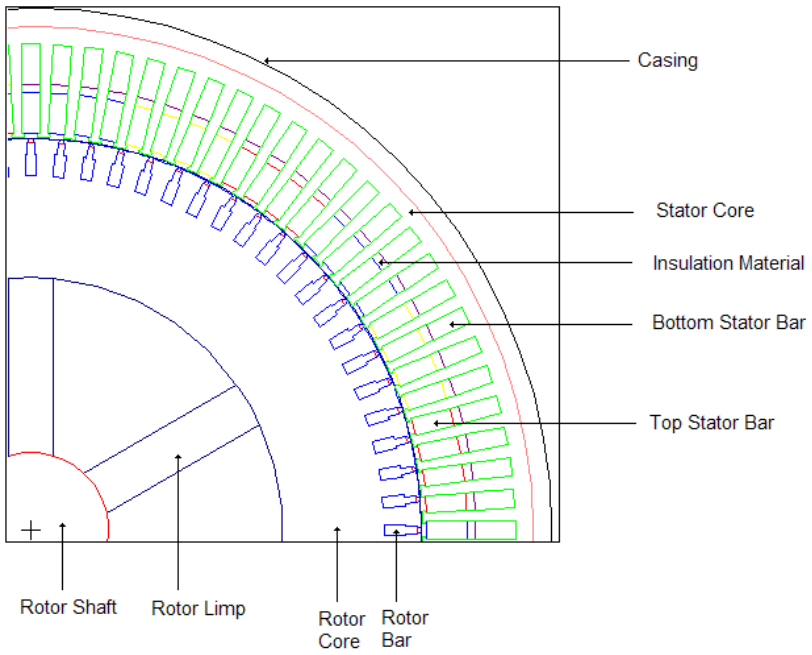


Figure 4.2: Maxwell 2D model materials description

Object	Material
[AirGap_Band]	vacuum
[Motor_Casing]	air
[PhaseAn]	copper
[PhaseAp]	copper
[PhaseBn	copper
[PhaseBp]	copper
[PhaseCn]	copper
[PhaseCp]	copper
[Rotor_Bars]	copper
[Rotor_Core]	non-conductive
[Rotor_Spiders]	non-conductive
Shaft	steel_1010
[Stator_Core]	non-conductive
[Winding_Insulation]	mica

Table 4.2 Material Set-up of the Simulated Motor

The stator and rotor cores were setup as non-conductive materials with a conductivity of zero so as for current to flow only in the stator windings and rotor bars.

4.1.3 Boundary and Sources Setup

This step in the simulation process is used to setup the sources and to assign the endring parameters. It must be noted that in electric motors, windings are generally voltage supplied with the resulting currents dependent on the resistance of the winding and the back electromotive force (EMF). The motor casing was setup as the boundary and the following materials setup as follows:

- The endring was setup as a passive end-connected conductor with 0.008 ohms in the end resistance between adjacent conductors and 0.005 henries in the end inductance between adjacent conductors.
- The phases were assigned the voltage sources as stranded with the following functions:
  - PhaseA=3300*sqrt(2/3)*cos(2*pi*50*T)
  - PhaseB=3300*sqrt(2/3)*cos(360*50*T - 120)
  - PhaseC=3300*sqrt(2/3)*cos(360*50*T - 240)

  The windings in each phase were assigned as positive and negative polarity according to grouping in section 2.2.1. Furthermore, the terminal attributes were assigned; the resistance value of 8 ohms, inductance of 0.003 henries, 200 total turns as seen from the terminal and 4 number of parallel branches.

4.1.4 Setup Solution

The important part of the Maxwell simulation is meshing. The quality of the mesh is critical to the accuracy and the convergence of the field solution. The mesh must be fine in regions where a large magnetic field gradient occurs (such as air gaps and rotor bars) and large elsewhere.

The process executed, for this simulation, was by choosing Manual Mesh and then accepting the number of levels for the QuadTree Seed. From this, a basic coarse mesh was generated and had to be refined for an accurate solution. The refining occurred by selecting objects, which are critical for solution accuracy. The number of elements in the AirGap_Band, Rotor_Bars and Stator_ Coils were made greatest to obtain a more accurate solution.

As a result of the refining for the accurate solution, the mesh was created as shown in Fig. 4.3 below.

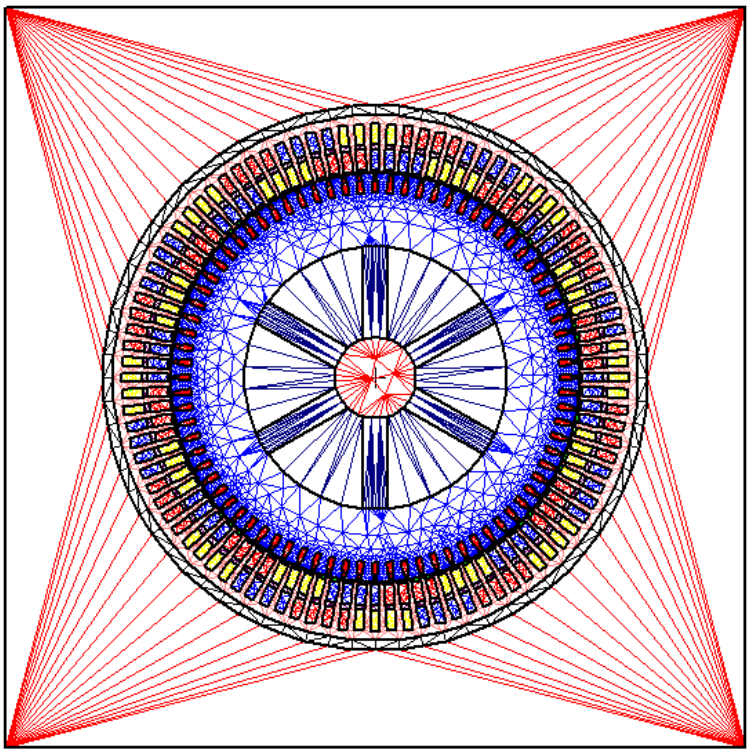


Figure 4.3: Maxwell 2D simulation mesh

4.1.5 Solution Options

The ‘Time Step’ which instructs the solver to calculate the fields at each stipulated time of the solution process, was chosen in a manner to be able to study even high frequency harmonics as will be seen in the simulation results. The model depth was chosen to be 980 mm which is the length of the stator winding.

4.1.6 Motion Setup

For the motion setup a band was defined in the airgap. The band can be defined as a moving object that contains all moving objects. Then rotation was selected as the type of motion to be used with the set position at (0, 0) as the centre of

rotation. The mechanical setup of the motor was set at 747 rpm for the same load of the motor being that was used in the experiment.

4.1.7 Signal Processing

The simulation stator current signals were then exported and processed using Matlab to perform an FFT. The FFT function used and processing is explained in more detail in Chapter 5 section 5.3.2.

4.2 Induction Motor Simulation Results

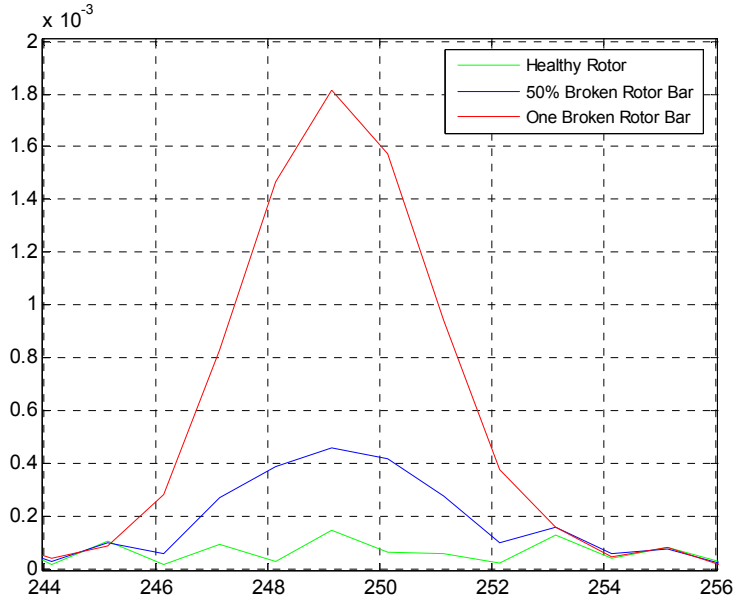


Figure 4.4: Simulated stator current at the 5th harmonic

Fig. 4.4 shows a high increase in the amplitude of the simulated stator current at the 5th harmonics after a rotor bar break where $(5-6s)f$ component is. Whereas, Fig. 4.5, below, shows a slight increase after a rotor bar crack (50% broken rotor bar).

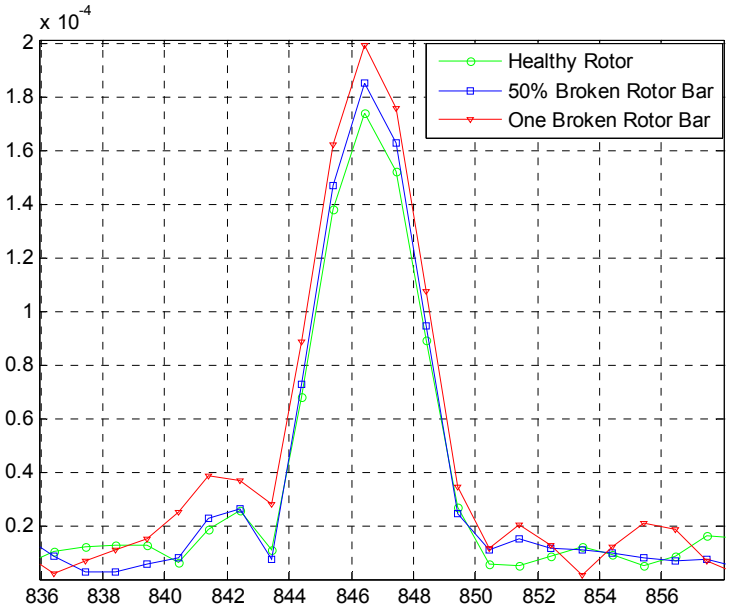


Figure 4.5: Simulated stator current at the 17th harmonic

Component	Harmonic	Theoretical Fault Frequency (Hz)	Simulated Fault Frequency (Hz)
$(1-2s)f$	1	49.6	49.4
$(3-4s)f$	3	149.2	149.1
$(5-6s)f$	5	248.8	249.1
$(7-8s)f$	7	348.4	349.2
$(9-10s)f$	9	448.0	448.2
$(11-12s)f$	11	547.6	548.3
$(17-18s)f$	17	846.4	846.4
$(19-20s)f$	19	946.0	946.5
$(21-22s)f$	21	1045.6	1046.5
$(27-28s)f$	27	1344.4	1345.5
$(43-44s)f$	43	2141.2	2141.5
$(53-54s)f$	53	2639.2	2638.8
$(61-62s)f$	61	3037.6	3038.8

Table 4.3: Comparison of theoretical and simulated stator currents for s = 0.004

The theoretical and simulated stator current frequencies for detection of rotor bar faults for the simulated motor at s = 0.004 are very similar to each other especially in lower harmonics. This indicates that the simulation results give a good indication of rotor bar detection frequencies for the conditions, the motor was simulated under. These frequencies are later utilised for the detection of a cracked and broken rotor bar in the experiment of the research.

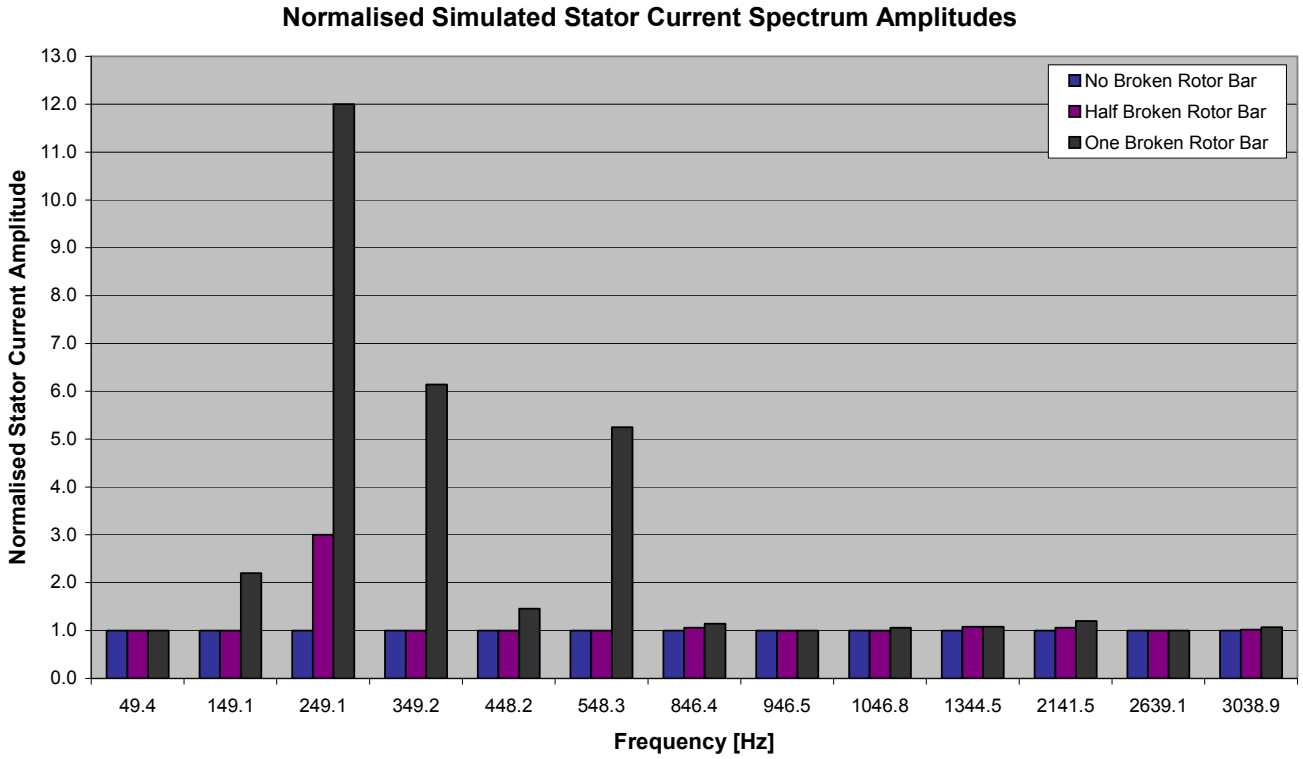


Figure 4.6: Normalised simulated stator current results

The simulation was done in order to study broken rotor bar detection frequencies and observe how much the current amplitudes vary from no broken rotor bar, cracked rotor bar (half broken bar) to completely broken bar. Figure 4.6 indicates the variation of the stator current amplitudes on different harmonics. The $(5-6s)f$ component (5^{th} harmonic) shows a 3 times increases from no broken bar to a half broken rotor bar then a 12 times increase for a completely broken rotor bar. The $(7-8s)f$ and the $(11-12s)f$ components show a 6.1 and 5.3 times

increase after a completely broken rotor bar respectively with no increase after a rotor bar crack. In other harmonics, there are slight increase as can been seen in Figure 4.6.

4.3 Induction Motor Simulation Conclusion

The results of the Maxwell 2D simulation affirm the theoretical rotor bar detection frequencies, which are expressed by eq. 3.10. Most theoretical and simulated rotor bar detection frequencies are within or less than 0.5 Hz of each other. Furthermore, the results show how the stator current amplitudes vary at specific frequencies from no broken bar to a cracked bar and then to a completely broken bar. When a bar is completely broken there is a significant increase in the stator current amplitude. This simulation study gave a base for the broken rotor detection frequencies to be examined when performing the experimental measurements on industrial squirrel cage induction motors.

CHAPTER 5

EXPERIMENTAL TESTING DETAILS AND DATA PROCESSING

5.1 Experimental Test Details

Recently, a high frequency of electric motor failures due to broken rotor bars have been experienced at Eskom generation power stations. This prompted an investigation to determine an optimal technique to detect breaking of bars at the inception of the break.

The research involved uses a wide range of conventional broken rotor bar detection techniques and also explores new detection techniques. The testing was performed using different measuring instruments, operated by a number of test personnel from different companies and most importantly analysis of results.

The experimental testing involved testing of two industrial induction motors which had operated as induced draught fan motors at Arnot Power Station. The testing was performed at a motor repair workshop, which had a capability to load a motor to simulate operating plant condition. The two induction motors were of the same design, even though other the motor had indications that it might have been rewound before.

The conventional rotor bar detection techniques performed were vibration (radial and axial) monitoring and stator current monitoring. The non-conventional techniques explored were shaft voltage and leakage flux monitoring (leakage flux results included in Appendix F). The tests measurements were taken under different condition of the rotor bar that is without any broken rotor bar, half broken rotor bar and fully broken rotor bar at different loads. The first phase of testing, involved testing the motors as received with an assumption that there were no broken rotor bars. The second phase of testing, involved testing after inducing a

rotor bar fault into the two induction motors with the testing personnel not knowing which one had what fault induced on it.

The motor details are provided below in Table 5.1.

General Motor Details	
Description	**Rating**
Serial No.:	300068/01 & 300071/01
Supply Connection	3 phases
Rated Voltage	3.3 kV
Rated Current	352 A
Power Rating	2300 hp = 1.7 MW
Rated Speed	744 rpm
Number of Poles	8 poles
Number of Stator Slots	96
Number of Rotor Slots	80

Table 5.1: Arnot Power Station ID Fan Induction Motor Specifications used for experimental measurements

The other motor details, which include dimensional details of the motors, were earlier included in Chapter 4.

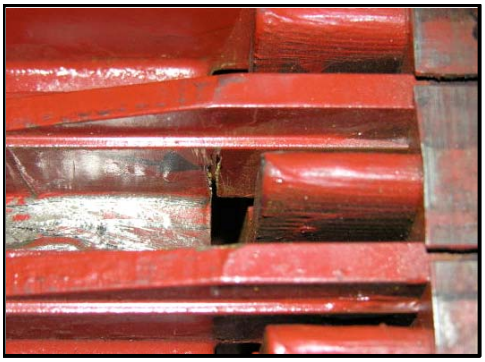


Figure 5.1 (a) Half broken rotor bar

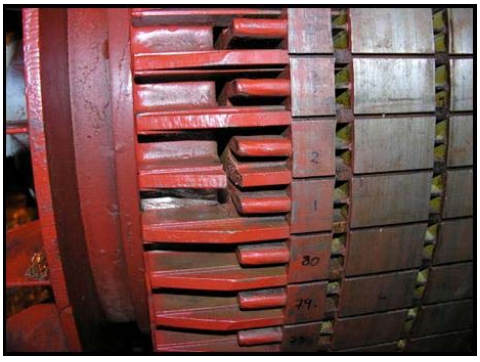


Figure 5.1 (b): One fully broken rotor bar

Fig. 5.1 (a) and (b) illustrate a half-broken and one fully broken rotor bar used in the experimental testing. This specific rotor was used in the initial experimental measurements performed in 2005 indicated in Chapter 5 in [47] when the project initial commenced but is of the similar design as the motors used in the experiment for this research.

5.2 EXPERIMENT MEASURING INSTRUMENTS

5.2.1 Current Transducer

A current transducer was used to capture the current induced into the stator winding by rotor bars. The current transducer used was a LEM-flex RR3030 AC current probe which is a Rogowski coil and works on the Rogowski principle. The Rogowski coil consists of a helical coil of wire with the lead from one end returning through the centre of the coil to the other end, so that both terminals are at the same end of the coil. The whole assembly is then wrapped around the straight conductor whose current is to be measured. Since the voltage that is induced in the coil is proportional to the rate of change (derivative) of current in the straight conductor, the output of the Rogowski coil is then connected to an electrical (or electronic) integrator circuit in order to provide an output signal that is proportional to current.



Figure 5.2: LEM-flex RR3030 AC current probe

LEM-flex RR3030 Specifications	
Current Measuring Range	30 – 3000 A
Output	100 – 1 mV/A
Frequency Range	10 Hz – 50 kHz
Accuracy	1 % of range
Operating Temperature	-20°C to 85°C
Noise	4 mV
Phase Error (<1°)	45 – 65 Hz
(<10°)	At 20 kHz

Table 5.2: LEM-flex RR3030 Specifications

The Rogowski coils were wrapped around the motor supply cables in each phase. Then the current signals from each phase were captured through coaxial cables using a dSpace adaptor box and fed into a dSpace data acquisition card DS1104.

5.2.2 Vibration Sensors

As it is not easy to measure the vibration on the rotor, the most appropriate solution is to measure on the frame of the motor, since the force on the rotor is transferred through the bearing to the motor frame. Also Muller [28] stated the principal frequencies of axial force act on the rotor and are transferred directly as an axial vibration to the frame via bearings. It is important to realise that these frequencies in the axial vibration spectrum are also modulated by the inherent vibration of the rotor at rotational speed. The origin of the rotational force is due to mechanical unbalance.

The vibration sensors utilised in the experiment were accelerometers of an analog style accelerometers which outputted a continuous voltage that is proportional to acceleration 100mV/g. The accelerometers were magnetically to the body of the motor at the DE of the motor. Radial and axial vibration measurements were taken for the experiment.

The vibration signals were then passed through a charge amplifier by coaxial cables then to the dSpace card DS1104 as indicated in Figure 5.6 below.



Figure 5.3: Connection of accelerometers for vibration measurements

5.2.2 Speed Sensor: Tachometer

The motor speed was measured using a digital tachometer, model RM-1501.



Figure 5.4: Digital Tachometer RM-1501 for speed measurement

The tachometer was then connected by a coaxial cable to the dSpace card DS1104 as indicated in Figure 5.6 below.

Digital Tachometer RM-1501 Specifications			
	Range	Resolution	Accuracy
RPM (optical)	10.00 to 99999 rpm	0.01/0.1/1	0.04% ± 2dgtst
RPM (contact)	20.00 to 29999 rpm	0.01/0.1/1	0.04% ± 2dgtst
Sampling Rate		0,7 sec (>60 rpm) & 1 sec (10 to 60 rpm)	
Measuring Distance		50 to 300mm	
Operating Temperature		0ºC ~ 50ºC	
Range Selection		Automatic	
Accessories		Software and RS-232 interface	

Table 5.3: Digital Tachometer RM-1501 Specifications

5.3 DATA ACQUISITION AND PROCESSING

5.3.1 dSpace: DS1104 R&D Controller Board

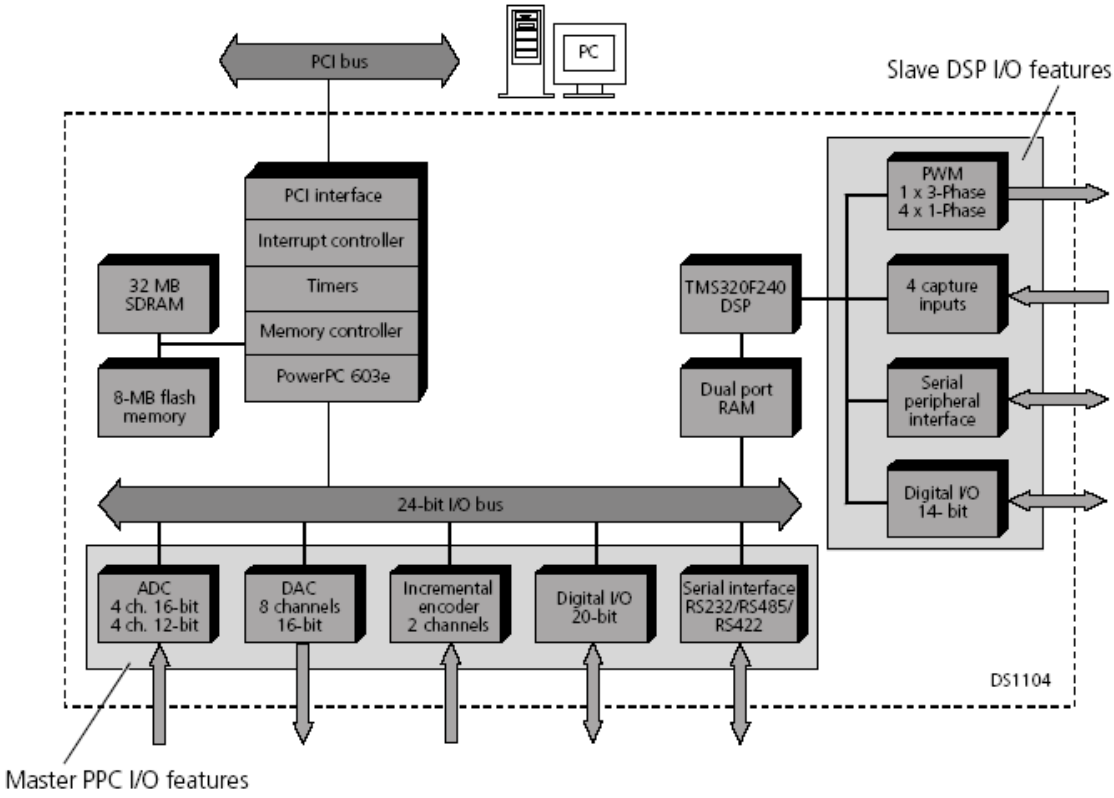


Figure 5.5: An overview of the architecture and functional units of the DS1104

The DS1104 R&D Controller Board provides the following features:

- **Master PPC** representing the computing power of the board, and featuring several I/O units
- **Slave DSP** featuring further I/O units
- **Interrupt controller** providing various hardware and software interrupts
- **Memory** comprising DRAM and flash memory,
- **Timers** providing a sample rate timer, a time base counter, and 4 general-purpose timers,
- **Host interface** for setting up the DS1104, downloading programs and transferring runtime data from/ to the host PC.

Further specifications of the DS1104 are included in Appendix B. The dSpace Control Desk for data acquisition was setup as seen below in Fig. 5.6.

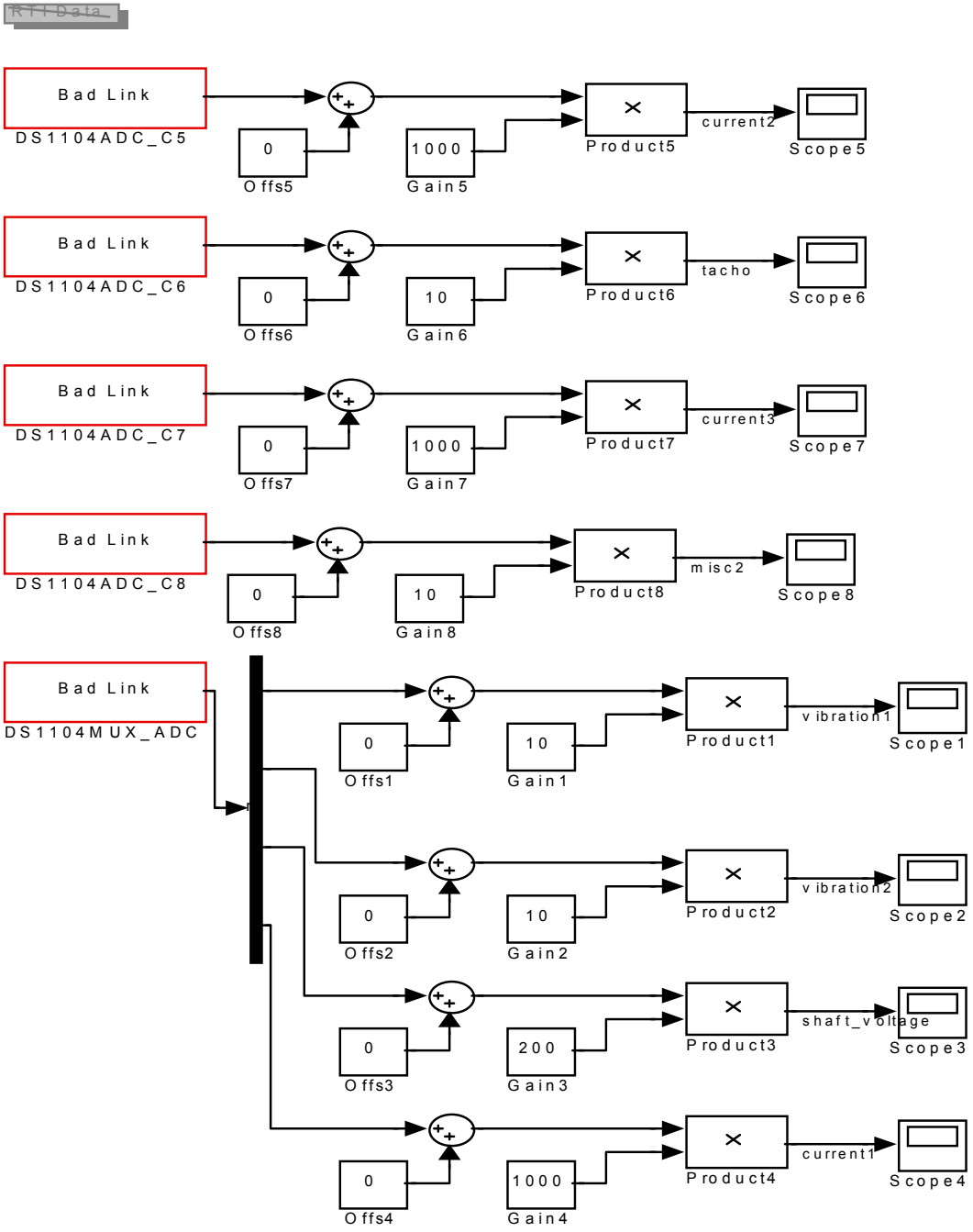


Figure 5.6: dSpace Control Desk setup for experimental work

5.3.2 Signal Processing

The second most important aspect of signal analysis (and of this research) is the signal processing before fault diagnosis. Ayhan *et. al.* [43] mentioned that the Fast Fourier Transform (FFT) is the most widely used non-parametric spectrum analysis method, which yields efficient and reasonable results for MCSA technique. The FFT is an algorithm to compute the Discrete Fourier Transform (DFT) of a discrete time series function with minimum computational effort. FFT algorithms compute the DFT of the given time series by successively decomposing the *N*-point DFT computation into computations of smaller size.

Ayhan [43] suggests that Welsch's periodogram method is most efficient than FFT and periodogram methods in terms of fault detection performance. Although all the three methods are based on DFT technique, the use of a Hanning window and overlapping segments in Welch's method contributed to the fault detection in a positive way. The use of Hanning window reduces the side effect of the sidelobes and results in a decrease in the PSD estimate bias. The side lobes of the signal spectrum cause the signal power leak into other frequencies. The bias of the PSD estimate is due to this spectral leakage. Applying a tapered window to the signal in the spectral estimation, such a Hanning window reduces the effect considerably. This results in a decreased estimation bias, which shows that the PSD estimate is closer to the real value. On the other hand, overlapping segments case the data treatment and smoothing of the PSD estimate. As the number of data segments increase, the PSD estimate variance decreases. Both these positive effects suggest that Welch's periodgram method is a preferred approach when compared to the other two inspected methods in the broken rotor bar fault detection of induction motors.

However, Dhuness [47] suggested that the Welsh's method is not adequate for large machines as the magnitude of interbar currents may become larger than fault frequency components as stipulated by Landy. Landy *et.al.* [20] outlined the

signal processing to be employed in large machines as outlined in Fig. 5.7. The MATLAB™ codes used for the signal processing are included in Appendix B.

- Filtering: the function of the filter is to remove unwanted parts of the signal, such as random noise, or to extract useful parts of the signal, such as components lying within a certain frequency range.

- Windowing as explained by Ayhan [43] above.

- Zero-padding: Zero-padding is adding a series of zeros onto the end of the signal. This is done to overcome the problem of picket fencing which is when the peak of a frequency of interest lies between the two of the discrete transform lines. If the frequency resolution of the spectrum is defined as

$$\Delta f = \frac{f_s}{N} \tag{5.1}$$

  The number of points by M, the frequency resolution becomes

$$\Delta f = \frac{f_s}{N + M} \tag{5.2}$$

  Zero-padding improves the resolution of the spectrum.

- FFT: The FFT is an algorithm to compute the Discrete Fourier Transform (DFT) of a discrete time series function with minimum computational effort. The DFT takes a discrete signal in the time domain and transforms that signal into its discrete frequency domain representation. FFT is then extremely important in frequency (spectrum) analysis.

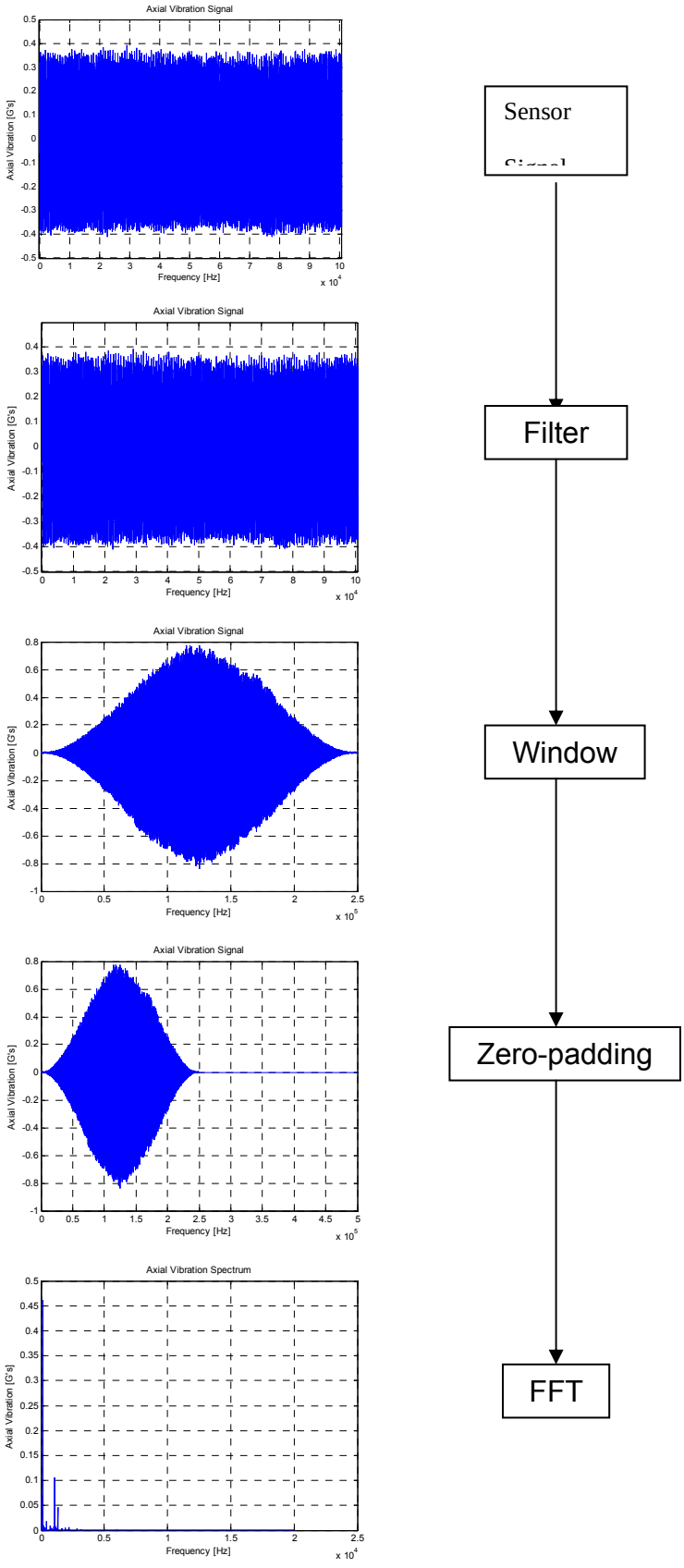


Figure 5.7: Summarised signal processing process [20]

5.3.3 Selection of FFT parameters [20]

This subsection discusses important parameters in signal data processing which are important for capturing the signals.

The most important signal processing equations are:

$$T = \frac{1}{\Delta f} = N.\Delta t = \frac{N}{f_s} \tag{5.1}$$

and

$$\Delta t = \frac{1}{f_s} = \frac{1}{n_y f_{high}} \tag{5.2}$$

where

T = total time for time wave

n_y = Nyquist rate

N = number of sample points

Δt = time between samples in the time waveforms

Δf = frequency resolution in the frequency domain

f_s = sampling frequency

Each acquisition requires that the sampling rate and the resolution be determined. These two parameters determine the total acquisition time and the resolution of the signal in time domain.

5.3.3.1 Sampling rate

The sampling rate is calculated as:

$$f_s = n_y f_{high} \tag{5.3}$$

The highest frequency (f_{high}) that is required for successfully monitoring the motor should be known and used to set the sampling rate. The Nyquist rate (n_y) of depends on the spectrum analyzer and more specifically the roll-off of the anti-aliasing filter.

5.3.3.2 Frequency resolution

The frequency resolution is determined by the number of points and the sampling frequency. Invariably the number of points is limited by the spectrum analyzer. The frequency resolution is

$$\Delta f = \frac{f_s}{N} \tag{5.4}$$

Prior knowledge of the frequency spectrum is necessary in order to select an acceptable frequency resolution. If the frequency resolution is not of acceptable level, the time signal may be zeropadded. Zeropadding the time signal however requires intensive processing, and all the original time points.

5.3.3.3 Acquisition time and time resolution

These parameters are automatically set by determining the sampling rate and the frequency resolution. The total acquisition time is determined by eq. 5.1. and 5.2.

CHAPTER 6

INDUSTRIAL EXPERIMENTAL RESULTS AND DISCUSSION

6.1 Experimental Results Introduction

The experimental results for the tests performed are presented in this order, stator current analysis, axial vibration analysis and shaft voltage analysis for each motor before and after fault inception. Comparisons of the literature supporting each technique as well as the Maxwell simulation results of the stator current are outlined in this section.

6.2 Motor Stator Current Analysis

When using the stator current signature to monitor the condition of the rotor bars, eq. 3.7 and eq. 3.8 were used and compared with the fault frequencies obtained from testing before and after fault inception.

The results presented below, in Table 6.1, indicate expected theoretical fault frequencies for Motor A at 54% load, running at a speed of 747 rpm then the slip is 0.004. The table presents all fault frequencies from the first harmonic till the 61^{st} harmonic.

Harmonic	Lower Component $f_{lsb} = f\left[\left(\frac{k}{p}\right)(1-s)-s\right]$	Frequency (Hz)	Upper Component $f_{usb} = f\left[\left(\frac{k}{p}\right)(1-s)+s\right]$	Frequency (Hz)
1	$(1-2s)f$	49.6	f	50.0
3	$(3-4s)f$	149.2	$(3-2s)f$	149.6
5	$(5-6s)f$	248.8	$(5-4s)f$	249.2
7	$(7-8s)f$	348.4	$(7-6s)f$	348.8
9	$(9-10s)f$	448.0	$(9-8s)f$	448.4
11	$(11-12s)f$	547.6	$(11-10s)f$	548.0
13	$(13-14s)f$	647.2	$(13-12s)f$	647.6
15	$(15-16s)f$	746.8	$(15-14s)f$	747.2
17	$(17-18s)f$	846.4	$(17-16s)f$	846.8
19	$(19-20s)f$	946.0	$(19-18s)f$	946.4
21	$(21-22s)f$	1045.6	$(21-20s)f$	1046.0
23	$(23-24s)f$	1145.2	$(23-22s)f$	1145.6
25	$(25-26s)f$	1244.8	$(25-24s)f$	1245.2
27	$(27-28s)f$	1344.4	$(27-26s)f$	1344.8
29	$(29-30s)f$	1444.0	$(29-28s)f$	1444.4
31	$(31-32s)f$	1543.6	$(31-30s)f$	1544.0
33	$(33-34s)f$	1643.2	$(33-32s)f$	1643.6
35	$(35-36s)f$	1742.8	$(35-34s)f$	1743.2
37	$(37-38s)f$	1842.4	$(37-36s)f$	1842.8
39	$(39-40s)f$	1942.0	$(39-38s)f$	1942.4
41	$(41-42s)f$	2041.6	$(41-40s)f$	2042.0
43	$(43-44s)f$	2141.2	$(43-42s)f$	2141.6
45	$(45-46s)f$	2240.8	$(45-44s)f$	2241.2
47	$(47-48s)f$	2340.4	$(47-46s)f$	2340.8
49	$(49-50s)f$	2440.0	$(49-48s)f$	2440.4
51	$(51-52s)f$	2539.6	$(51-50s)f$	2540.0
53	$(53-54s)f$	2639.2	$(53-52s)f$	2639.6
55	$(55-56s)f$	2738.8	$(55-54s)f$	2739.2
57	$(57-58s)f$	2838.4	$(57-56s)f$	2838.8
59	$(59-60s)f$	2938.0	$(59-58s)f$	2938.4
61	$(61-62s)f$	3037.6	$(61-60s)f$	3038.0

Table 6.1: Theoretical calculation of stator current fault frequencies for s = 0.004

When using eq. 3.14, the rotor bar fault frequencies for Motor A at 54 % load, running at 747 rpm with s = 0.004 and n_r = 12.45.

	Harmonic	Frequency (Hz)	
	q_1	$-sf$	$+sf$
Fundamental	4	49.6	50
Slot harmonic	-92	1145.2	1145.6
Slot harmonic	100	1244.8	1245.2

Table 6.2 Stator current rotor bar fault frequencies as in [40]

The slot harmonics of orders -92 and 100 as determined by eq. 3.14 are indicated in Fig 6.8 and 6.9 below.

6.2.1 Motor A Stator Current Analysis

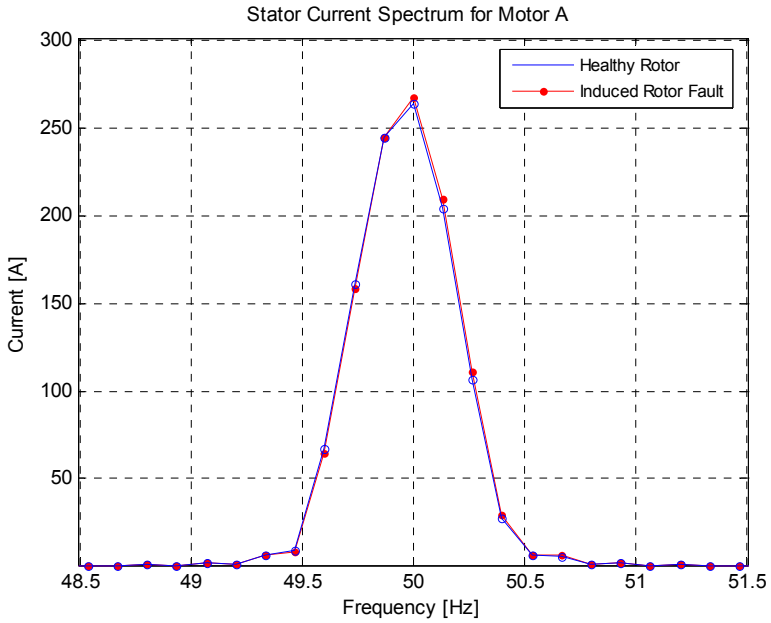


Figure 6.1: Motor A stator current at the1st harmonic (50 Hz)

Figure 6.1 presents the $(1-2s)f$ frequency component of the stator current of Motor A. There are no sidebands in the stator current spectrum after fault inception indicating a cracked or broken rotor bar.

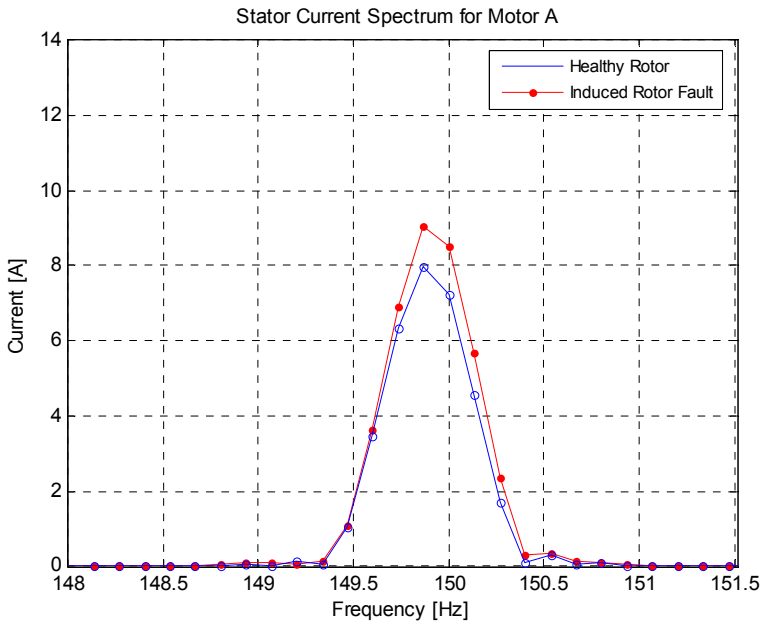


Figure 6.2: Motor A stator current at the 3rd harmonic (150 Hz)

A slight increase in stator current amplitude in the 3rd harmonic can be observed.

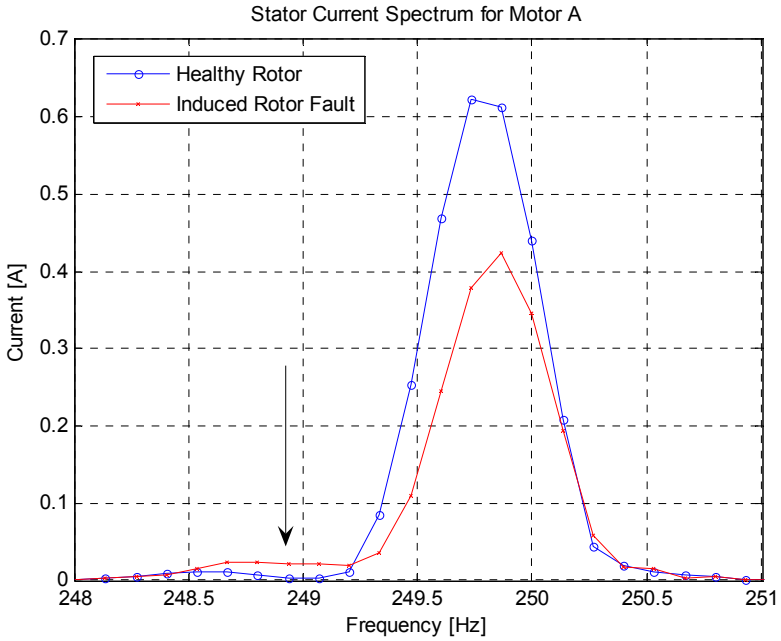


Figure 6.3: Motor A stator current at the 5th harmonic (250 Hz)

A $(5-6s)f$ frequency component (indicated by an arrow in fig. 6.3) shows an increase, which indicates that a rotor bar has defected since the motor A was last

tested. The measured fault frequency at 248.8 Hz has increase by 1.9 times indicating a change in the rotor condition from the last test.

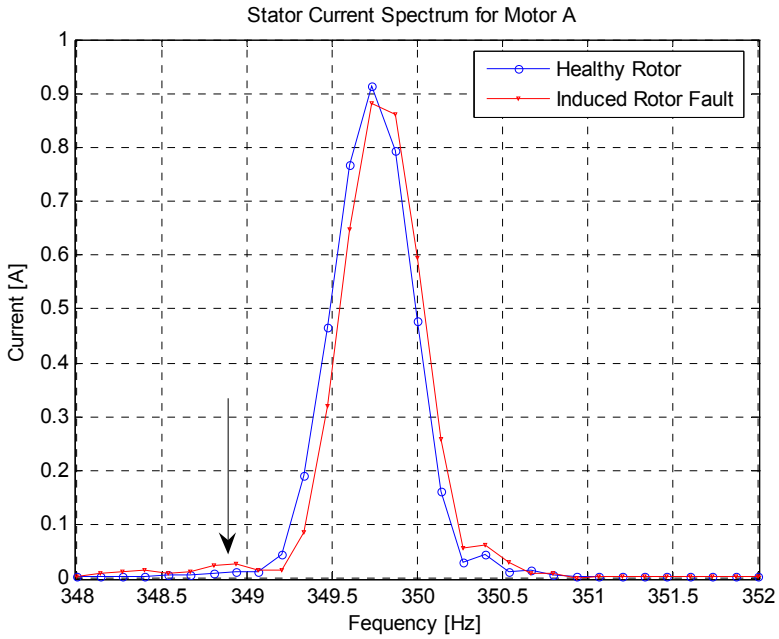


Figure 6.4: Motor A stator current at the 7th harmonic (350 Hz)

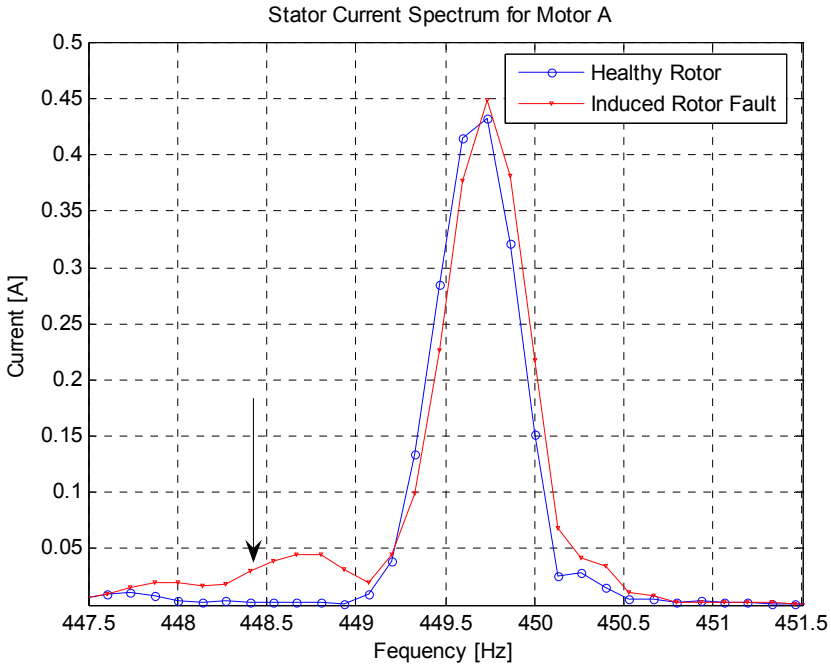


Figure 6.5: Motor A stator current at the 9th harmonic (450 Hz)

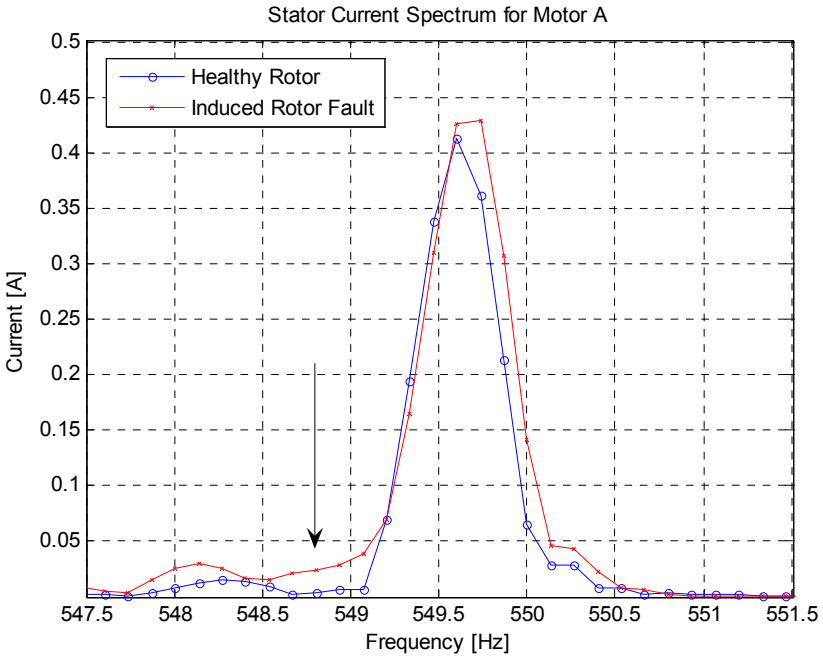


Figure 6.6: Motor A stator current at the 11th harmonic (550 Hz)

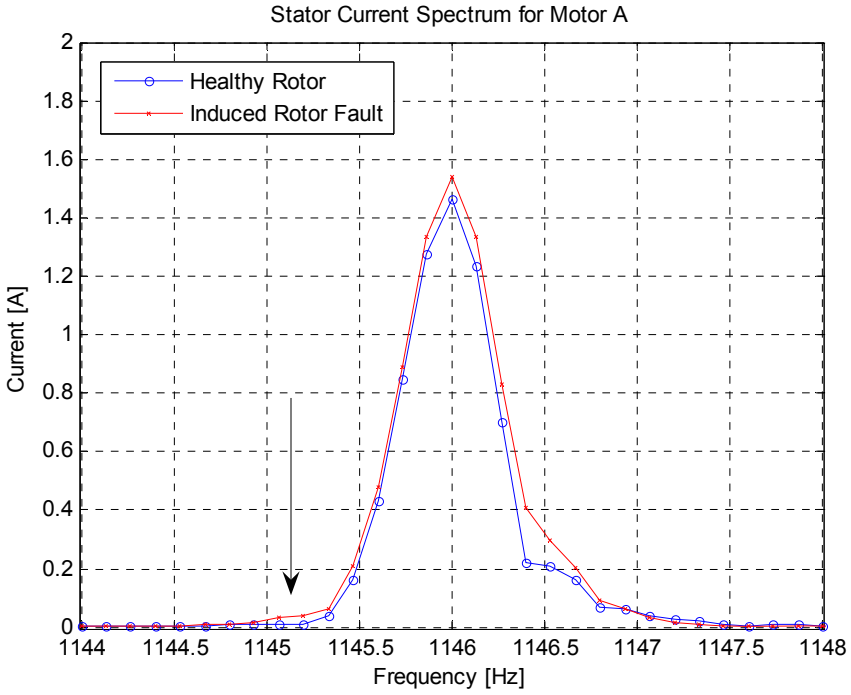


Figure 6.7: Motor A stator current at the 23rd harmonic (1150 Hz)

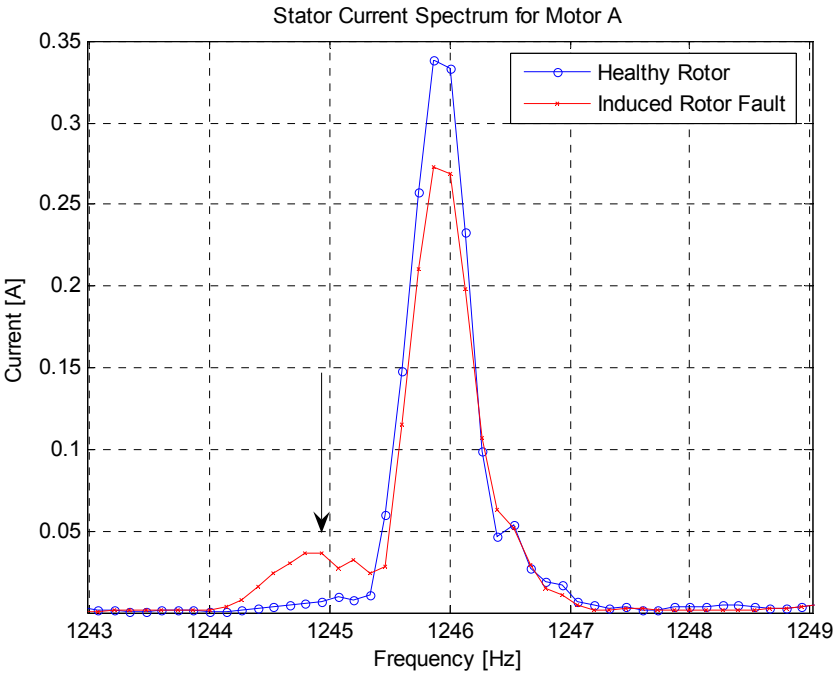


Figure 6.8: Motor A stator current at the 25th harmonic (1250 Hz)

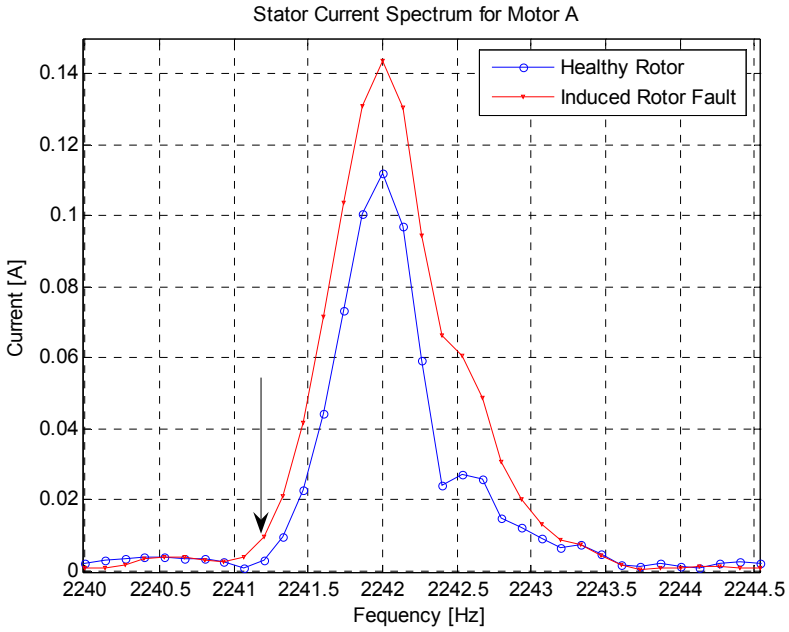


Figure 6.9: Motor A stator current at the 43rd harmonic (2250 Hz)

Figures 6.4 – 6.9 show fault frequencies at various harmonics which indicate and confirm that there is a definitely a rotor bar fault in the Motor A.

The measured fault frequencies are also compared and normalised against a healthy rotor before inducing a rotor fault.

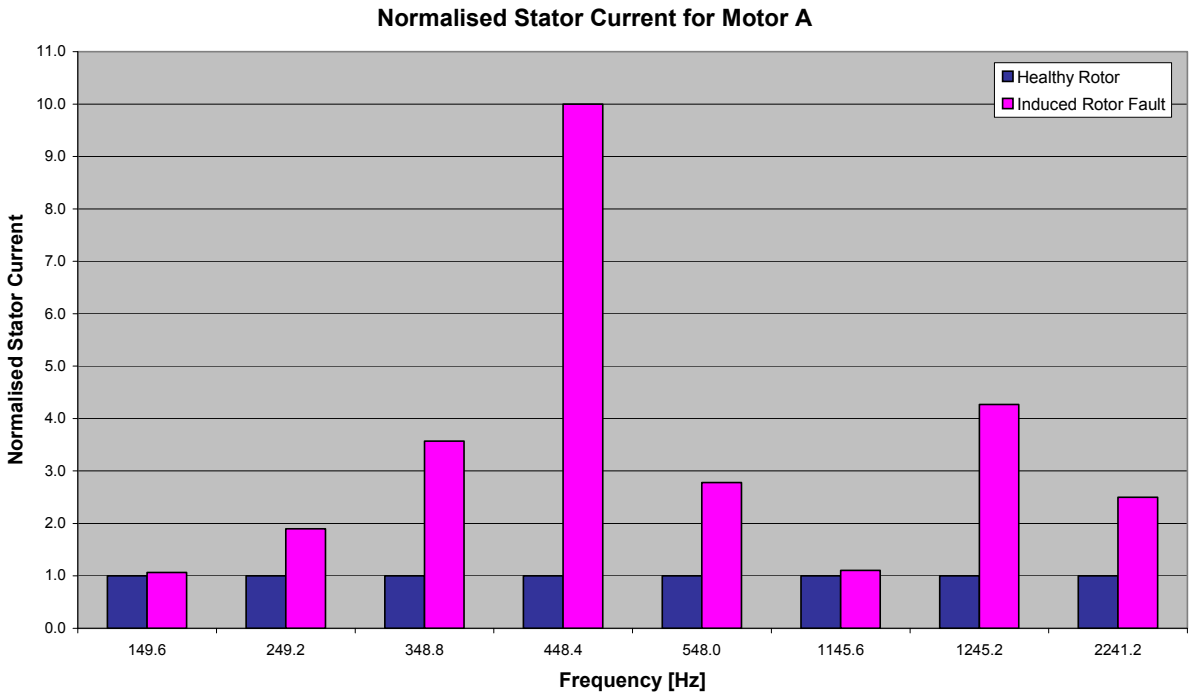


Figure 6.10: Normalised stator current for Motor A at different harmonics

Figure 6.10, which is the normalised stator current for motor A, shows that there is an increase in the fault frequencies amplitudes which suggests that a rotor bar defect has occurred in the motor since it was last tested.

Motor A was also tested at 65% load after inducing a fault in the rotor even though it could not be tested at 65 % load in the first phase of testing. A 65 % load the speed was 746.5 rpm then s = 0.0047 and n_r = 12.43. Using eq. 3.13 and 3.14, the stator current fault frequencies were found and are tabulated below in Table 6.3. The stator current fault frequencies as per Kliman [9] are included in Appendix D.

	Harmonic	Frequency	
	q_1	$-sf$	$+sf$
Fundamental	4	49.47	49.97
Slot harmonic	-92	1143.3	1143.8
Slot harmonic	100	1242.75	1243.25

Table 6.3 Stator current for Motor A at 65 % load

The stator current at 65 % load cannot be compared with the stator current before fault inception because of testing system limitations experienced at high loads in the first phase of testing.

6.2.2 Motor B Stator Current Analysis

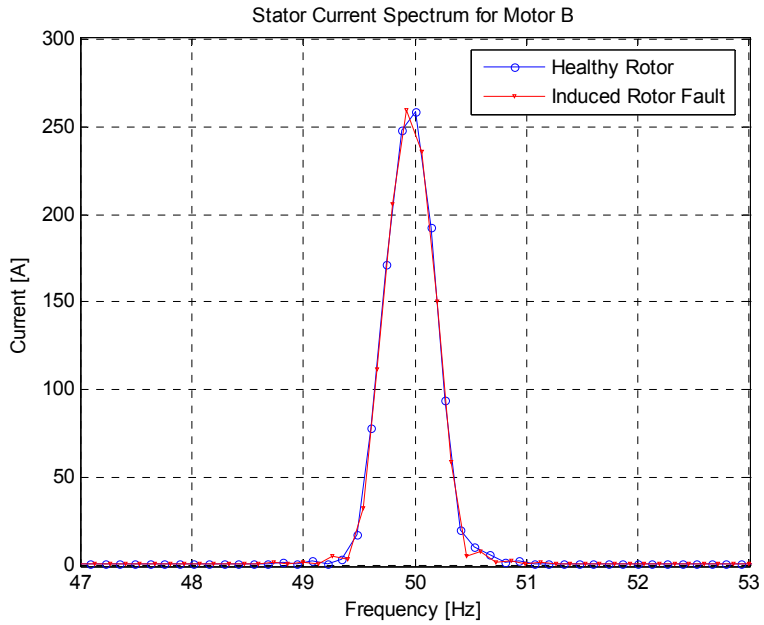


Figure 6.11: Motor B stator current at the 1st harmonic (50 Hz)

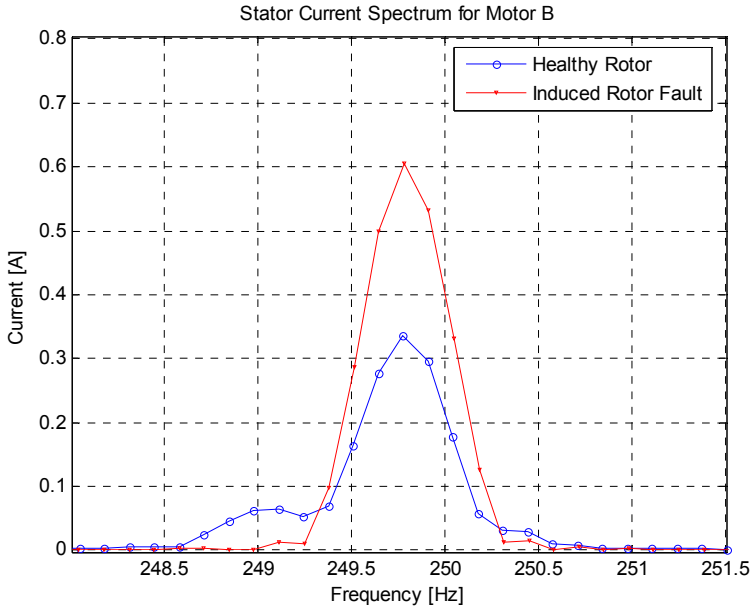


Figure 6.12: Motor B stator current at the 5th harmonic (250 Hz)

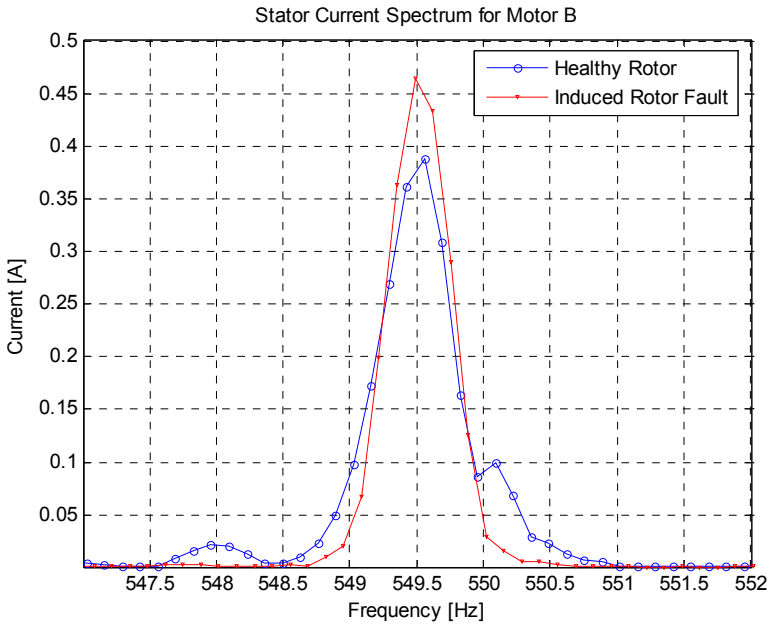


Figure 6.13: Motor B stator current at 11th harmonic (550 Hz)

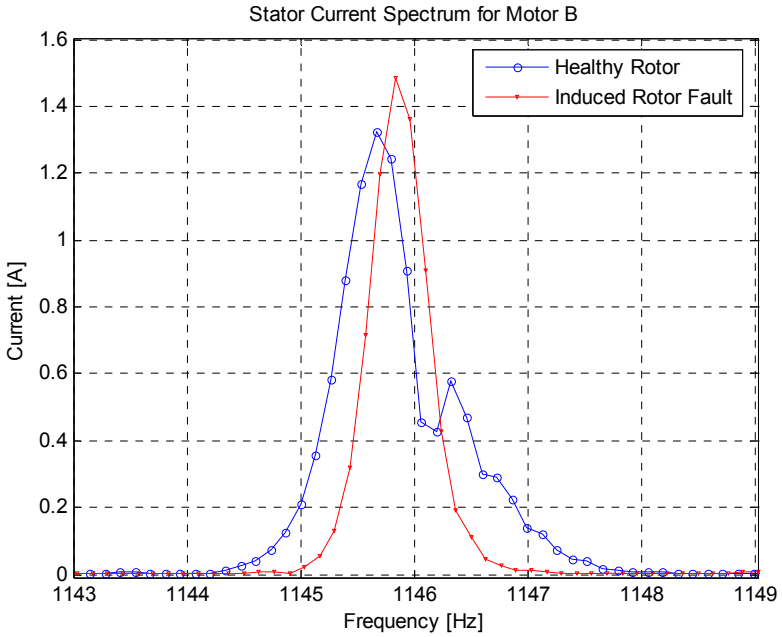


Figure 6.14: Motor B stator current at 23rd harmonic (1150 Hz)

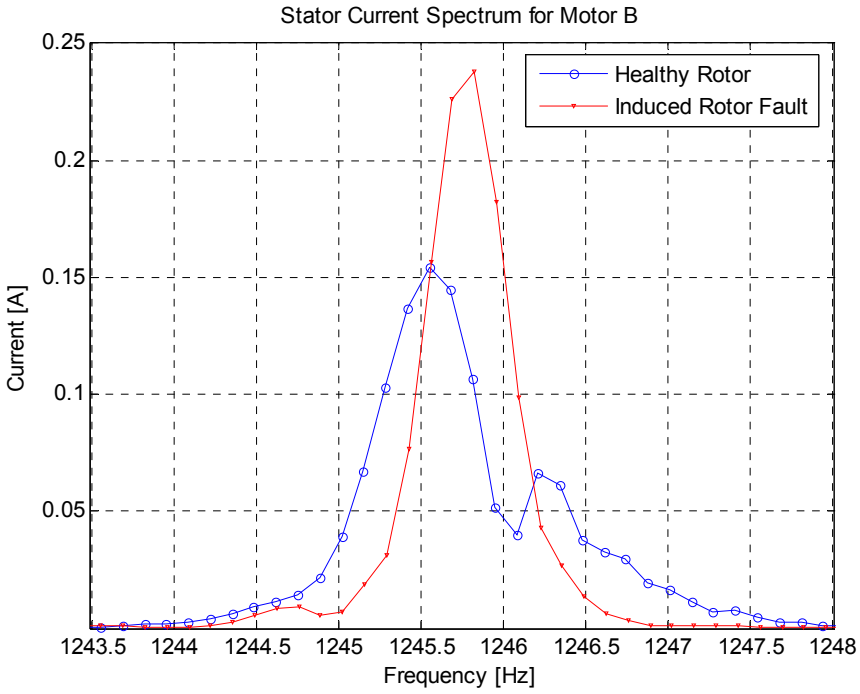


Figure 6.15: Motor B stator current at 25th harmonic (1250 Hz)

Figures 6.11 – 6.15 show the Motor B stator current spectra at different harmonics with an increase in the stator current amplitudes in most of the harmonics. But this could not be directly correlated to the rotor bar fault onto the rotor. It must be noted that there are no fault frequency components observed on the stator current spectra, which indicate a cracked or broken rotor bar.

6.3 Axial Vibration Analysis

The analysis of axial vibration examines theoretical frequencies suggested by Muller (Table 3.1) which are then compared with the measured frequencies at 54% load with the motor running at a speed of 747 rpm. Then from the slip of the motor is 0.004. The axial vibrations for Motor A at 65 % load are included in Appendix B.

6.3.1 Motor A Axial Vibration Analysis

Group	Fault Detection Component 1	Frequency (Hz)	Fault Detection Component 2	Frequency (Hz)	Fault Detection Component 3	Frequency (Hz)
1			sf	0.4		
2	$(6-8s)f$	298.4	$(6-6s)f$	298.8	$(6-4s)f$	299.2
3	$(12-14s)f$	597.2	$(12-12s)f$	597.6	$(12-10s)f$	598.0
4	$(18-20s)f$	896.0	$(18-18s)f$	896.4	$(18-16s)f$	896.8
5	$(24-26s)f$	1194.8	$(24-24s)f$	1195.2	$(24-22s)f$	1195.6
6	$(30-32s)f$	1493.6	$(30-30s)f$	1494.0	$(30-28s)f$	1494.4
7	$(36-38s)f$	1792.4	$(36-36s)f$	1792.8	$(36-34s)f$	1793.2
8	$(42-44s)f$	2091.2	$(42-42s)f$	2091.6	$(42-40s)f$	2092.0
9	$(48-50s)f$	2390.0	$(48-48s)f$	2390.4	$(48-46s)f$	2390.8
10	$(54-56s)f$	2688.8	$(54-54s)f$	2689.2	$(54-52s)f$	2689.6

Table 6.4: Motor A theoretical results of axial vibrations by Muller [26].

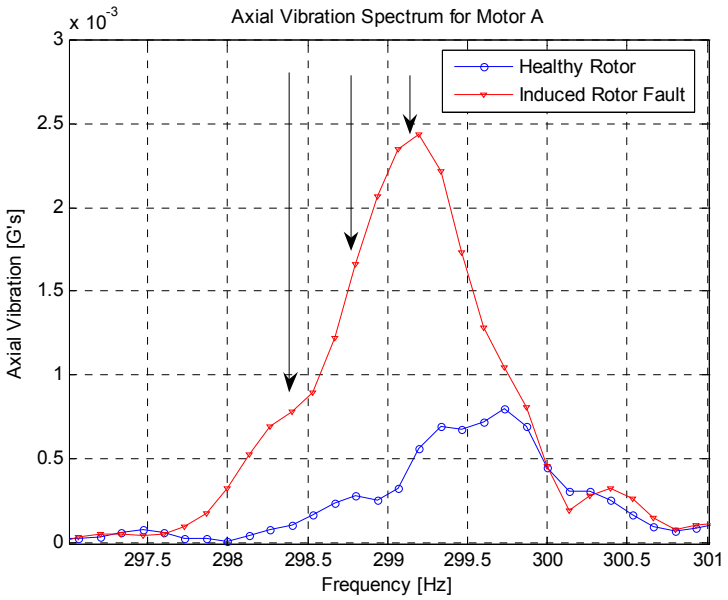


Figure 6.16: Motor A 1st group of axial vibrations fault frequencies

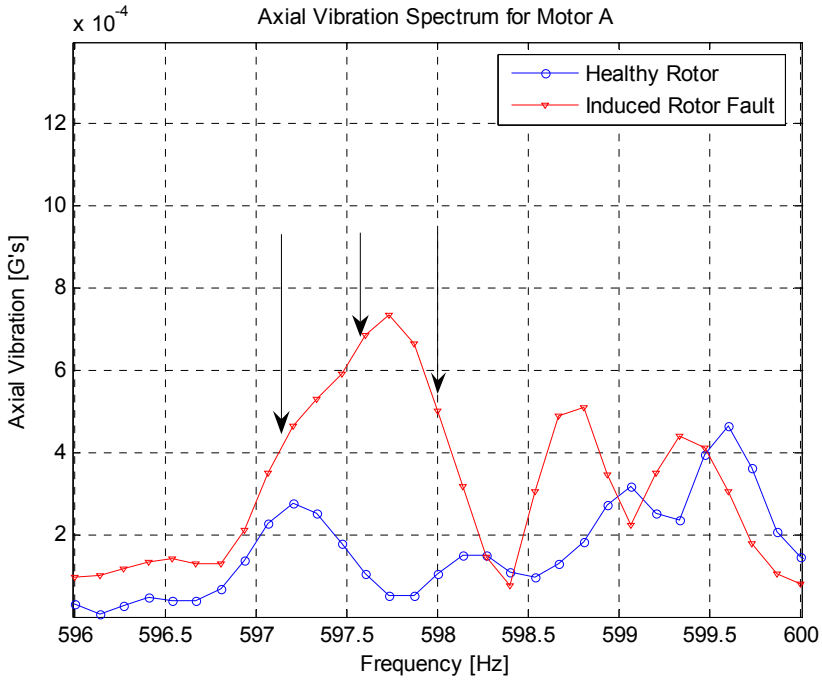


Figure 6.17: Motor A 2nd group of axial vibrations fault frequencies

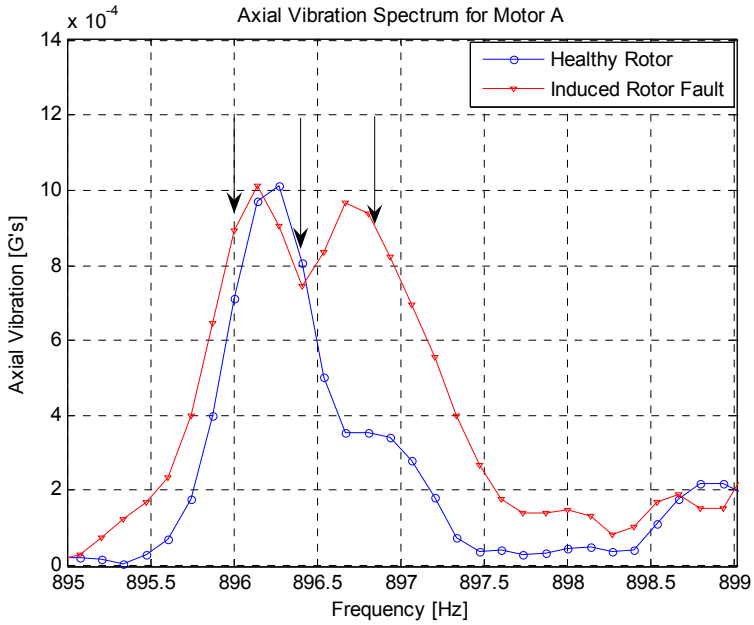


Figure 6.18: Motor A 3rd group of axial vibrations fault frequencies

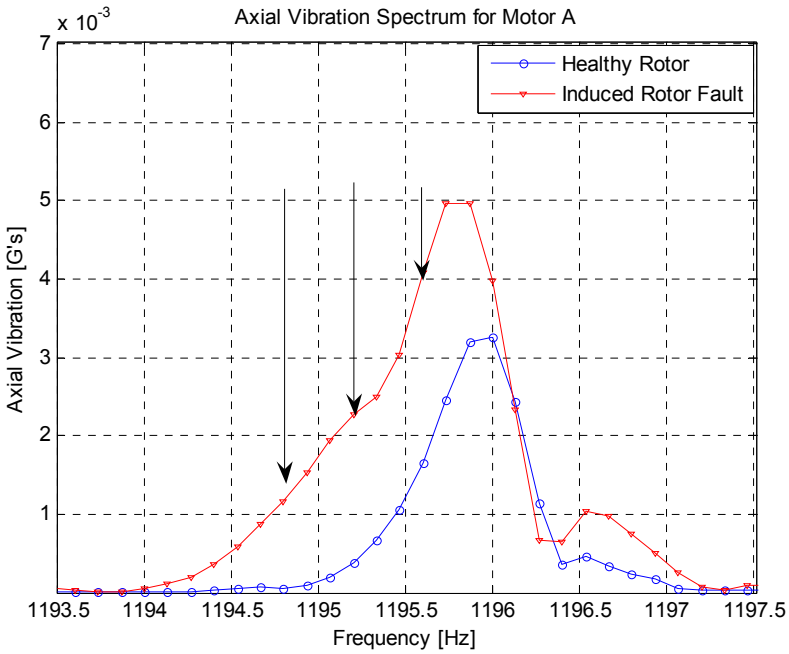


Figure 6.19: Motor A 4th group of axial vibrations fault frequencies

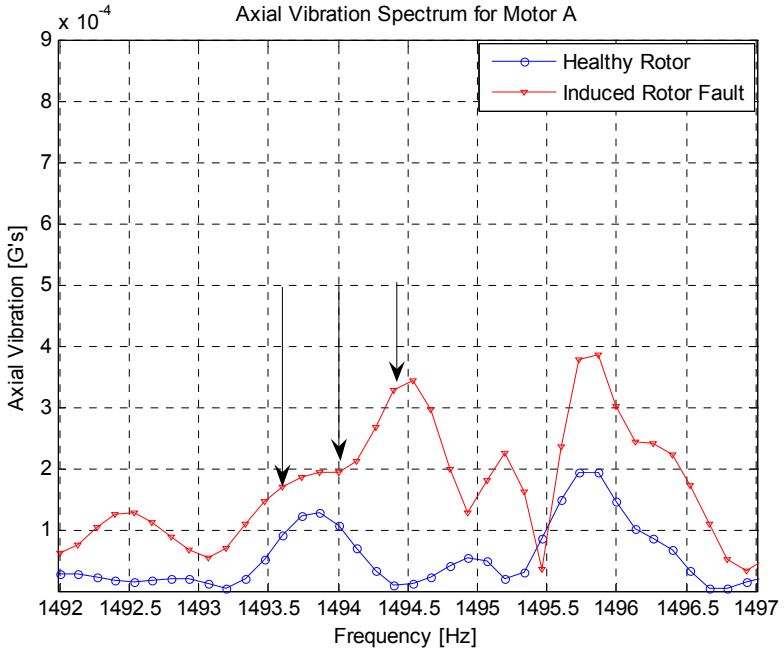


Figure 6.20: Motor A 5th group of axial vibrations fault frequencies

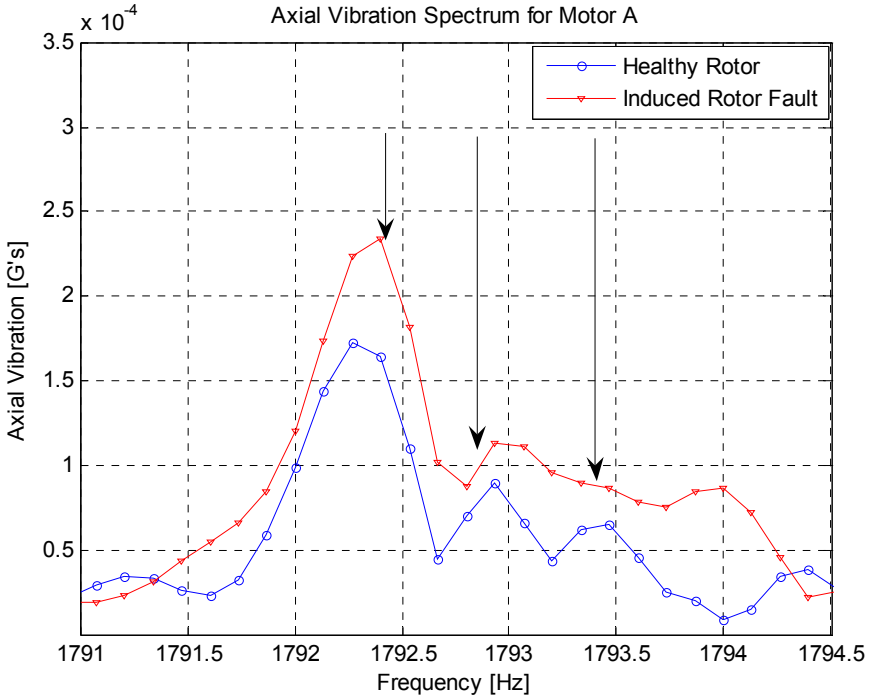


Figure 6.21: Motor A 6th group of axial vibrations fault frequencies

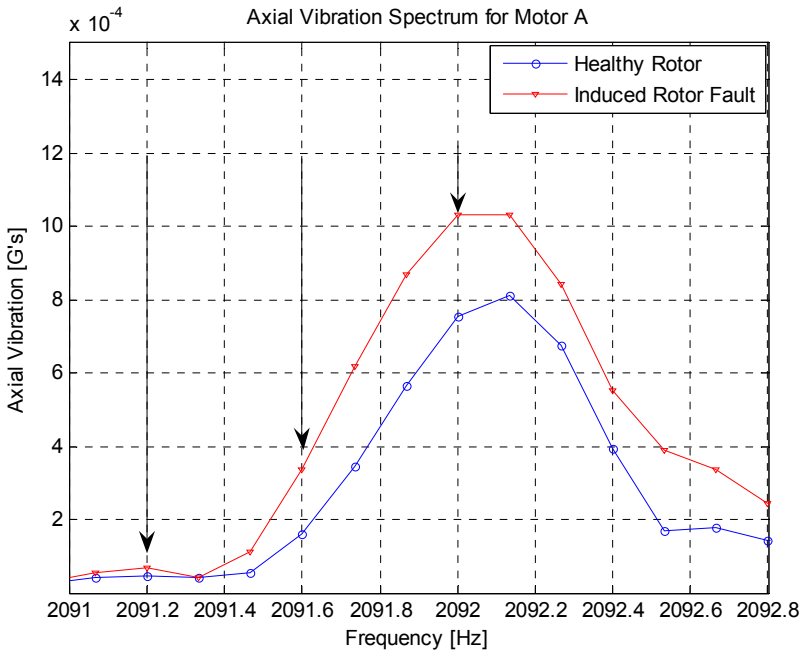


Figure 6.22: Motor A 7th group of axial vibrations fault frequencies

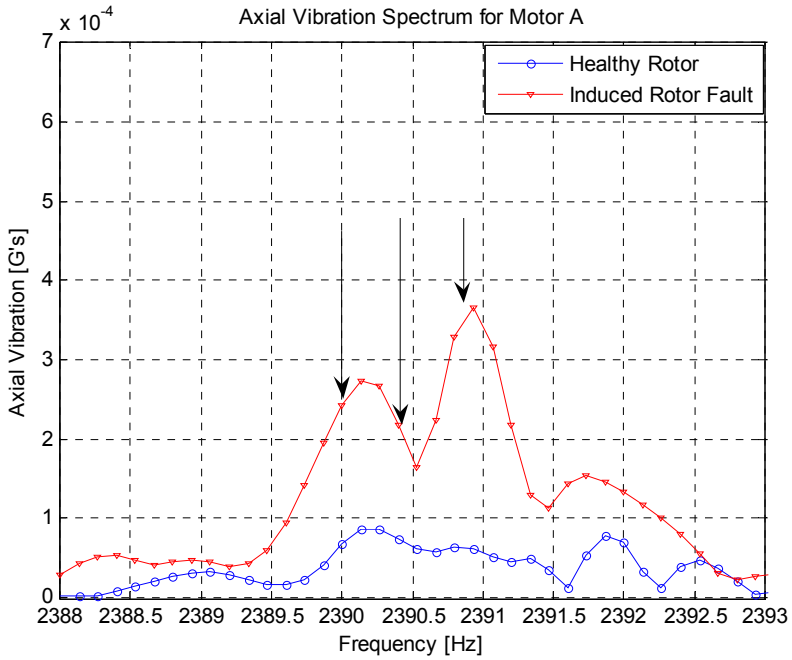


Figure 6.23: Motor A 8th group of axial vibrations fault frequencies

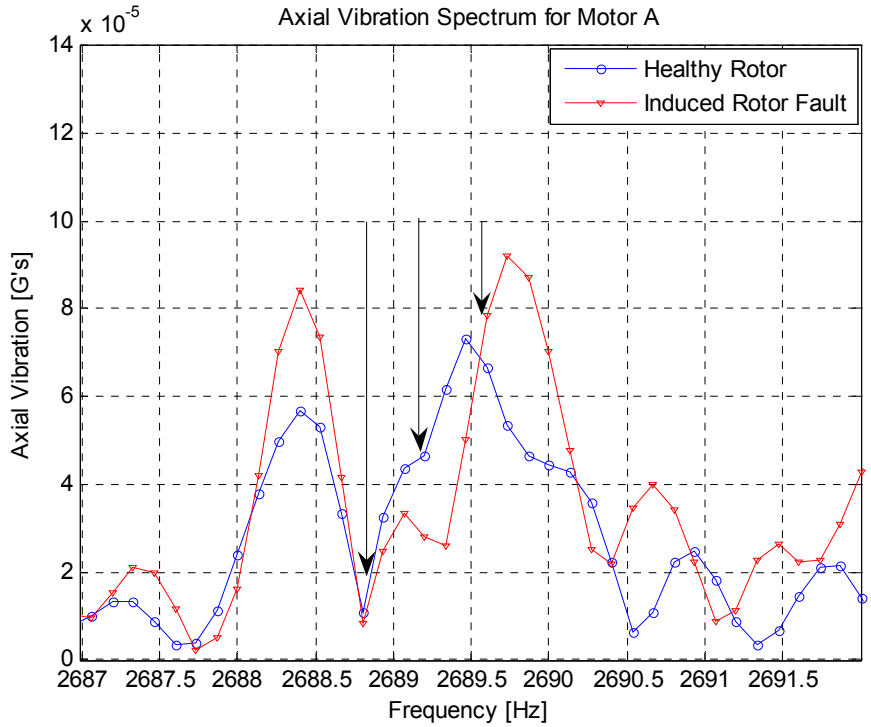


Figure 6.24: Motor A 9th group of axial vibrations fault frequencies

The axial vibration broken rotor bar detection frequencies recommended by Muller [24] are observed and indicated in the Motor A axial vibration spectra fig. 6.16 – 6.24.

6.3.2 Motor B Axial Vibration Analysis

Motor B was also tested under the same condition as Motor A above. Therefore, all the parameters, i.e. speed and slip, in Table 6.5 are still applicable for the Motor B axial vibration analysis.

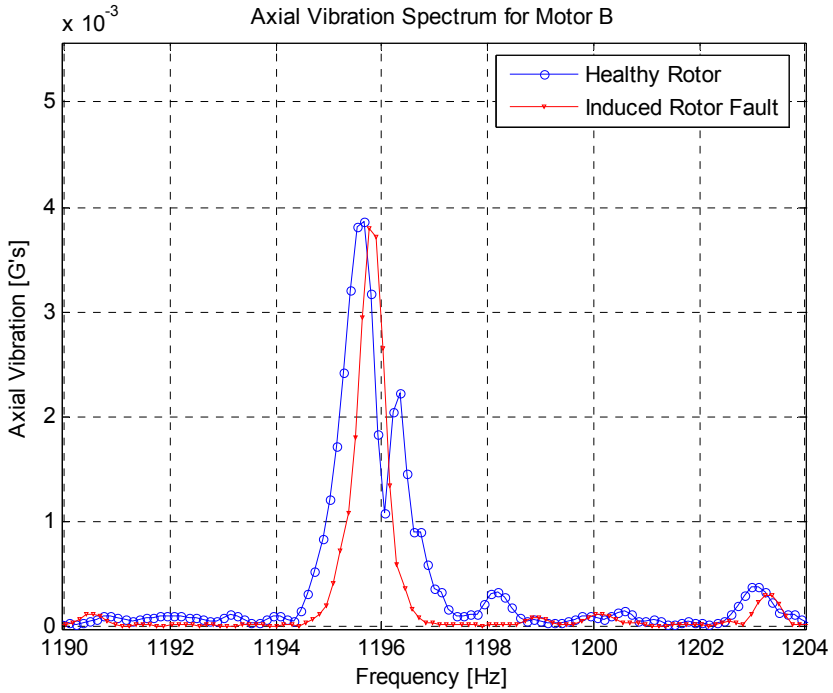


Figure 6.25: Motor B 4th group of axial vibrations fault frequencies

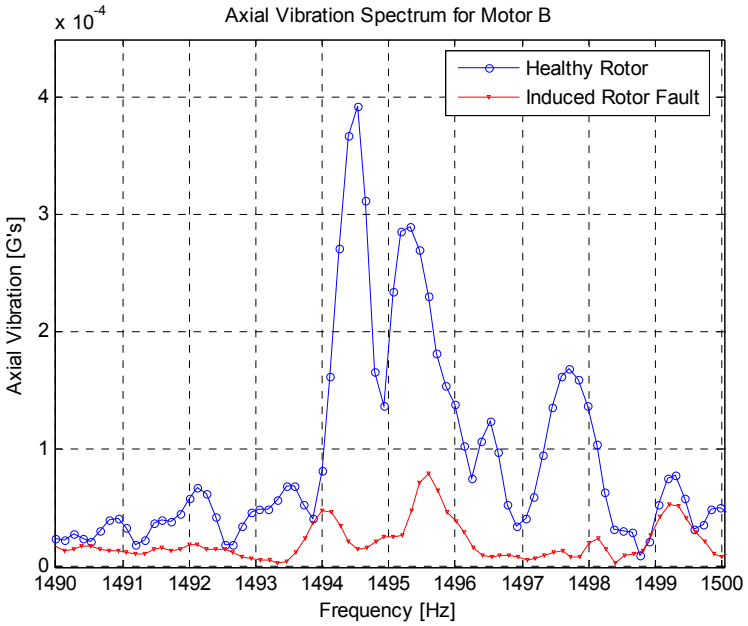


Figure 6.26: Motor B 5th group of axial vibrations fault frequencies

Fig. 6.25 – 6.26 which show axial vibrations spectra of Motor B show that there is no indication of a cracked or broken rotor bar fault. During the testing on Motor B, a bearing fault occurred which might have affected the axial vibration results above.

6.4 Other monitoring technique: shaft voltage analysis

Concurrently with this research, Dhuness [47] investigated a non-conventional technique that could be used for early detection of broken rotor bars. The non-conventional technique involved measuring shaft voltages of the induction motor.

Dhuness derived shaft voltage monitoring frequencies that should be monitored to detect broken rotor bars. The shaft voltage frequencies are given by:

$$f_c = f\left(s - q(1-s)\right) \tag{6.1}$$

where

q = 1,5,7,11,13,17…

Harmonic	Fault component
1	$(2s-1)f$
5	$(6s-5)f$
7	$(8s-7)f$
11	$(12s-11)f$
13	$(14s-13)f$
17	$(18s-17)f$
19	$(20s-19)f$
23	$(24s-23)f$
25	$(26s-25)f$
29	$(30s-29)f$
31	$(32s-31)f$
35	$(36s-35)f$

Table 6.5: Shaft voltage rotor bar detection frequencies

6.4.1 Motor A Shaft Voltage Analysis

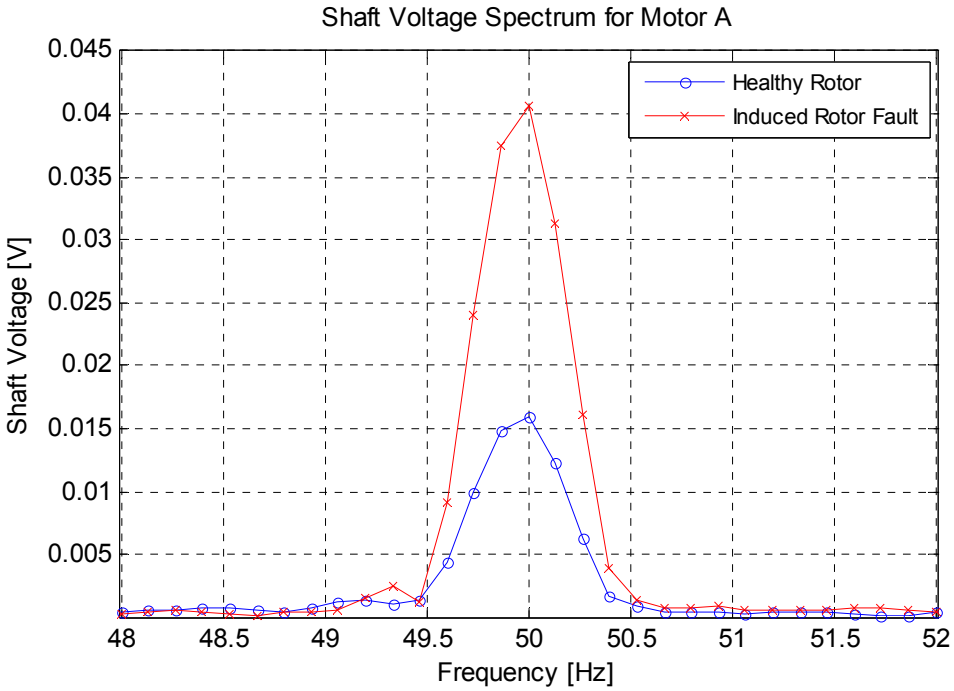


Figure 6.27: Motor A shaft voltage at 50 Hz (1st harmonic)

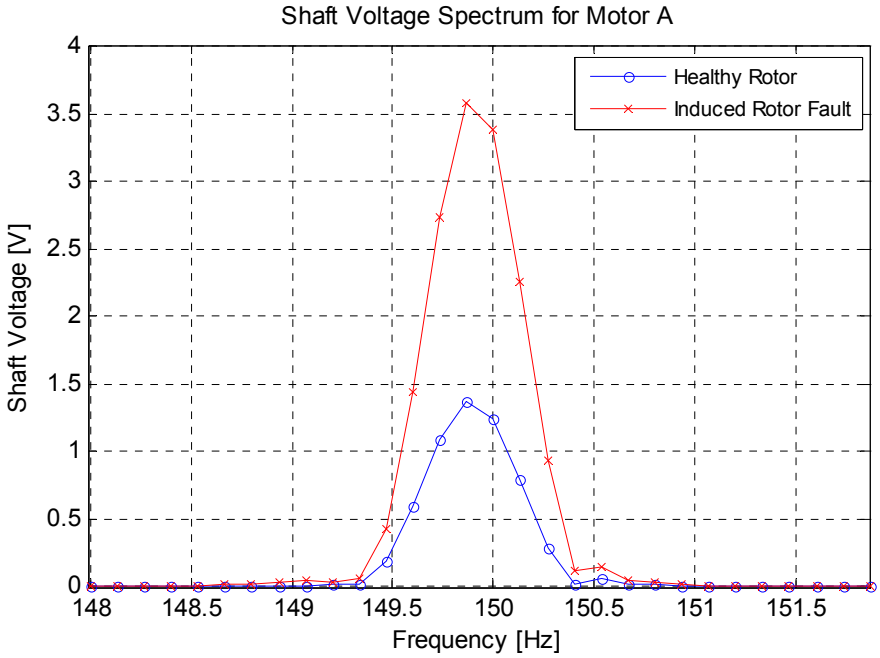


Figure 6.28: Motor A shaft voltage at 150 Hz (3rd harmonic)

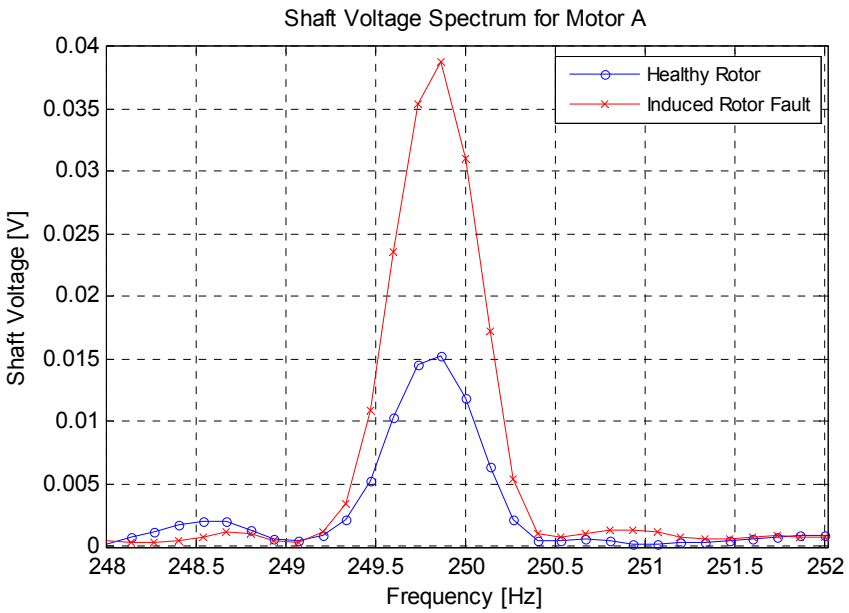


Figure 6.29: Motor A shaft voltage at 250 Hz (5th harmonic)

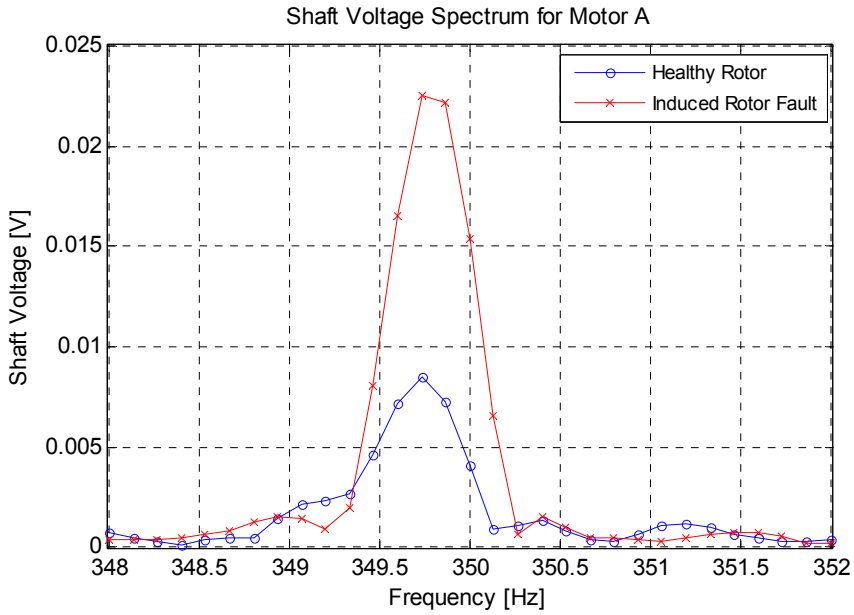


Figure 6.30: Motor A shaft voltage at 350 Hz (7th harmonic)

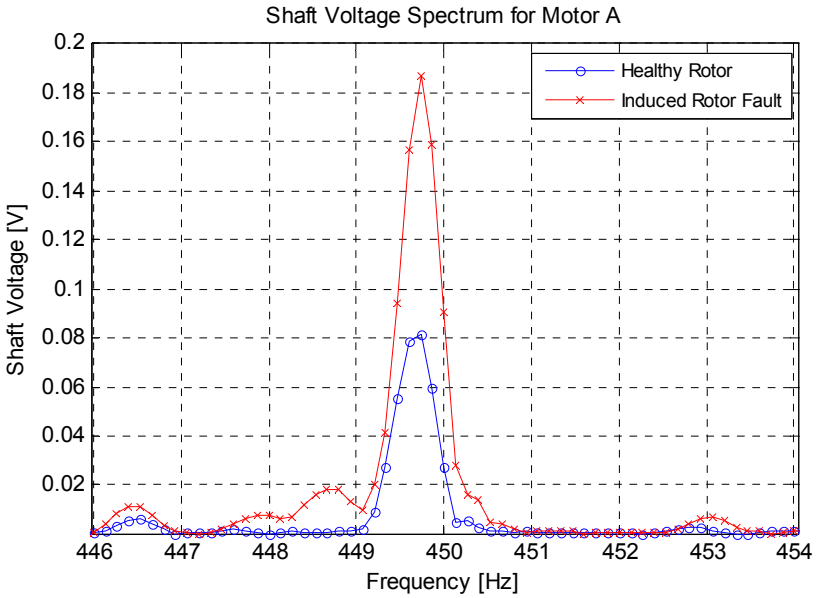


Figure 6.31: Motor A shaft voltage at 450 Hz (9th harmonic)

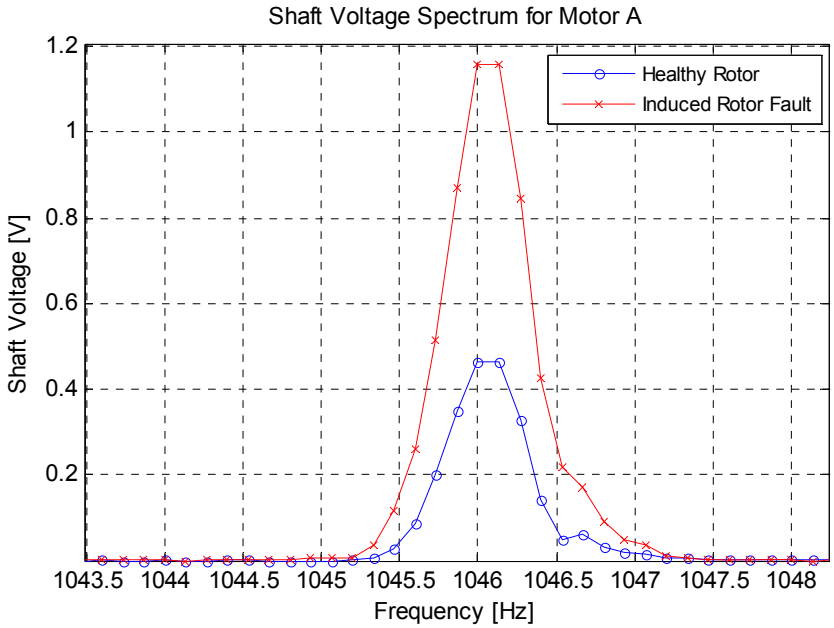


Figure 6.32: Motor A shaft voltage at 1050 Hz (21st harmonic)

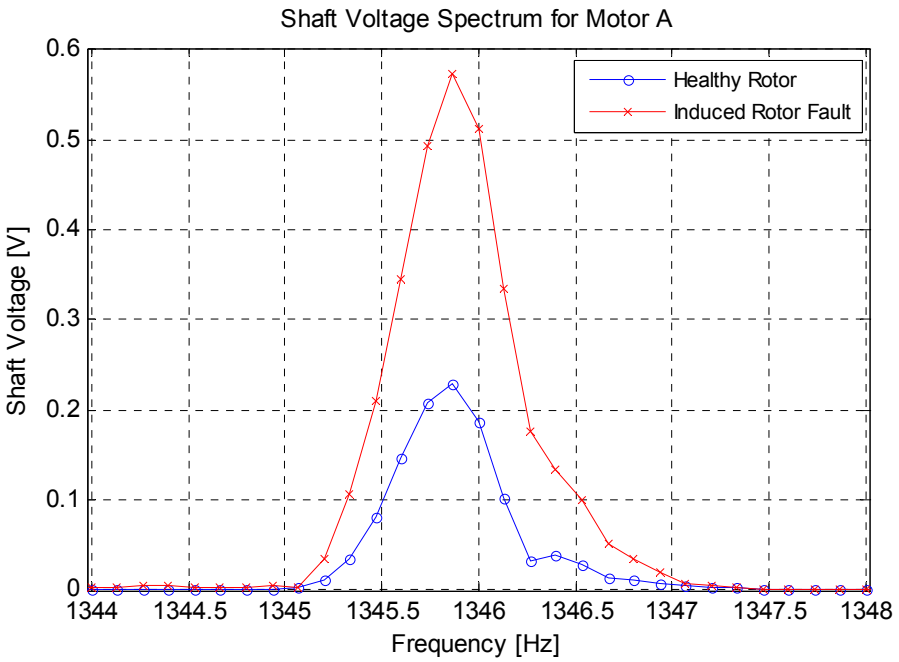


Figure 6.33: Motor A shaft voltage at 1350 Hz (27th harmonic)

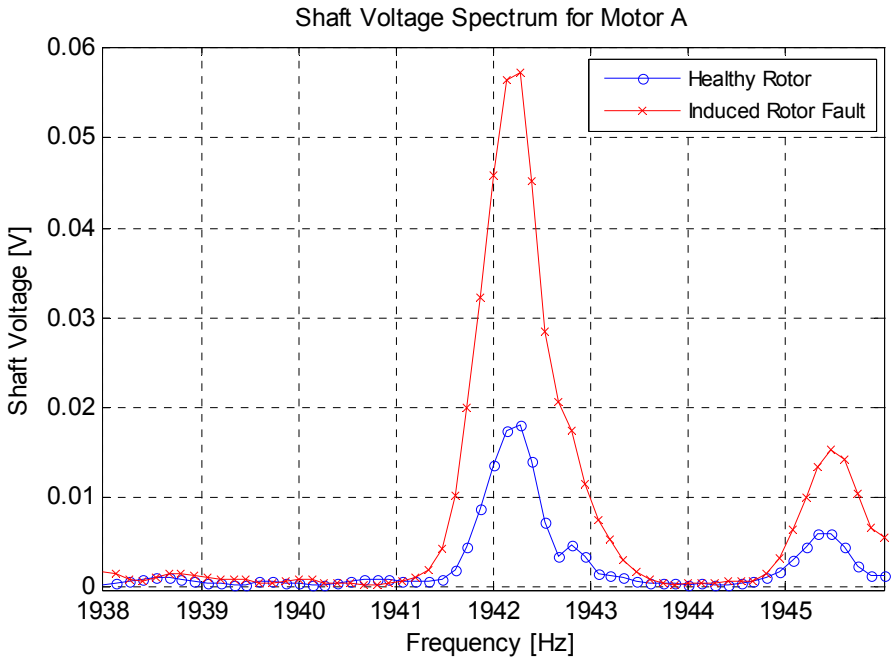


Figure 6.33: Motor A shaft voltage at 1950 Hz (39th harmonic)

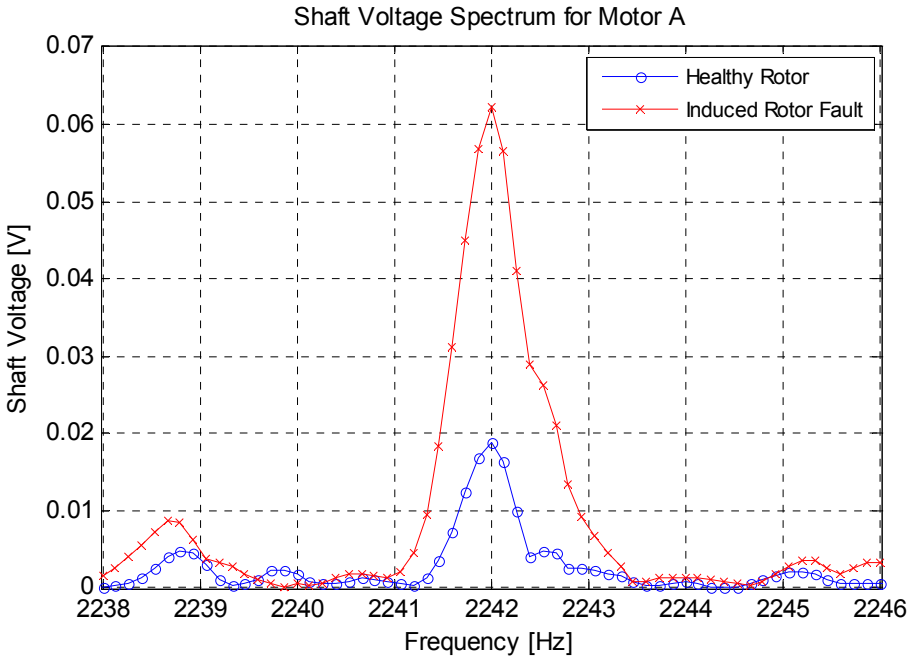


Figure 6.35: Motor A shaft voltage at 2250 Hz (45th harmonic)

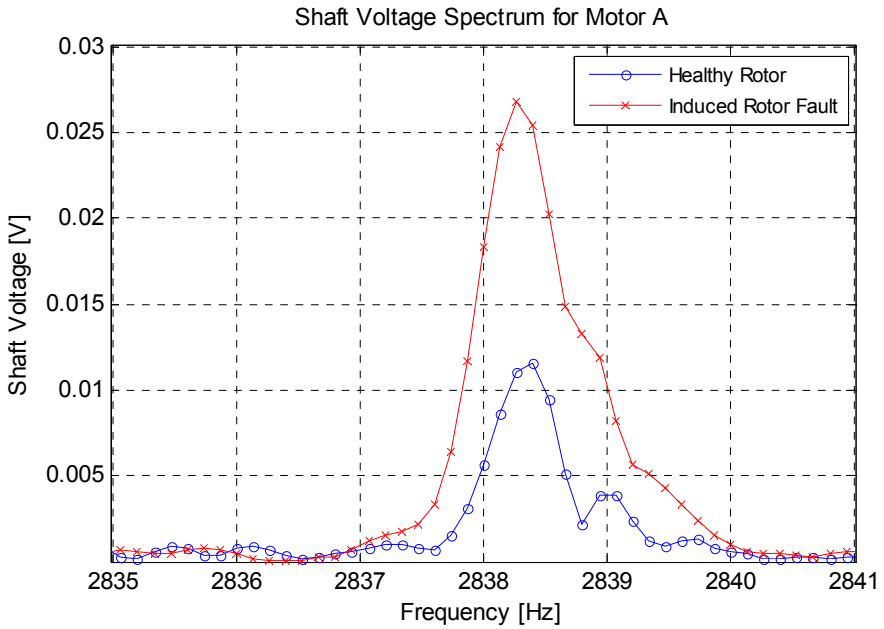


Figure 6.36: Motor A shaft voltage at 2850 Hz (57th harmonic)

The shaft voltage spectra show that there is a developing fault in the motor. This indicated by a high increases in the shaft voltage magnitudes.

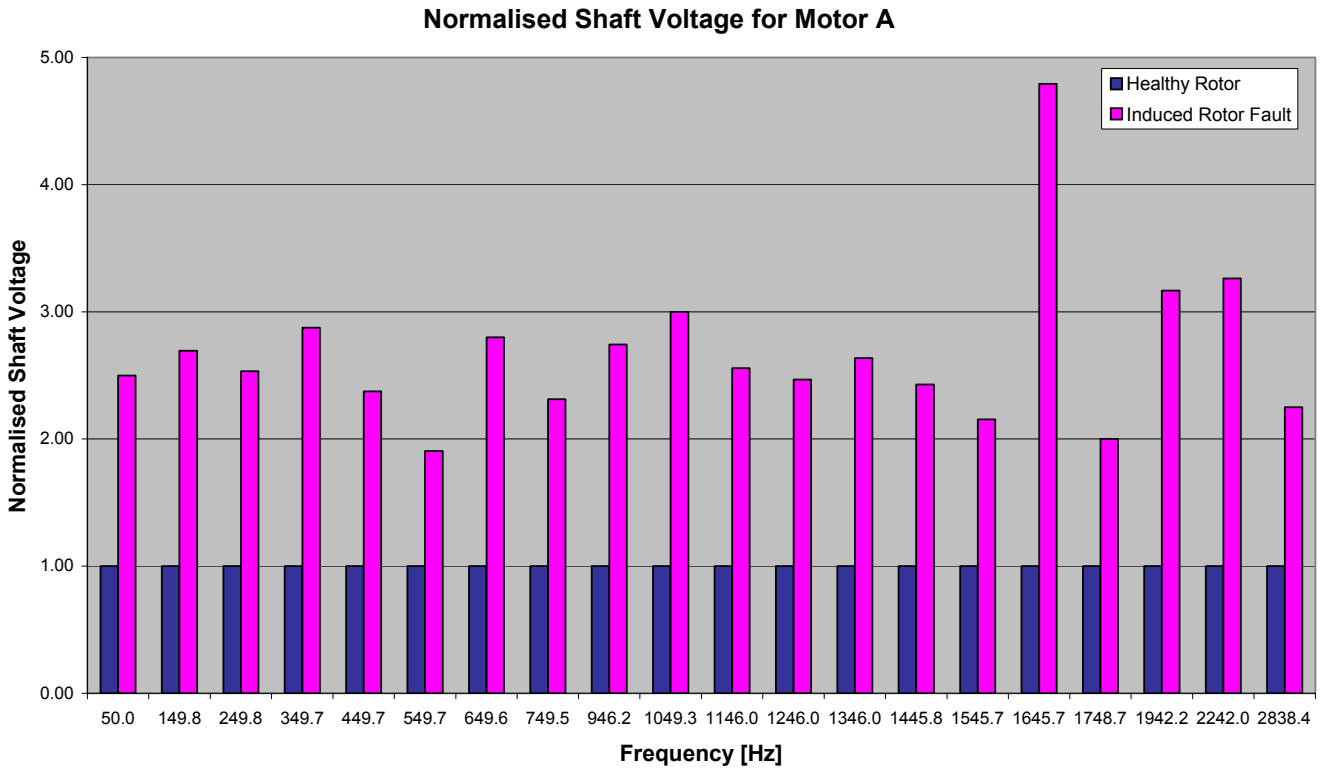


Figure 6.37: Normalised shaft voltage for Motor A at different frequencies

Figure 6.37 shows that there is at least a 2 times increase in the shaft voltages that indicates that there is a fault in motor A.

6.4.2 Motor B Shaft Voltage Analysis

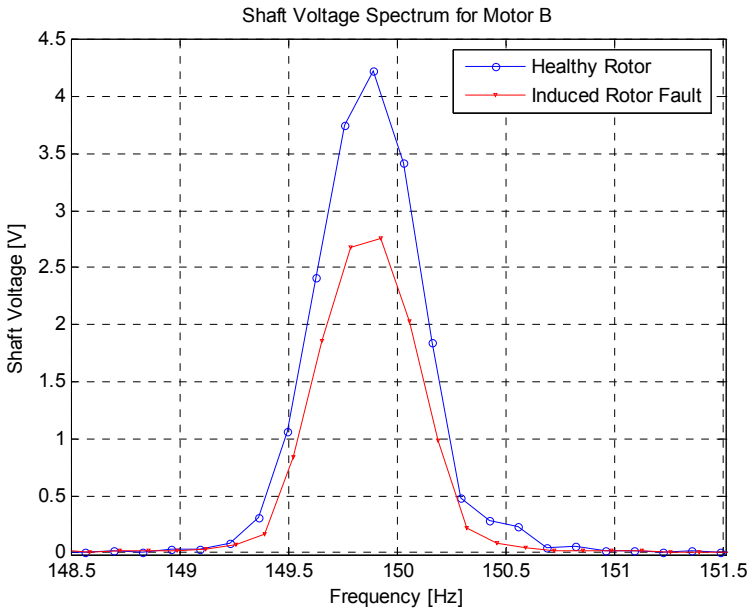


Figure 6.38: Motor B shaft voltage at 150 Hz (3rd harmonic)

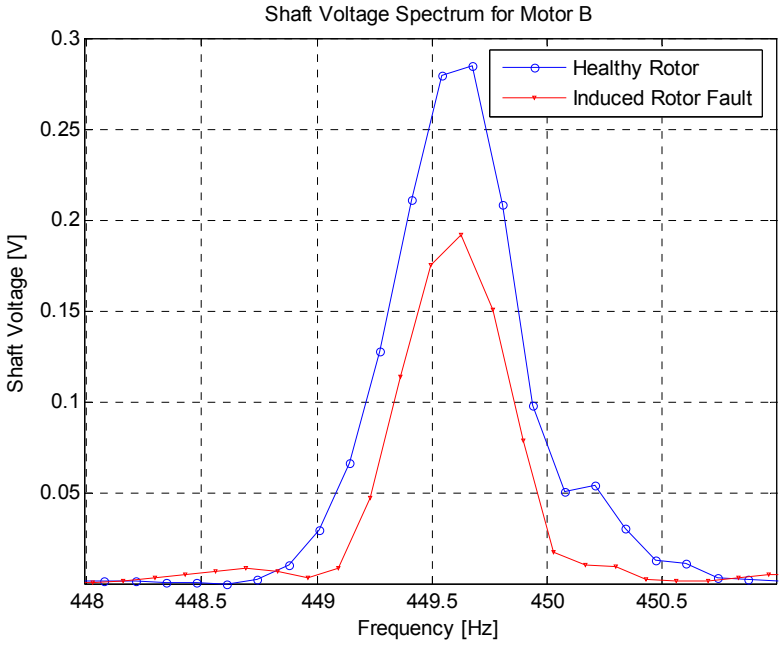


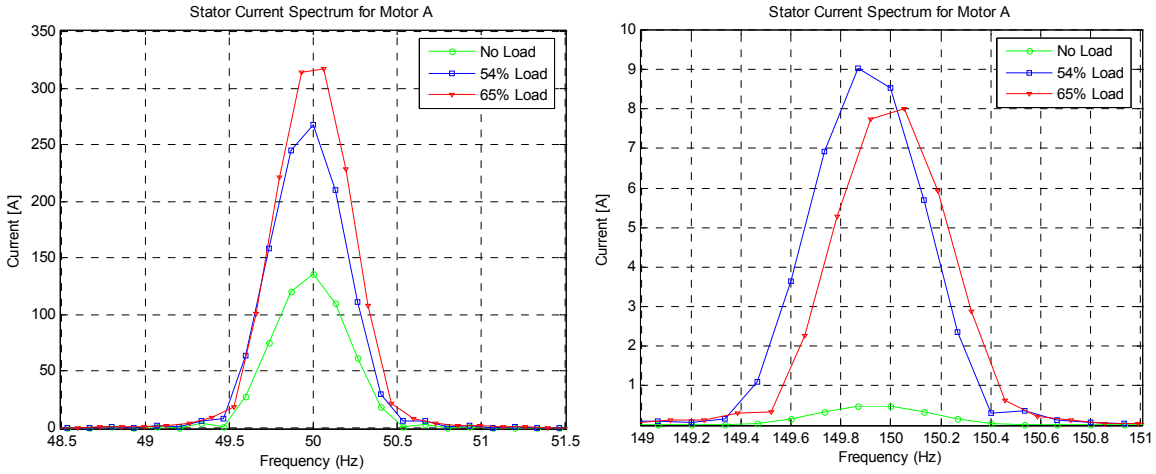
Figure 6.39: Motor B shaft voltage at 450 Hz (9th harmonic)

6.5 The Effects of Load

The motors were tested at different loads. This section shows and discusses the effect that varying loads had on the results. Furthermore, it present comparisons on stator currents, axial vibrations and shaft voltages for no-load, 54% load and 65 or 70% loads on Motor A and B.

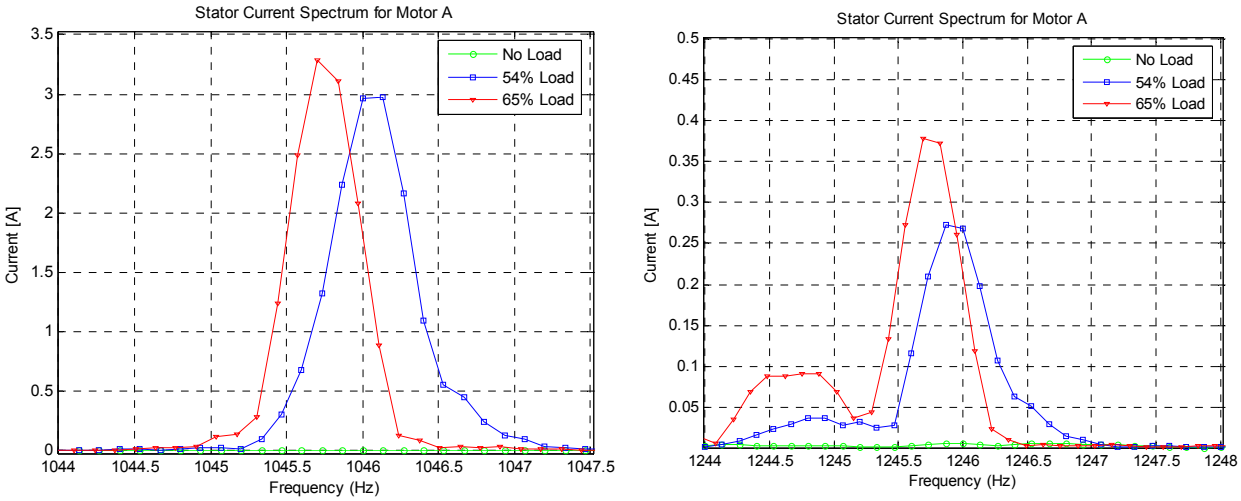
The experimental results which are used to outline the effect of load on detection of broken bars are those taken when there were faults induced onto the rotors.

6.5.1 Motor A Load Effects comparison



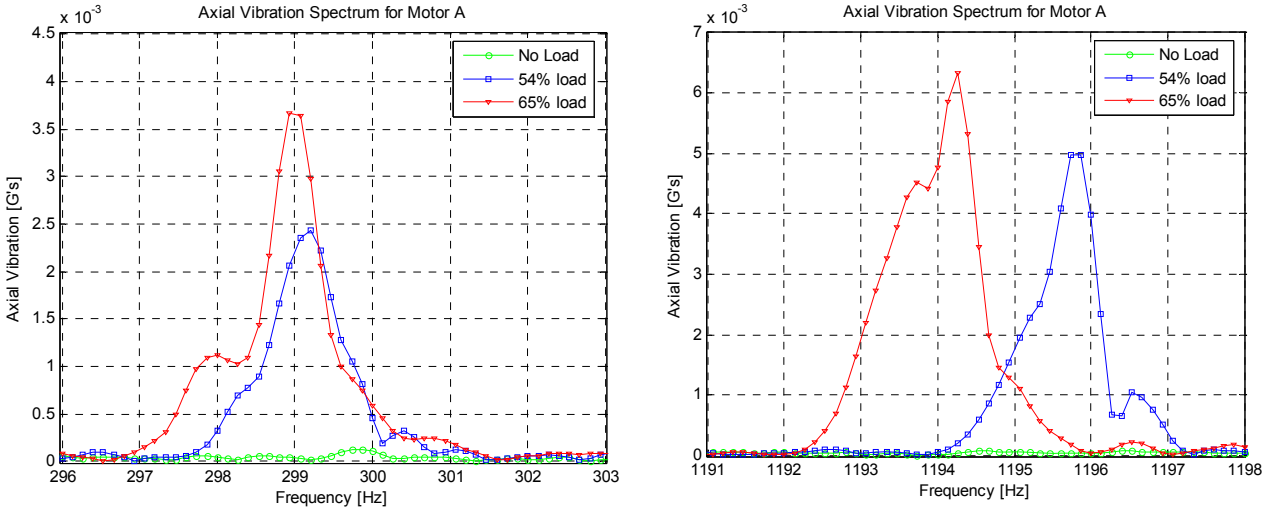
(a) (b)

Figure 6.40 (a) and (b): Stator current at different motor loads



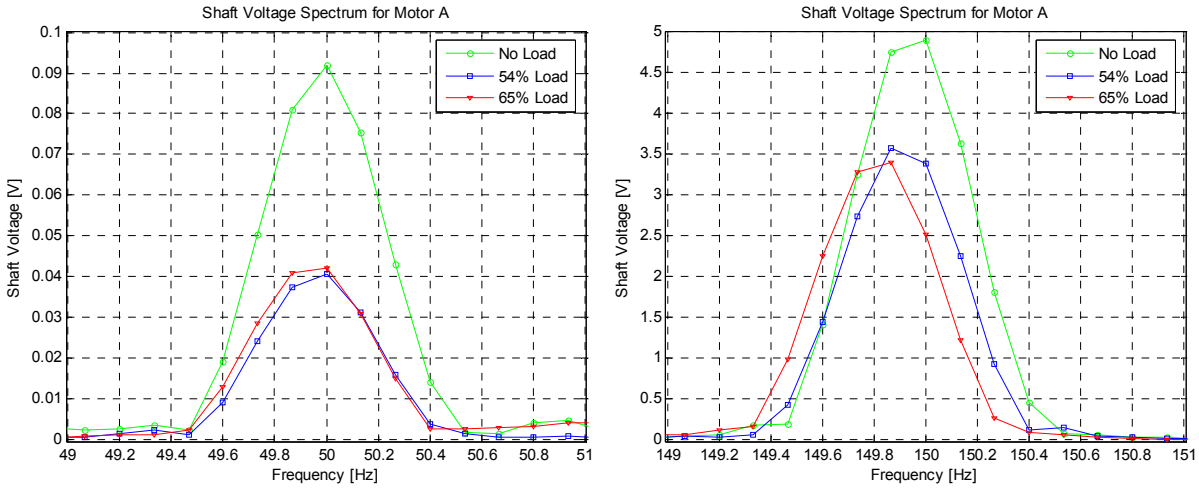
(a) (b)

Figure 6.41 (a) and (b): Stator current for Motor A at different loads



(a) (b)

Figure 6.42 (a) and (b): Axial vibrations at different motor loads



(a) (b)

Figures 6.43 (a) and (b): Shaft voltage at different motor loads

Figures 6.40 – 6.43 show the comparison of testing at different loads for rotor bar detection techniques examined. The degree of motor loading during the performance of the test plays an important role in correctly determining the condition of the rotor. The motor loading affects the thermal expansion of the crack or break consequently correct motor diagnosis. In conclusion, the higher the motor is loaded, the higher the probability of correct diagnosis.

6.6 Experimental Results Summary and Comparison

The results show that the stator current, axial vibration and shaft voltage in Motor A indicating that there is a developing fault in the motor. The techniques could detect a broken rotor bar as it was later revealed that the rotor had been intentionally broken for the experiment. During the performance of the

experiment on Motor B a bearing fault occurred which might have affected the results above. The stator current, however was not greatly affected by the developing bearing fault. The results of the stator current show some variations in the stator current fault frequencies but could not be correlated to any fault. Motor B was later revealed to have had a half broken bar fault induced on the rotor.

6.7 Experimental Results Conclusion

The theoretical rotor bar fault frequencies were observed in the experimental results in each technique with the stator current fault frequencies having been verified by the simulation.

Both Motor A and Motor B were verified to have had no broken rotor bars before commencing the experiment. Thereafter, in Motor A, a completely broken rotor bar fault was induced and in Motor B, a half broken rotor bar fault was induced.

The completely broken rotor bar fault, in Motor A, could be detected by the stator current analysis, axial vibration analysis and the shaft voltage analysis. However, the half broken rotor bar could not be detected in Motor B due to a bearing develop fault in the motor.

CHAPTER 7

CONCLUSION AND RECOMMENDEND FUTURE WORK

7.1 Research Report Summary

Chapter 1 outlined the overview of this research, states the problem statement and rotor bar failure mechanisms or rather causes of rotor bar/s breaks.

Chapter 2 highlighted previous researches and case studies conducted on detection of broken rotor bars which has assisted in better understanding of the existence of interbar currents and axial forces, factors influencing early detection of broken rotor bars and development of broken rotor bar detection techniques.

Chapter 3 discussed the literature and analysis of different broken rotor bar detection techniques. These detection phenomena originated from previous research presented in Chapter 2. The broken rotor bars identifying frequencies in each technique were also presented.

Chapter 4 presented modelling of a broken rotor bar simulation using Maxwell 2D. The simulation was performed to investigate the induction motor stator current that is how the sidebands change in a single broken bar rotor with respect to a healthy rotor.

Chapter 5 discussed the experimental work conducted to validate the literature and practical implementation of the techniques. This chapter explains the measuring process and the set up of the equipment used in the experimental work, capturing and analysis of data.

Chapter 6 presented the experimental results from the industrial tests performed on the research with discussions of measurements taken. Finally, Chapter 7

presents the conclusion and recommendations on the effective technique on detection of broken rotor bars during operation.

7.2 Research Report Conclusion

The main objective of this research was to determine an optimal technique for detection of a cracked and broken rotor bar in medium voltage motors during operation. Additionally, to give recommendations that can be used to develop guidelines for the implementation of the technique.

Based on the theory and experimental measurement results, presented on this report, the motor stator current analysis proved to be a more reliable rotor bar detection technique. Hence the motor stator current analysis was determined as an optimal technique for detection of broken rotor bar in medium voltage motors. The author recommends the utilization of the motor stator current analysis supported by axial vibration analysis with the following conditions:

1. The induction motor is loaded as high as possible but not less than 50% during taking of the measurements.
2. The measurements are to be taken and trended at the same load over a period of time depending on the criticality of the induction motor.
3. Baseline measurements are recommended on all medium voltage squirrel cage induction motors with one measurement for every six months taken thereafter for one year. Then the induction motor operations and number of starts the motor endures can be used to determine the frequency of measurements required.
4. Safety measures need to be enforced during the performance of measurements to ensure safety of the testing personnel as the motors will be tested on load.
5. The possibility of interbar currents being present in the motor should be investigated as they can influence the detection of a broken rotor bar. If

this information is not readily available, the possibility of interbar being present in the machine in question should be held in mind.

6. The number of stator slots and the number of rotor bars must be known in order to determine some of the fault frequencies to be observed during the measurements analysis.
7. Vibration measurements must be taken in the same motor bearing housing position. Vibrations are transmitted to the bearing housing as well as the stator frame but the bearing housing will give a better measurements. The type of bearings used in the motor also has an effect on the transmission of the exciting forces.

The shaft voltage analysis is a non-conventional technique that was investigated in this research. The shaft voltage analysis results show that the technique can be used to detect broken rotor bars in squirrel cage induction motors during operation but a further investigation is required to confirm reliability for diagnosis of large induction machines.

Stator current analysis is the optimal technique, presently, for early detection of a broken rotor bar under operating condition in medium voltage induction motors. The results for a cracked rotor bar did not yield any conclusive rotor bar detection diagnosis. Axial vibration analysis can be used as a secondary technique to stator current analysis. But it must be noted that the stator current analysis or any other technique cannot presently be used a one time diagnostic tool for a broken rotor bar, periodic non-intrusive trending is recommended.

7.3 Recommendations for further research

An investigation of axial flux (leakage) monitoring as an alternation technique for early detection of broken rotor bars is recommended with also more exploration of the shaft voltage analysis.

Zachas [42] showed that there is heating which follows the same distribution as the interbar currents and is concentrated at the unhealthy side of the broken rotor bar. He recommended utilisation of a thermal camera to evaluate the distribution of heat along a broken rotor bar. During the testing phase of this research, this was not explored but seems to be a consideration for future testing. This may seem to be a much quicker way to non-invasively detect broken rotor bars in motors when interbar currents are present.

The currently available technology, which is normally utilized in the industry need to be investigated and is presented in this report Appendix E but more technology, needs to be developed for detection of broken rotor bars.

There is a need to set up a standard for performance of each broken rotor bar detection technique. Furthermore, compilation of a guideline for analysing the data captured for the tests, indicating which frequencies correlate to broken rotor bar.

Training of condition monitoring personnel in terms of performing the detection techniques, data capturing and analysis is highly recommended with the information presented in this research report.

The author hopes that the research report recommendations assist in early detection of a cracked and a single broken rotor bar on-line during operation without intrusion to the motor.

APPENDIX A

MAXWELL 2D: INDUCTION MOTOR SIMULATION

A.1 General Procedure for creating and solving a 2D Model

This section informs of the general procedure that was followed when using the Maxwell 2D to create and solve a 2D problem.

- A **Solver** command is used to specify the electric or magnetic field quantity to be computed. The field quantities that can be computed depend on the field solver type required. The solver types include:
    - **Electrostatic** which is used for static electric fields.
    - **Magnetostatic** which is used for static magnetic fields.
    - **Eddy Currents** which computes time-varying fields and eddy currents.
    - **DC Conduction** which computes conduction currents caused by DC voltage differentials.
    - **StaticThermal** which solves thermal quantities of devices.
    - **AC Conduction** which computes conduction currents caused by AC voltage differentials.
    - **Eddy Axial** which computes eddy currents induced in a time-varying magnetic fields.
    - **Transient** is used for time-varying fields.

- A **Drawing** command is used to select the model types whether XY plane or RZ plane:
    - **XY Plane**: Visualise Cartesian models as sweeping perpendicularly to the cross-section.
    - **RZ Plane**: Visualise axisymmetric models as revolving around an axis of symmetry in the cross-section.

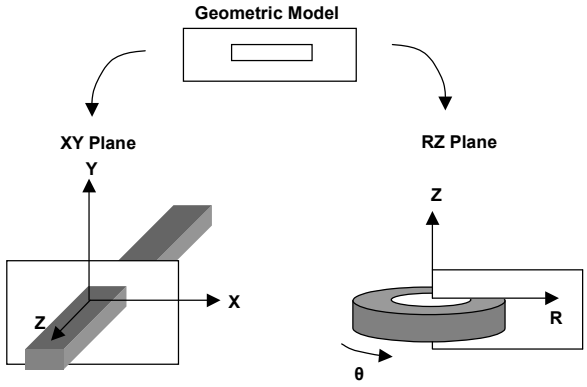


Figure A.1: XY and RZ geometric model planes

- A **Define Model** command is used to create the geometric model. In the Define Model the following are used:
    - **Draw Model**: Allows for accessing the 2D Modeler and for building the objects that make-up the geometric model.
    - **Group Objects**: Allows for grouping discrete objects that are actually one electrical object.

- A **Setup Material** command is used to assign materials to all objects in the geometric model.

- A **Setup Boundaries/Sources** command is used to define the boundaries and sources for the problem. This determines the electromagnetic excitations and field behaviour for the model.

- A **Setup Executive Parameters** command to instruct the simulator to compute on or more of the following special quantities during the solution process:
    - Matrix (capacitance, inductance, admittance, impedance, or conductance matrix, depending on the selected solver).
    - Force

    - Torque
    - Flux Linkage
    - Post Processor macros
    - Current flow
- A **Setup Solution/Options** command is used to enter parameters that affect how the solution is computed.

- A **Setup Solution/Motion Setup** command to define the motion parameters of the system.

- A **Solve/Nominal Problem** command is used to solve the appropriate field quantities.

- A **Post Processor** command is used to analyse the solution.

These commands must be chosen in the sequence presented above or as they appear on the Maxwell 2D.

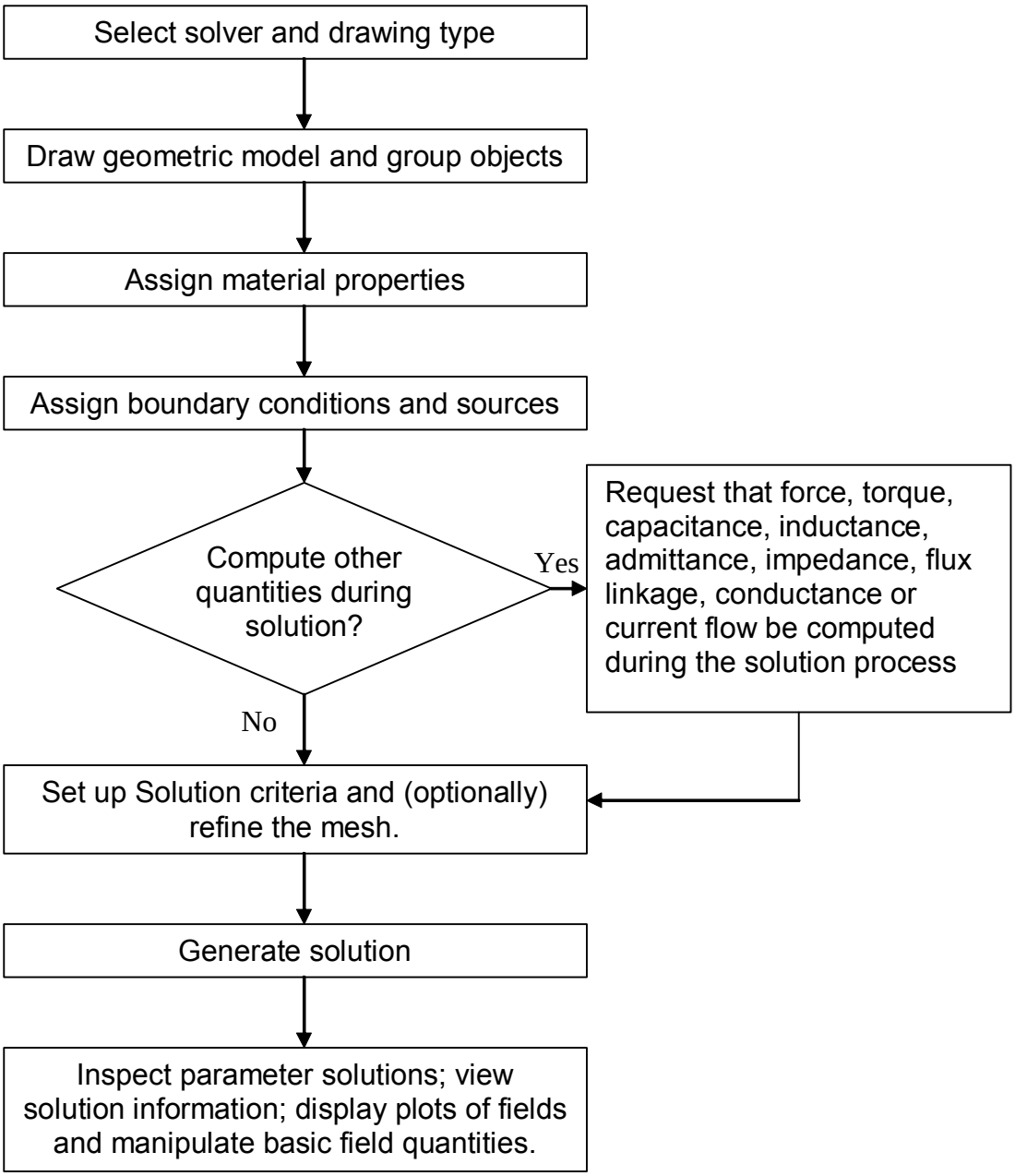


Figure A.2: Flow diagram of creating and solving a Maxwell 2D Model

APPENDIX B

DS1104 R&D CONTROLLER BOARD SPECIFICATIONS

Parameter	Characteristics
Processor	• MPC8240 processor with PPC603e and on-chip peripherals • 64-bit floating-point processor • 250MHz CPU • 2x16KB cache; on chip • A PCI interface (5 V, 32 bit, 33 MHz)
Memory	• Global memory: 32 MB SDRAM • Flash memory: 8 MB
Timer	• 1 sample rate timer (decrementer) 32-bit down counter, reload by software, 40 ns resolution • 4 general purpose timer 32-bit down counter, reload by hardware, 80 ns resolution • 1 time base timer 64-bit up counter, 40 ns resolution, range 23400 years
Interrupt controller	• 5 timer interrupts • 2 incremental encoder index line interrupts • 1 UART interrupt • 1 slave DSP interrupt • 1 slave DSP PWM interrupt • 5 ADC end conversion interrupts • 1 host interrupt • 4 user interrupts form the I/O connector
ADC 1 x 16-bit ADC mux	• 4 muxed channels equipped with one 16-bit sample & hold ADC Note: 5 ADC channels (1 x 16-bit + 4 X 12-bit) can be sampled • 16-bit resolution • ±10 V input voltage range • 2 µs conversion timer • ± 5mV offset error • ± 0.25% gain error • 4 ppm/K offset drift • 25 ppm/K gain drift • > 80 dB signal-to-noise ratio (SNR)
ADC 4 x 12-bit ADC	• 4 channels equipped with one 12-bit sample & hold ADC Note: 5 ADC channels (1 x 16-bit + 4 X 12-bit) can be sampled • 12-bit resolution • ±10 V input voltage range • 80 ns conversion timer • ± 5mV offset error • ± 0.5% gain error • 4 ppm/K offset drift • 25 ppm/K gain drift • > 65 dB signal-to-noise ratio (SNR)
DACs 8 x 16-bit DAC	• 16-bit resolution • ±10 V output voltage range • ± 5 mA maximum output current • Max. 10 s settling time (full scale, accuracy 1/2LSB) • ± 1 mV offset error • ± 0.1% gain error • 13 ppm/K offset drift

	• 25 ppm/K gain drift • 80 dB signal-to-noise ratio (SNR)
Digital I/O	• 20-bit digital I/O • Single bit selectable for input or output • ±5 mA maximum output current • TTL voltage range for input and output
Digital Incremental Encoder Interface (2 x 24 bit)	• 2 channels • Selectable single-ended TTL or differential (RS422) input • Fourfold line subdivision • Max. 1.65 MHz input frequency, i.e. fourfold pulse counts up to 6.6 MHz • 24-bit loadable position counter • Reset on index • 5V/0.1A sensor supply voltage
Serial interface	• 1 serial UART (universal asynchronous receiver and transmitter) • Selectable transceiver mode: RS232/ RS422/ RS485 • Max. baudrate RS232: 115.2 kBaud • Max. baudrate RS422/ RS485: 1 MBaud
Slave DSP subsystem	• Texas Instruments TMS320F240 DSP • 16-bit fixed-point processor • 20 MHz clock frequency • 64 K x 16 external program memory • 28 K x 16 external data memory • 4 K x 16 bit dual-port memory for communication • 16 K x 16 flash memory • 1 x 3-phase PWM output • 4 x 1-phase PWM output • 4 capture inputs • SPI (serial peripheral interface) • Max. 14-bit digital I/O • TTL output/input levels for all digital I/O pins • ±13 mA maximum output current
Host interface	• 32-bit PCI host interface • 5 V PCI slot • 33 MHz ±5%.
Physical size	PCI 185 x 106.68 mm
Ambient temperature	0 … 55 ºC (32 … 131 ºF)
Cooling	Active cooling by fan
Power supply	• +5V ±5%, 2.5 A • +12V ±5%, 0.3 A • -12V ±5%, 0.2 A
Power Consumption	18.5 W

Table B.1: The data sheet of the DS1104 R&D Controller Board

APPENDIX C

DATA PROCESSING MATLAB CODES

C.1 The Matlab FFT Function used for data processing [47]

```
%-------------------------------------------------------
%          Computing FFT
%-------------------------------------------------------
{

function [frequency,amplitude,phase] = FFT(signal,samplingfrequency)

Signallenght=length(signal);

absamplitude =abs(fft(signal));

halfabsamplitude=absamplitude(1,(1:round(Signallenght/2)+1) );

amplitude=(halfabsamplitude/(Signallenght/2));

frequency = samplingfrequency*(0:round(Signallenght/2))/Signallenght;

ph=angle(fft(signal)/ Signallenght);    %phase angle of fft

phase=ph(1:round(Signallenght/2)+1);    %discard half f

}
```

C.2 Measured Signal Processing

```
load ('D:\...\54_load_ 6-4s_1ds.Y.Data ');% 54% load data sampled at 40kHz
sc54_40_1a=54_load_6-4s_1ds.Y(1,5).Data; %red phase line current
sc54_40_1b=54_load_6-4s_1ds.Y(1,7).Data; % white phase line current
sc54_40_1c=54_load_6-4s_1ds.Y(1,4).Data; % blue phase line current
vb54_40_1a=54_load_6-4s_1ds.Y(1,1).Data; %axial vibration
vb54_40_1b=54_load_6-4s_1ds.Y(1,2).Data; %radial vibration
sh54_40_1=54_load_6-4s_1ds.Y(1,3).Data; % shaft voltage
speed54_40_1=54_load_6-4s_1ds.Y(1,6).Data; % speed of the shaft
time54_40_1=54_load_6-4s_1ds.X.Data;

%The Matlab code used to perform the FFT through all process in [47]

N = 200000;          %N : Number of FFT points
w=hann(N);
overlap=[];
cf=15e3;             %  cf: cut-off frequency in Hz
Fs=40e3;             %  Fs: Sampling Frequency in Hz
[b,a]=butter(3,(cf/(Fs/2)),'low');
Shsum=sc54_40_1a;
yShsum=filter(b,a,Shsum);
clear Shsum
winyShsum=2*w'.*yShsum(1,1:N);
sizewindow=size(winyShsum);
wShsum=zeros(1,sizewindow(1,2)*2);
wShsum(1,1:sizewindow(1,2))=winyShsum;
clear winyShsum;
cu54_40_1a=wShsum;
[fShsum,PyyShsum,phase]=FFT(cu54_40_1a,Fs);
figure;
```

```
plot(fShsum,2*PyyShsum);
grid
xlabel('Frequency  [Hz]');
ylabel('Current  [A]');
title('Stator Current Spectrum for Motor A');
clear all
clc
 %-------------------------------------------------------
```

The signal processing was then performed for each of the following signals: current, shaft voltage, axial vibration and speed which were then used in the experimental results in Chapter 6.

APPENDIX D

ADDITIONAL THEORETICAL AND INDUSTRIAL MEASUREMENTS RESULTS

In this section, additional theoretical and industrial measurement results are presented.

D.1 Stator Current Analysis

The stator current theoretical results for the motor loaded at 65% and 70% are presented in Table D1 and D2 respectively.

Harmonic	Lower Component $f_{lsb} = f\left[\left(\frac{k}{p}\right)(1-s)-s\right]$	Frequency (Hz)	Upper Component $f_{usb} = f\left[\left(\frac{k}{p}\right)(1-s)+s\right]$	Frequency (Hz)
1	$(1-2s)f$	49.53	f	50.0
3	$(3-4s)f$	149.07	$(3-2s)f$	149.53
5	$(5-6s)f$	248.60	$(5-4s)f$	249.07
7	$(7-8s)f$	348.13	$(7-6s)f$	348.60
9	$(9-10s)f$	447.67	$(9-8s)f$	448.13
11	$(11-12s)f$	547.20	$(11-10s)f$	547.67
13	$(13-14s)f$	646.73	$(13-12s)f$	647.20
15	$(15-16s)f$	746.27	$(15-14s)f$	746.73
17	$(17-18s)f$	845.80	$(17-16s)f$	845.27
19	$(19-20s)f$	945.33	$(19-18s)f$	945.80
21	$(21-22s)f$	1044.87	$(21-20s)f$	1045.33
23	$(23-24s)f$	1144.40	$(23-22s)f$	1144.87
25	$(25-26s)f$	1243.93	$(25-24s)f$	1244.40
27	$(27-28s)f$	1343.47	$(27-26s)f$	1343.93
29	$(29-30s)f$	1443.00	$(29-28s)f$	1443.47
31	$(31-32s)f$	1542.53	$(31-30s)f$	1543.00
33	$(33-34s)f$	1642.07	$(33-32s)f$	1641.53
35	$(35-36s)f$	1741.60	$(35-34s)f$	1742.07
37	$(37-38s)f$	1841.13	$(37-36s)f$	1841.60
39	$(39-40s)f$	1940.67	$(39-38s)f$	1941.13
41	$(41-42s)f$	2040.20	$(41-40s)f$	2040.67
43	$(43-44s)f$	2139.73	$(43-42s)f$	2140.20
45	$(45-46s)f$	2239.27	$(45-44s)f$	2239.73
47	$(47-48s)f$	2338.80	$(47-46s)f$	2339.27
49	$(49-50s)f$	2437.87	$(49-48s)f$	2438.80
51	$(51-52s)f$	2536.13	$(51-50s)f$	2538.33
53	$(53-54s)f$	2637.40	$(53-52s)f$	2637.87
55	$(55-56s)f$	2736.93	$(55-54s)f$	2735.60
57	$(57-58s)f$	2836.47	$(57-56s)f$	2836.93
59	$(59-60s)f$	2936.00	$(59-58s)f$	2936.47
61	$(61-62s)f$	3035.53	$(61-60s)f$	3036.00

Table D1: Theoretical Stator Current for 65% Load at s = 0.0047

Harmonic	Lower Component $f_{lsb} = f\left[\left(\frac{k}{p}\right)(1-s)-s\right]$	Frequency (Hz)	Upper Component $f_{usb} = f\left[\left(\frac{k}{p}\right)(1-s)+s\right]$	Frequency (Hz)
1	$(1-2s)f$	49.47	f	50.0
3	$(3-4s)f$	148.93	$(3-2s)f$	149.47
5	$(5-6s)f$	248.40	$(5-4s)f$	248.93
7	$(7-8s)f$	347.87	$(7-6s)f$	348.40
9	$(9-10s)f$	447.33	$(9-8s)f$	447.87
11	$(11-12s)f$	546.80	$(11-10s)f$	547.33
13	$(13-14s)f$	646.27	$(13-12s)f$	646.80
15	$(15-16s)f$	745.73	$(15-14s)f$	746.26
17	$(17-18s)f$	845.20	$(17-16s)f$	845.73
19	$(19-20s)f$	944.67	$(19-18s)f$	945.20
21	$(21-22s)f$	1044.13	$(21-20s)f$	1044.67
23	$(23-24s)f$	1144.60	$(23-22s)f$	1144.13
25	$(25-26s)f$	1243.07	$(25-24s)f$	1245.2
27	$(27-28s)f$	1342.53	$(27-26s)f$	1344.8
29	$(29-30s)f$	1442.00	$(29-28s)f$	1442.53
31	$(31-32s)f$	1541.47	$(31-30s)f$	1542.00
33	$(33-34s)f$	1640.93	$(33-32s)f$	1641.47
35	$(35-36s)f$	1740.40	$(35-34s)f$	1740.93
37	$(37-38s)f$	1839.87	$(37-36s)f$	1840.40
39	$(39-40s)f$	1939.33	$(39-38s)f$	1939.87
41	$(41-42s)f$	2038.80	$(41-40s)f$	2039.33
43	$(43-44s)f$	2138.27	$(43-42s)f$	2138.80
45	$(45-46s)f$	2237.73	$(45-44s)f$	2238.27
47	$(47-48s)f$	2337.20	$(47-46s)f$	2337.73
49	$(49-50s)f$	2436.67	$(49-48s)f$	2437.20
51	$(51-52s)f$	2536.13	$(51-50s)f$	2536.67
53	$(53-54s)f$	2635.60	$(53-52s)f$	2636.13
55	$(55-56s)f$	2735.07	$(55-54s)f$	2735.60
57	$(57-58s)f$	2834.53	$(57-56s)f$	2835.07
59	$(59-60s)f$	2934.00	$(59-58s)f$	2934.53
61	$(61-62s)f$	3033.47	$(61-60s)f$	3034.00

Table D2: Theoretical Stator Current for 70% Load at s = 0.0053

D.2 Axial Vibrations Analysis

The axial vibrations theoretical results for the motor loaded at 65% and 70% are presented in Table D3 and D4 respectively.

Group	Fault Detection Component 1	Frequency (Hz)	Fault Detection Component 2	Frequency (Hz)	Fault Detection Component 3	Frequency (Hz)
1			sf	0.5		
2	$(6-8s)f$	298.1	$(6-6s)f$	298.6	$(6-4s)f$	299.1
3	$(12-14s)f$	596.7	$(12-12s)f$	597.2	$(12-10s)f$	597.7
4	$(18-20s)f$	895.3	$(18-18s)f$	895.8	$(18-16s)f$	896.3
5	$(24-26s)f$	1193.9	$(24-24s)f$	1194.4	$(24-22s)f$	1194.9
6	$(30-32s)f$	1492.5	$(30-30s)f$	1493.0	$(30-28s)f$	1493.5
7	$(36-38s)f$	1791.1	$(36-36s)f$	1791.6	$(36-34s)f$	1792.1
8	$(42-44s)f$	2089.7	$(42-42s)f$	2090.2	$(42-40s)f$	2092.7
9	$(48-50s)f$	2388.3	$(48-48s)f$	2388.8	$(48-46s)f$	2389.3
10	$(54-56s)f$	2686.9	$(54-54s)f$	2687.4	$(54-52s)f$	2687.9

Table D3: Theoretical Axial Vibration at 65% Load with s = 0.0047

Group	Fault Detection Component 1	Frequency (Hz)	Fault Detection Component 2	Frequency (Hz)	Fault Detection Component 3	Frequency (Hz)
1			sf	0.5		
2	$(6-8s)f$	297.9	$(6-6s)f$	298.4	$(6-4s)f$	298.9
3	$(12-14s)f$	596.3	$(12-12s)f$	596.8	$(12-10s)f$	597.3
4	$(18-20s)f$	894.7	$(18-18s)f$	895.2	$(18-16s)f$	895.7
5	$(24-26s)f$	1193.1	$(24-24s)f$	1193.6	$(24-22s)f$	1194.1
6	$(30-32s)f$	1491.5	$(30-30s)f$	1494.0	$(30-28s)f$	1495.5
7	$(36-38s)f$	1789.9	$(36-36s)f$	1790.4	$(36-34s)f$	1790.9
8	$(42-44s)f$	2088.3	$(42-42s)f$	2088.8	$(42-40s)f$	2089.3
9	$(48-50s)f$	2386.7	$(48-48s)f$	2387.2	$(48-46s)f$	2387.7
10	$(54-56s)f$	2685.1	$(54-54s)f$	2685.6	$(54-52s)f$	2686.1

Table D4: Theoretical Axial Vibration at 70% Load with s = 0.0053

APPENDIX E

ADDITIONAL BROKEN ROTOR BAR DETECTION INSTRUMENTS

One of the objectives of this research was to determine which equipment exists for the detection of broken rotor bars. An opportunity was then taken to utilize these equipment for detection of broken rotor bars in order to assess their functionality and utilization for detection of a cracked or broken rotor bar conducted in this research. This section then presents the specifications for the equipment utilised in the research. The equipments were operated and the results analysed by the South African agencies of the OEMs. The full detailed reports submitted are included in APPENDIX F and APPENDIX G.

For the purpose of the better understanding of the discussions in the reports attached in the APPENDIX F and G, the motor with serial number 300068/01 was tested on the 12 September and 10 October is referred to as Motor A or Motor 1 and the motor with serial number 300071/01 tested on the 14 September and 12 October is referred to as Motor B or Motor 1.

E.1 CSMeter

Thomson and Fender [38], after several case studies, developed a portable handheld instrument for reliable on-line detection of broken rotor bars and abnormal levels of eccentricity. The instrument is called CSMeter and is said to detect cracked or broken rotor bars, along with porosity in cast rotors.



Figure E.1: CSMeter [12]

The keyword for condition based-monitoring is reliability and in the case of the instrument this includes a number of critical features:

- Unambiguous diagnosis of a fault over a range of motor ratings.
- Correct estimation of the slip for any given load conditions for a range of motor designs and power ratings.
- Clear discrimination between the unique current signature patterns caused by a fault and any current components induced due to mechanical disturbances to the rotor from gearboxes, belt drivers, and fluid couplings etc in the drive train.
- Reduce the need for an expert to interpret the acquired data by applying reliable, advanced diagnostic algorithms to the current spectra.

The CSMeter is capable of testing all non-synchronous, AC induction motors, and 220 to 13,800 volts. Furthermore, it has the following advantages, which make it better than other equipment:

- Testing is fast and simple and results are provided immediately
- Uses only one current probe
- Can detect broken rotor bars, endring failures, voids/porosity in cast rotors and air gap eccentricity levels.
- Testing is done on-line, in less than two minutes.

- Can accurately test motors under varying load conditions
- Can distinguish between mechanically induced side bands caused by gear reducers, and legitimate rotor bar problems.
- No special training or expertise is needed
- No voltage input required
- No speed input is required

The stator current can be taken by using an industrial CT, which is not sensitive enough to due to burdens across them and saturation problems. The industrial CT must be shorted in its secondary to improve its sensitivity during testing. The measurements are then taken from the shorted output using a current clamp. Then the measured stator current is analysed using CSView. The experiment report for this instrument is included in APPENDIX G.

E.2 CSI 2130 Machine Health Analyser



Figure E.2**:** CSI 2130 Machinery Health Analyser

The CSI 2130 machinery health analyzer (Fig. E.2) is used to collect vibration data, stator current data and flux data in conjunction with the instruments presented below, that is, the current clamp and flux coil. All the data collected from the CSI 2130 machinery health analyzer can be transferred to the AMS suite: Machinery health manager application for final analysis, trending, comparison with results from other diagnostic technologies, decisive problem diagnosis, and implementation of corrective actions. The usage of the CSI 2130 in this research is present in APPENDIX F.

E.3 Current Clamps



Figure E.3: Current Clamps

Lastly, using a current clamp directly clamped around the supply terminals. Data was captured using a CSI2130 and analysed using RBMView.

E.4 Flux Coil



Figure E.4: Flux Coil

Technical Description:

- The CSI Model 343 flux coil is designed for use with CSI machinery analyzers to detect flux generated by electric motors. Except for the initial calibration and possible verification, the use of the 343 flux coil eliminates the need for

current clamp measurements. The flux coil captures flux signals which provide an electrical "quality" signature.

- This electrical signature is sensitive to conditions, which alter the electrical characteristics of the motor, such as broken rotor bars, eccentricity, voltage imbalance between phases, and stator faults.

Flux readings are acquired by consistent placement of the flux coil on the axial outboard end of the motor and automatically stored in the analyzer. Spectra of these measurements may be permanently stored, trended, or analyzed for alarms in CSI MotorView II software.

Benefits:

- Reduces safety concerns by not having to address live power leads.
- On-line non-intrusive motor diagnostic tool.
- Easy to mount on the opposite drive end of motor.
- Eliminates need for current clamp in most cases.
- Detection of electrical faults in ac induction motors.

Flux coil is a simple sensor made of magnetic wire wound into a coil analysed using RBMView.

Even though a measurement may be taken at the same place on motor, if the coil shape is significantly different from one measurement to the next, absolute frequency amplitudes can vary.

Consistent placement of the flux coil on the axial outboard end of the motor is critical for obtaining reliable and trendable data. It is important that the measurement be taken at the same location, with the same spacing between the sensor and motor, and without swinging or twisting movement of the flux coil.

CSI has designed a formed flux coil. It is manufactured in two sizes with diameters of 6" and 12'. The portable coil can be mounted to a motor via magnets or permanently mounted holding pads. A specially designed bracket for holding the flux coil steady will attach to both the magnet and holding pad.

APPENDIX F: CMM CONSULTANTS EXPERIMENT REPORT

CMM Consultants (Pty) Ltd
Condition Monitoring Since 1986

Reg. No. 2004/020845/07

P.O Box 13156
Leraatsfontein,038
Rep. of South Africa
Phone: (013) 697 4693
Fax: (013) 697 4697
www.cmmc.co.za

Report Number: RPN3044

HV Motor – Rotor Bar Tests

Eskom

To enhance our understanding of the plant and to maximise machine availability it is essential that CMM Consultants be informed of any maintenance and or corrective actions performed on the plant monitored.

1: Test Procedure
2: Analysis
3: Conclusion
4: Recommendation

Should you require additional information please feel free to contact us.

Assuring; you of our best attention at all times.

Philip Schutte
Condition Monitoring Management Consultants
082 905 7172

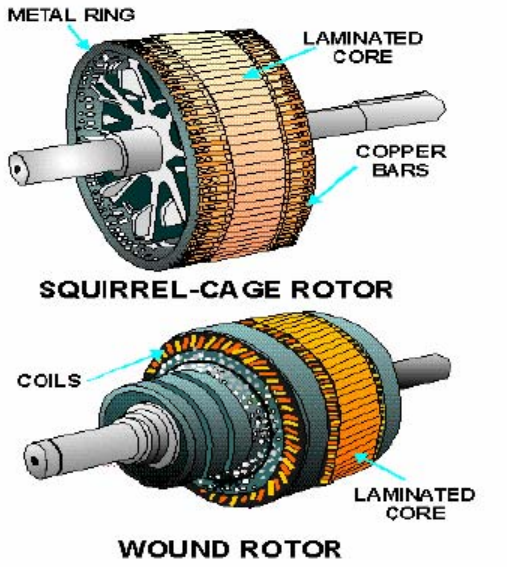
Directors: Reinhardt Otto (Managing) Mike Botes Philip Schutte Debbie Blane (Financial)

1: TEST PROCEDURE

Test Dates:	1st 12 September 2006 (MTR 1) 2nd 14 September 2006 (MTR 2) 3rd 10 October 2006 (MTR 1) 4th 12 October 2006 (MTR 2)
Test Equipment:	CSI 2130 dual channel, data collector in conjunction with a 100-mV/g accelerometer, Current clamp, Flux coil, and Machinery Health Manager (CSI) software was used.
Plot-data:	All vibration data in this report are absolute vibration measured in velocity RMS (mm/sec) and acceleration 0-Peak (G-s). Non-standard data are measured in dB.
Test Procedure:	Our test equipment was installed, both vibration and current/Flux data was taken on both bearings.

Notes: ***RB1 means current clamp***
FCI means flux coil

Diagram



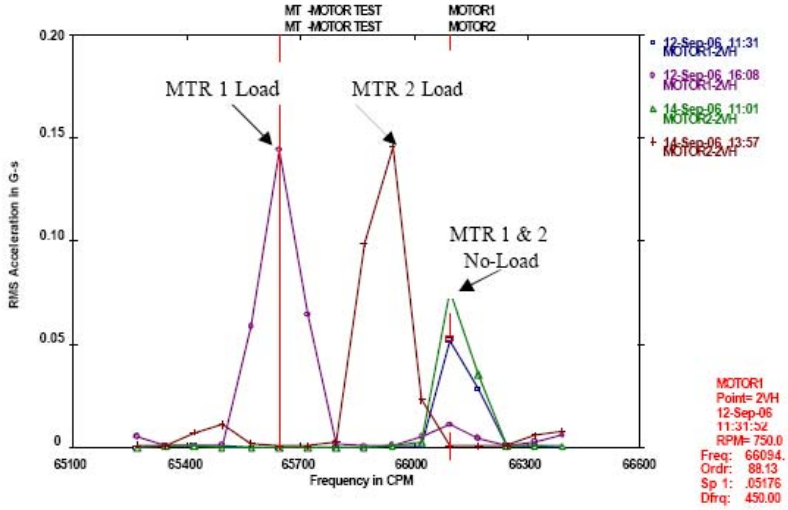
2: ANALYSIS (Test 1and 2)

Motor	**AEI**
Type	**AC Induction Motor**
Phase	**3Ø**
Frequency	**50 HZ**
Voltage	**3300 Volt**
Current	**352Amps**
Speed	**744 RPM**

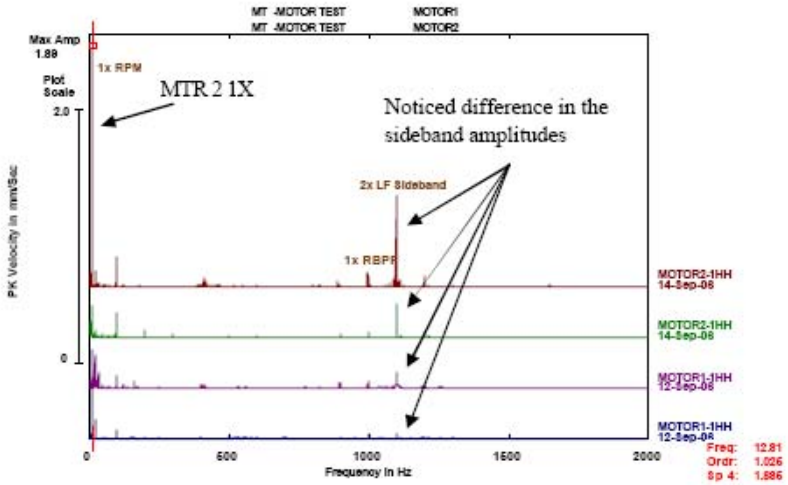
Overall Observation

The overall level of vibration is within acceptable limits, at approximately 70 % of the full-load condition. However there is some concern about the excessive rise in temperature which was recorded on both Motor DE bearings during all tests performed.

Also evident (SEE TREND PLOT BELOW) is that motor 1 had a change in speed of 5.11 RPM in comparison to motor 2 which had an speed change of 1.7 RPM; indicating that motor one (1) was either test at a higher load or that motor one (1) is lest efficient than motor two (2) at the same load, it appear that the later are more correct as both motors where tested at +/- 50 and 94 AMPS. The possibility that the stator was rewind with a different type or diameter wire could not be out-ruled.

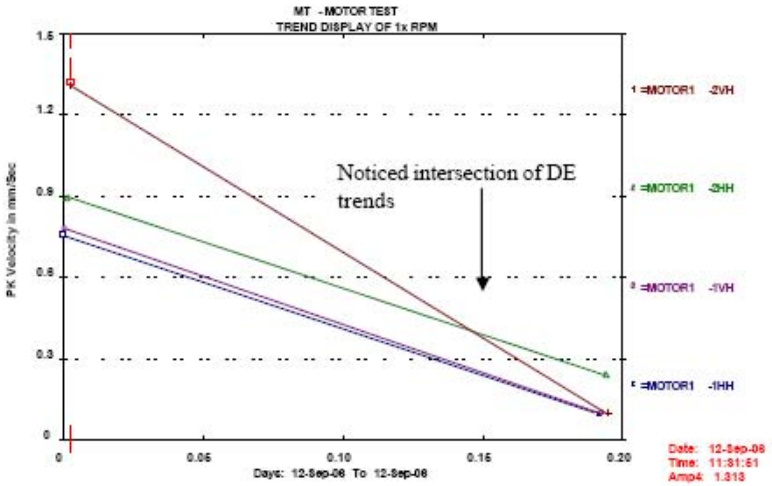


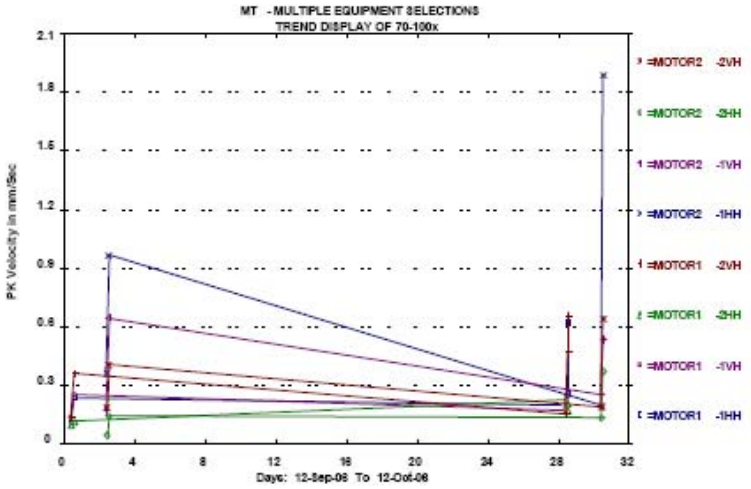
The dynamic balanced condition of both motors are acceptable, however the 1x RPM vibration had increased with approximately 754% (from 0.25 to 1.885 mm/sec) on motor two (2) from no-load to load (SEE MULTIPLE SPECTRUM PLOT BELOW), a similar behaviour of the upper 2x LF sideband around the Rotor bar frequency was noticed, as this phenomenon was not evident on motor MTR 1 we could assume that, thermal bow or an electrical induced, un-balance exist on motor two (2).

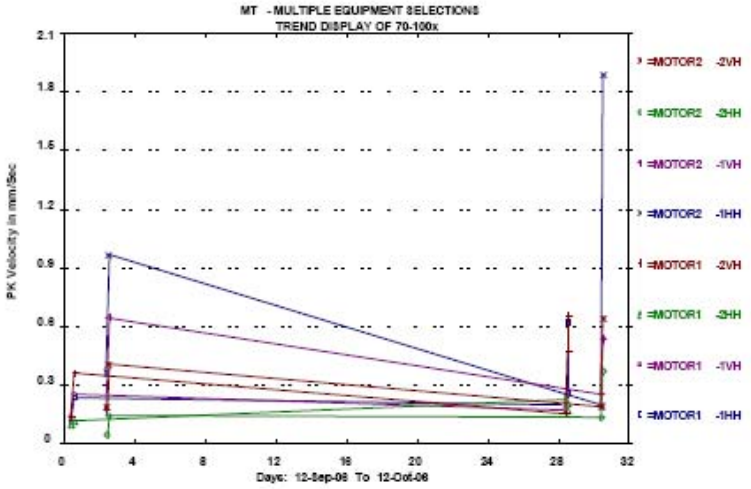


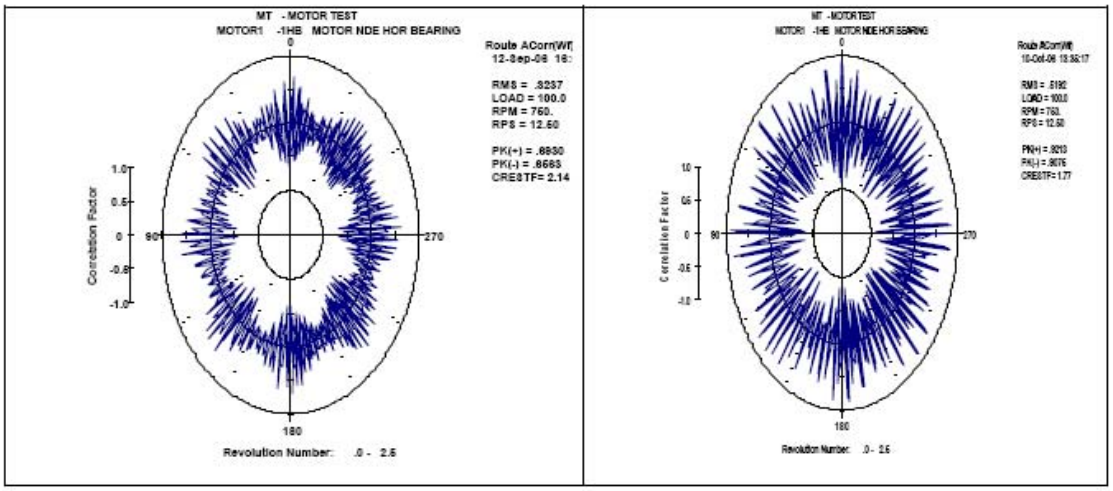
Vibration analysis

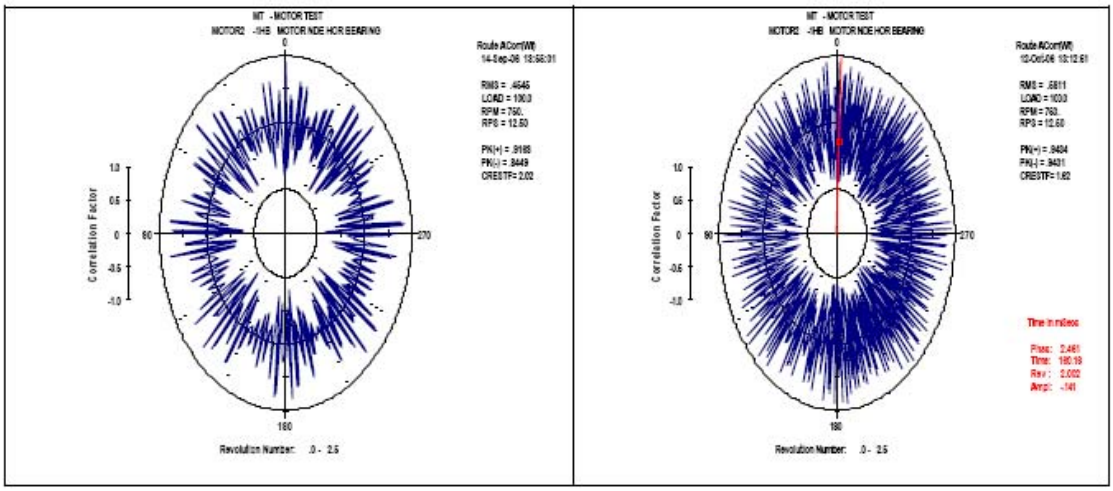
During our initial test on motor one (1) at No-load and load it was clearly evident that the Motor DE bearing might have been damaged or that the bearing clearance is excessive. The reason that, from No-Load to load the vibration amplitude behaviour across the two bearings react completely different within comparison to Motor two (2) (SEE MULTIPLE TREND BELOW).




MT - MULTIPLE EQUIPMENT SELECTIONS
TREND DISPLAY OF 70-100x
PK Velocity in mm/Sec
2.1
1.8
1.5
1.2
0.9
0.6
0.3
0
0
4
8
12
16
20
24
28
32
Days: 12-Sep-08 To 12-Oct-08
=MOTOR2 -2VH
=MOTOR2 -3HH
=MOTOR2 -1VH
=MOTOR2 -1HH
=MOTOR1 -2VH
=MOTOR1 -3HH
=MOTOR1 -1VH
=MOTOR1 -1HH


MT - MULTIPLE EQUIPMENT SELECTIONS
TREND DISPLAY OF 70-100x
PK Velocity in mm/Sec
2.1
1.8
1.5
1.2
0.9
0.6
0.3
0
0
4
8
12
16
20
24
28
32
Days: 12-Sep-08 To 12-Oct-08
=MOTOR2 -2VH
=MOTOR2 -3HH
=MOTOR2 -1VH
=MOTOR2 -1HH
=MOTOR1 -2VH
=MOTOR1 -3HH
=MOTOR1 -1VH
=MOTOR1 -1HH





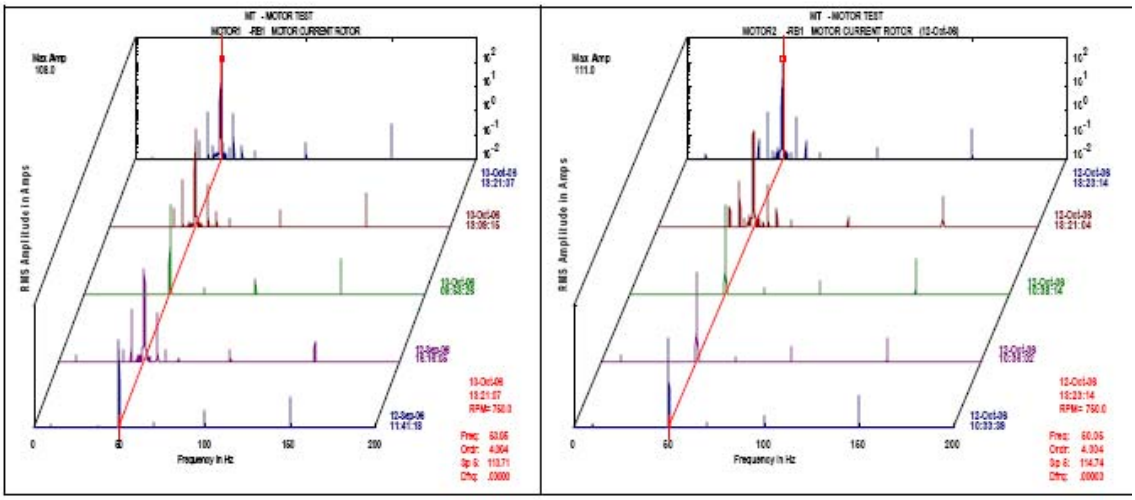
Current Analysis

Brief summing up of our conclusions that have so far been drawn can now be made:

Using the lower and higher sidebands of the stator current of a motor is a valid method for detecting broken bars.

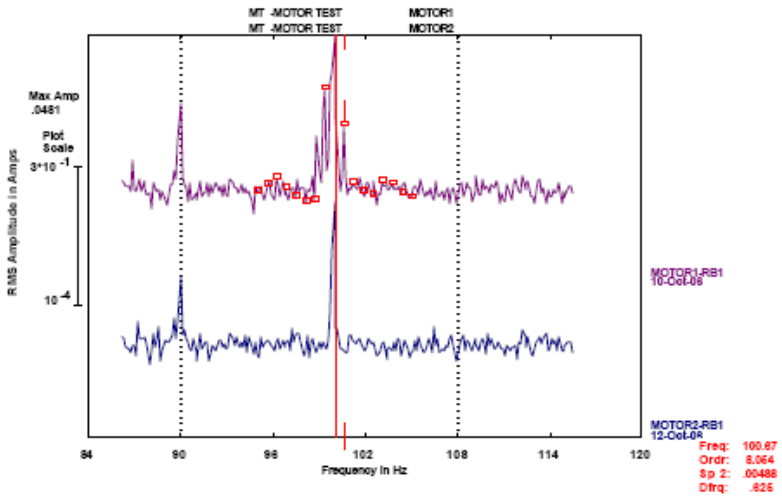
Owing to variation in the amplitude of harmonics with load, and the influence of both the size and the construction characteristics of the motor, the best parameter to indicate the level of breakdown is the difference between the amplitude of the fundamental harmonic and the lower and upper sideband.

Significant changes from No-load to load are evident around Line Frequency (50 Hz) on both motors, however both motors have the same characterises around Line Frequency after the suppose, rotor bar breakage making it difficult to indicate which rotor was damaged (SEE PLOTS BELOW).



However on a closer look at the 2x Line Frequency (100 HZ), its clearly evident that the rotor bar was cut on Motor one (1) (SEE MULTIPLE POINT SPECTRUM PLOT BELOW), the reason are the increase in amplitude of the lower and upper Slip Frequency (37.56 CPM) side band around 2x Line Frequency the ratio in amplitude have decreased to less than 35 dB which indicates the existence of broken bars. This was not evident on the Motor two (2) or on Motor one (1) before the suppose rotor bar breakage.

We have to point out that, when pulsating loads are applied to an induction motor, oscillations in the speed bring about changes in the motor's magnetic field, and in consequence in the stator current In fact, running machines such as compressors, pumps and especially gearboxes makes diagnosis of the rotor condition using current spectrum enormously difficult. From this point of view, it might be thought tat any external factor that causes regular fluctuations in the rotation speed of a rotor, or its torque to put in another way, might cause harmonics to occur in the supply current.



Flux Analysis

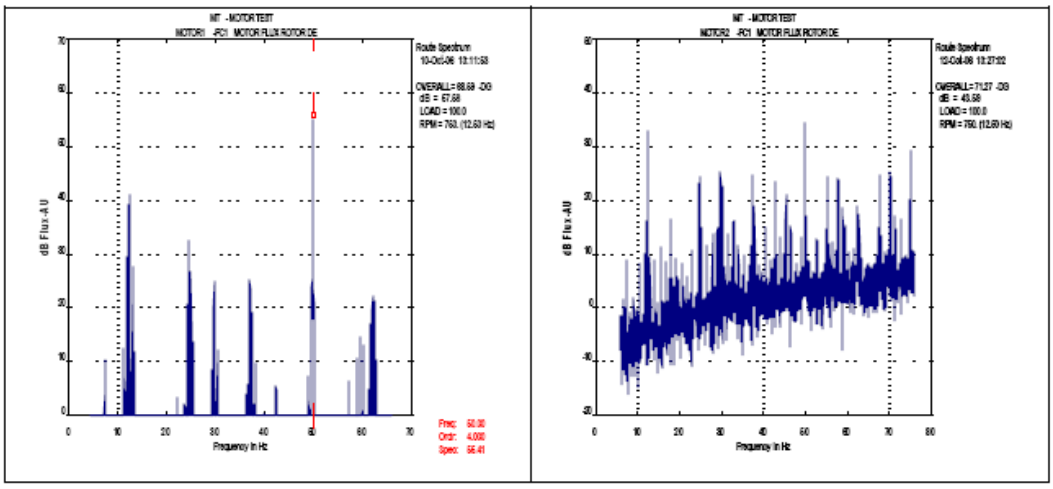
Axial leakage flux, which is also called shat flux, appears in all electrical machines and is produced because no machine can be constructed perfectly symmetrical. There will always be slight asymmetries in the electric and magnetic circuits due to building tolerances, anisotropy of the materials and so on.

The frequencies that vary in the flux spectrum when rotor symmetries are applied correspond to harmonics that already occur in the axial flux of the machine; in order words, new frequencies do not occur when the rotor is broken. This leads one to think that the breakdown mechanism is similar to the one described for stator currents, where the harmonic caused by the fault, which have identical frequencies to those already in the motor, are superimposed on them.

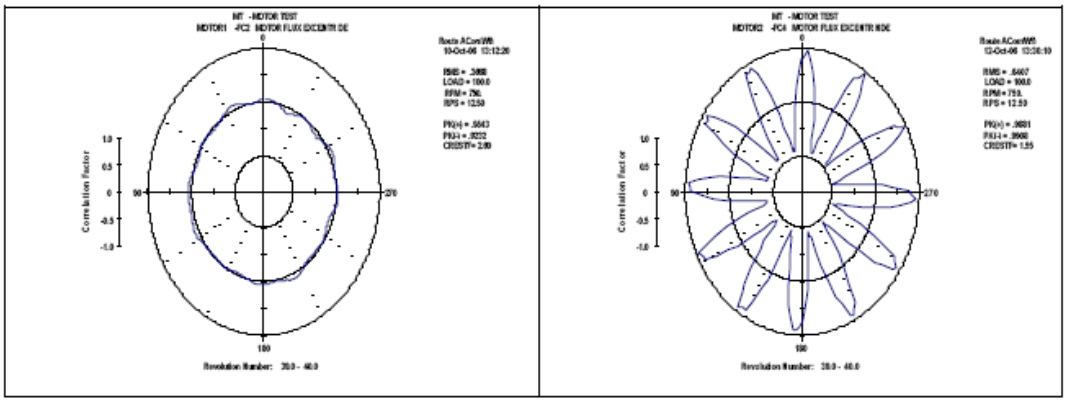
These harmonics are grouped more or less equidistant to each other, and when the motor is tested at different loads they are displaced, which points to their dependency on the motor's ration speed, or, in other words, its slip.

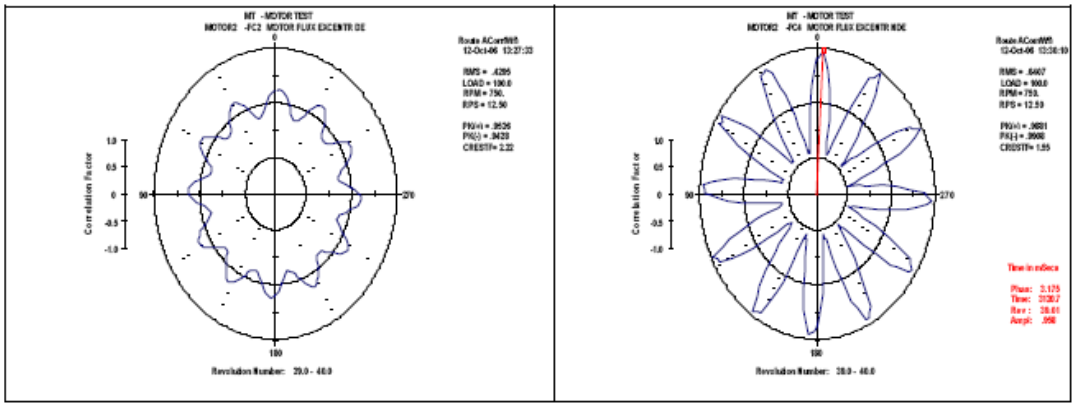
As axial flux is generated from stator and rotor currents, one might assume that the fault frequencies characteristic of the flux will be similar to those of the currents.

The significant difference in the flux data captured at load and before the supposed rotor brakeage indicates, that the rotor bar brakeage occurred on motor one (1). The excessive raised noise floor on motor two (2) also indicates that the Motor DE bearing was damaged during assembling of the Motor. However it's my opinion that the air gap on motor two (2) had changed after reassembling and therefore changing the characteristic and the behaviour of the motor, this could also explained the high bearing temperature of the DE Bearing.

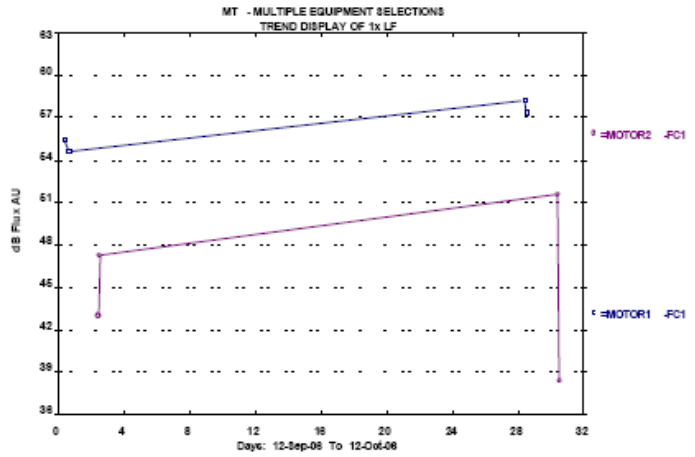


No significant difference is evident between motor 1 and 2 when comparing the auto correlation plots; I also suspect that the unique pattern is related to the stator configuration, and that the significant difference between the DE and NDE indicated that some form of eccentricity exist on both motors due to a, uneven air gap on the motor DE side (SEE FLUX AUTO CORRELATION PLOTS BELOW).

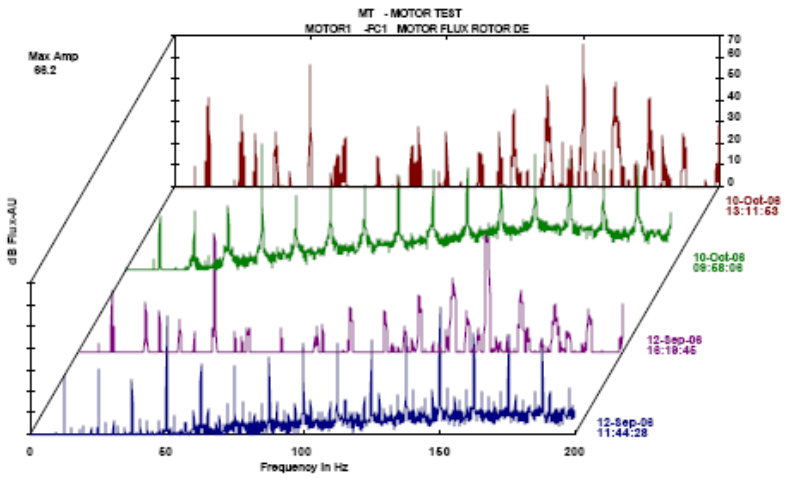




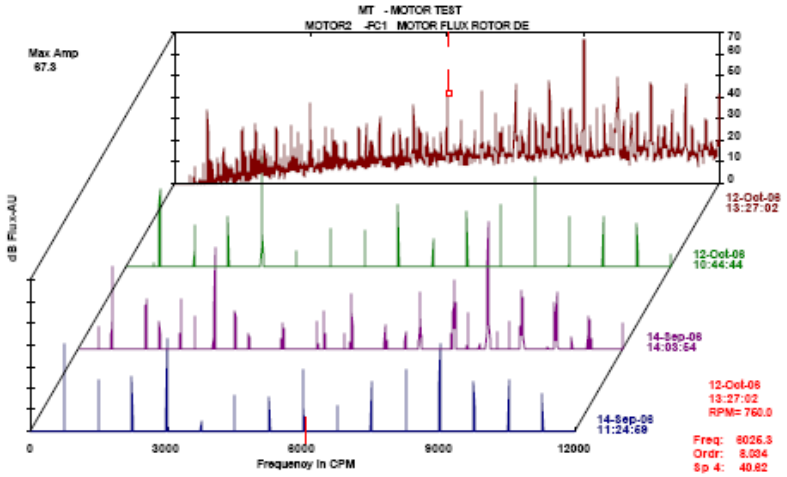
PLOT COMPARISON OF LINE FREQUECY MOTOR 1 AND 2



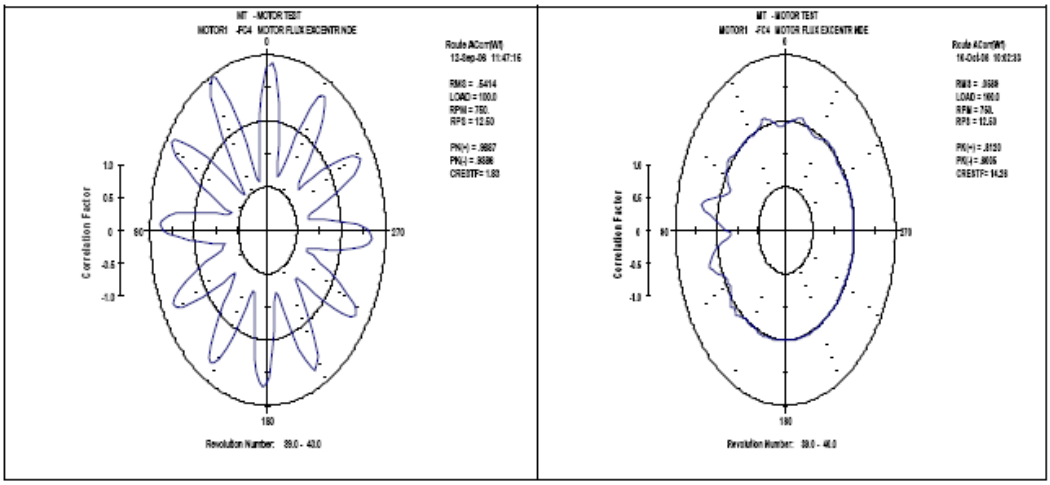
PLOT COMPARISON OF FLUX DATA MOTOR 1

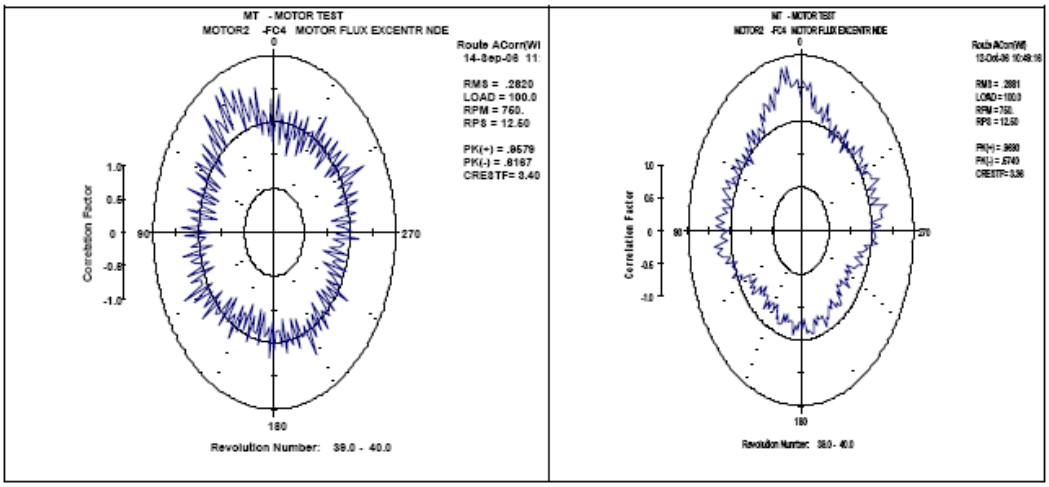


PLOT COMPARISON OF FLUX DATA MOTOR 2



PLOT COMPARISON OF FLUX ECCENTRICITY MOTOR NDE 1 AND 2





APPENDIX G: IRIS POWER EXPERIMENT REPORT

IRIS POWER L.P.

Current Signature Analysis Report

ESKOM
Motors Arnot M&C and
Arnot M&C B

Client Reference No:	*N/A*
IRIS Reference No:	N/A
Issue No:	1
Revision No:	1
Date:	Nov 1, 2006
Issuing office	*Toronto*

Prepared by: **Hasnain Jivajee**
Signature: 
Date: **01-Nov-2006**

Reviewed by: **Ian Culbert**
Signature: 
Date: **02-Nov-2006**

This document has been prepared for the titled project and should not be relied upon or used for any other project without an independent check being carried out as to its suitability and prior written authority of IRIS Power Engineering being obtained. IRIS accepts no responsibility or liability for the consequences of this document being used for a purpose other than the purposes for which it was commissioned. Any person using or relying on the document for such other purposes agrees, and will by such use or reliance be taken to confirm his agreement to indemnify IRIS for all loss or damage resulting therefrom. IRIS accepts no responsibility or liability for this document to any party other than the person by whom it was commissioned.

Disclaimer: It is impossible to predict time to failure.

Table of Contents

1 INTRODUCTION 3
2 SQUIRREL-CAGE ROTOR FAILURE MECHANISMS 3
3 BROKEN ROTOR CAGE WINDING DETECTION VIA MCSA 3
4 AIRGAP ECCENTRICITY (AGE) 5
5 MOTOR ARNOT M&C 6
5.1 Motor Design 6
5.2 MCSA Results 6
5.3 Discussion of Results 7
6 MOTOR ARNOT M&C B 8
6.1 Motor Design 8
6.2 MCSA Results 8
6.3 Discussion of Results 9
7 CONCLUSIONS AND RECOMMENDATIONS 10
7.1 Motor Arnot M&C 10
7.2 Motor Arnot M&C B 10
8 REFERENCES 10

APPENDIX – Broken Bar & Air Gap Eccentricity Reports

1 INTRODUCTION

The IRIS Power L.P. CSMeter is designed to detect defects in squirrel cage rotor windings and the degree of eccentricity in the airgap between the stator bore and rotor outside diameter.

2 SQUIRREL-CAGE ROTOR FAILURE MECHANISMS

For fabricated rotor windings, which the motors covered by this report almost certainly have, bar or short-circuit ring failures can occur from poor design, poor manufacture or frequent starting, especially if the driven equipment has a high inertia. Once one bar breaks additional mechanical and thermal stresses are placed on adjacent bars and they will also eventually fail to increase the number of broken bars. If this goes undetected a bar end, or piece of bar may eventually strike the stator winding and cause it to fail to ground. Broken short-circuit rings may also lead to consequential stator winding failures.

Other symptoms of motors with broken cage windings are a magnetic noise during starting and high vibration levels at rotor slot passing frequency with sidebands ± 2x line frequency removed and 2 x slip frequency variations in motor current.

3 BROKEN ROTOR CAGE WINDING DETECTION VIA MCSA

3.1 Current Signature for Cage Winding Breaks

It is well known that by identifying specific signatures in the stator current of an induction motor, breaks or cracks in rotor bars and shorting rings may be identified. It can be shown, from first principles that, if rotor cage winding breaks (hereafter referred to as BB) are present this gives rise to two current components distributed symmetrically around the main supply frequency component f_1. These current components are referred to as BB sidebands. It is well beyond the scope of this report to derive the equations for detection of the broken rotor bar current signature but an appraisal of the theory is given below [2].

Rotor currents in a cage winding produce a 3-phase magnetic field with the same number of poles as the stator field, but rotating at slip frequency $f_2 = s \times f_1$, where f_1 is the main supply frequency, with respect to the rotating rotor. In a symmetrical cage winding, only a forward rotating field exists. If rotor asymmetry occurs there will also be a resultant backward rotating field at slip frequency with respect to the forward rotating rotor. It can be shown that the backward rotating field with respect to the rotor induces an e.m.f. and current in the stator winding at:

$$F_{lsb} = f_1(1-2s) \text{ Hz} \qquad (1)$$

where s is the operating slip. This is referred to as the lower twice slip frequency sideband due to BB. There is therefore a cyclic variation of current that causes a torque pulsation at twice slip frequency ($2sf_1$) and a corresponding speed oscillation, which is also a function of

the drive inertia. Due to this rotor oscillation, an upper sideband current component is also induced in the stator and is enhanced by the third time harmonic flux. BB therefore result in current components being induced in the stator winding at frequencies given by:

$$f_{sb} = f_1(1 \pm 2s)\ \text{Hz} \qquad (2)$$

These are the classical twice slip frequency sidebands due to BB. An example of the current signature for an induction motor subjected to BB is given in Figure 1. Here, two side bands symmetrically distributed around the main supply frequency can clearly be seen.

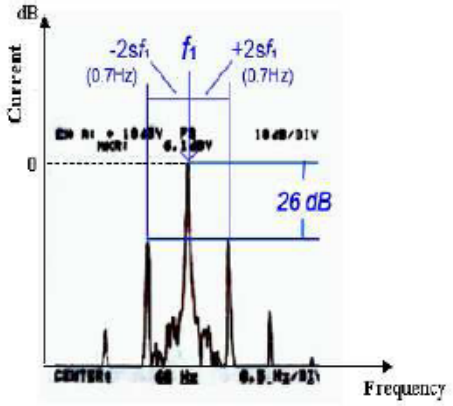


Figure 1: Example of a broken rotor bar spectrum containing clear evidence of broken rotor bars.

Thus, via frequency analysis of the motor supply current, by knowing the operating slip, current components due to the presence of BB may be detected The operating slip may be derived from the operating speed and, consequently, may be evaluated via a tachometer or a stroboscope measurement of the shaft speed.

The operating speed may also be deduced from the frequency spectrum itself. Using sophisticated algorithms, CSMeter is able to reliably estimate the operating slip for a wide range of induction motors providing the motor nameplate data is accurate.

If the number of rotor bars are known then the CSMeter provides an estimate of the number of broken bars based on the formula;

$$N \approx \frac{2R}{10^{d/20} + p} \qquad (3)$$

Where,

N = the estimated number of broken bars
R = the number of rotor slots
d = the average dB difference between the BB sidebands and the fundamental 60 Hz component of current
p = the number of pole pairs

3.2 Current Signature for Number of Rotor Spider Arms Equal to Number of Poles

A motor design feature that can lead to a false positive indication of a BB is if the number of spider arms (flutes) on the rotor shaft, to support the core, is equal to or is a multiple of the number of motor stator winding poles [1] . With this arrangement twice slip frequency

modulation of the motor magnetizing current and therefore airgap flux occurs to create current sidebands with the same frequency as those produced by BB. The only way to differentiate between the two is to perform tests at two significantly different loads. One of these loads should be at around the motor nameplate rating or as close to this as possible and the other should be about 20% less. If the $2Sf_1$ sidebands are due to BB then the magnitudes of both will reduced with load. On the other hand, if the sidebands are due to the number of rotor spider arms being equal to or a multiple of the number of poles, then their magnitudes will remain essentially the same no matter what the motor load is.

3.3 Two-Test Comparison

If there is any doubt as to whether symmetrical current components around the fundamental 60 Hz (f_1) current are due to broken bars or rotor spider arms a comparison of the results of two tests one of which should be at around motor full load and another at a load that is at least 20% less should, if possible be performed. If, as shown in Figure 2, the current components $\pm 2sf_{1HL}$ at the higher load are significantly further removed from the f_1 fundamental current component than the $\pm 2sf_{1LL}$ lower load ones then this confirms that they are due to BB or that number of rotor flutes is equal to or is a multiple of the number of poles. On the other had if the frequencies of these $\pm 2sf_1$- sidebands change very little with load they are due to some mechanical influence that could relate to the compressor the motor is driving.

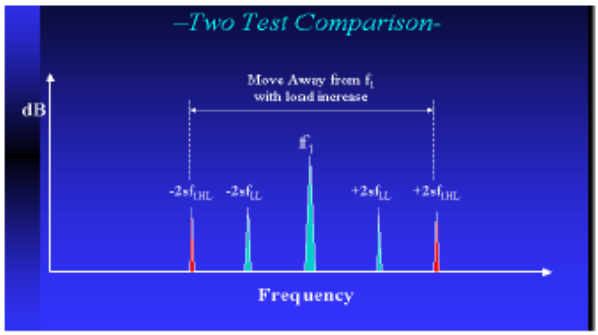


Figure 2

4 AIRGAP ECCENTRICITY (AGE)

4.1 Causes of Airgap Eccentricity

The industry standard for airgaps between the stator bore and rotor outside diameter is that they should be within ± 10% of the average of measurements taken 4 positions 90° apart. If this value is exceeded the unbalanced magnetic pull force between the rotor and stator will be high enough to create increased vibration levels, at 2X power supply frequency. This leads to increased bearing wear and in extreme cases the rotor pulling over to rub on the stator bore if the shaft stiffness is not high enough. The major causes of such problems are poor design, manufacturing defects and improper motor assembly. It is also important to note that if the

static airgaps approach 10% eccentricity then unbalanced magnetic pull can create dynamic eccentricity levels that cause the AGE to exceed ± 10%. In fact it is fair to say that unless the airgaps are perfect there will always be a component of dynamic eccentricity between the motor stator and rotor.

4.2 Current Signature for Airgap Eccentricity

Air gap eccentricity may be determined by identifying and analyzing the characteristic current signature pattern indicative of non-uniform stator bore to rotor outside diameter clearances [3]. The specific frequencies of the current components indicative of air gap eccentricity may be calculated by:

$$f_{ec} = f_1[R(1-S)/p \pm n_{ws}] \pm f_1[(1-S)/p] \quad (3)$$

f_{ec} = frequency components which are a function of airgap eccentricity
f_1 = supply frequency
R = number of rotor slots
$n_d = \pm 1$
s = slip
p = pole-pairs
n_{ws} = 1, 3, 5, 7……etc

This equates to a series of slot passing frequency components that are twice power supply frequency apart and have sidebands that are ± rotational speed frequency (f_r) removed. To assess motor airgap eccentricity from this spectrum the slot passing frequency component with the highest magnitude is selected. The average magnitude difference between the ± f_r components (in dB) relative that of the slot passing frequency are then determined. Average magnitude differences ≥ 35dB indicate acceptable airgaps and the motor would not likely exhibit excessive vibration levels.

5 MOTOR ARNOT M&C

5.1 Motor Design

Voltage	*6600V*	RPM/# Poles	*740/8*
HP	*3300*	Insulation	*Epoxy-mica*
Full Load Current	*352 A*	Manufacturer	*Westinghouse*
Machine type	*Induction Motor*	Rotor Slots	*80*
# Rotor Spider Arms	*Not known*	No-Load Current	*93.9 A*

5.2 MCSA Results

Current signature analysis (CSA) data was obtained on motor Arnot M&C on October 10, 2006. A measure of the operating current was provided by connecting to the secondary side of the main CT using a 5A/1V current probe from Northern Design Ltd. Several sets of

consequential BB and AGE tests were performed using an IRIS Power L.P. CSMeter. From one of these tests (ID #121) the following motor performance parameters were determined from the CSMeter:

Load Current – 223.55 A Operating Frequency – 50.02 Hz

5.3 Discussion of Results

5.3.1 BB Analysis

Figure 3 shows components that are present in the BB area of the current spectrum with two sidebands symmetrically distributed around the operating frequency at approximately ± 0.43Hz, marked as 'a' in Figure 3. The magnitude of the lower sideband is –51.2dB and that of the upper sideband is –48.5dB, yielding an average magnitude of –49.85dB.

Since the number of rotor bars is known, we use Equation 3 to estimate the number of broken bars which yields 0.51 broken bars. Equation 3, however, would only be accurate if the test was done at full load. In order to compensate for reduced load a correction factor of 2 is applied to the result. Re-calculation of Equation 3 with the correction factor yields an estimated 1.02 broken bars. The derivation of the correction factor is proprietary.

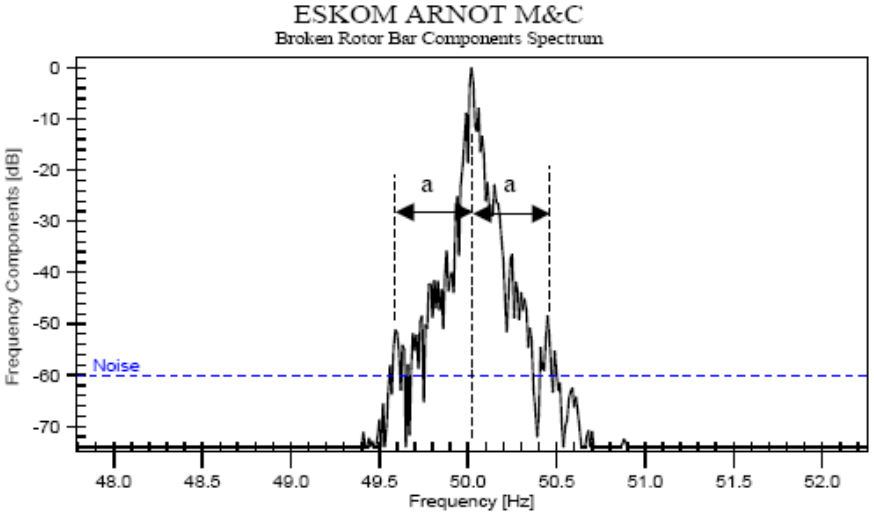


Figure 3

Since the sidebands are located at ±0.43 Hz from the operating frequency, Equation 1 yields an operating slip of 0.004298. Extrapolating the load vs slip curve to full load, starting from a no-load current of 93.9A, yields a full-load slip of 0.00856. This is equivalent to a full-load speed of 743.6 rpm, which does not compare well with the nameplate rated speed of 740 rpm. We believe the rated nameplate speed may be obsolete or inaccurate for this motor, keeping in mind its vintage (circa 1955) and the fact that repair work may have changed the nameplate parameters somewhat.

It may be worthwhile to mention that CSMeter relies heavily on the accuracy of rated nameplate speed and current. If these parameters are inaccurate there could be a risk of misdiagnosis. In this case we feel that the CSMeter was not able to detect broken rotor bars due to the inaccuracy of rated nameplate speed since the sidebands fell just outside of the calculated broken bar domain. Thus the manual calculations shown above were necessary to arrive at a diagnosis.

5.3.2 AGE Analysis

From Figure 4 (graph from test ID #122) the average difference, in dB, between RSPFC and the ± RSFC components = (51.48 + 56.31)/2 – 7.71 = 46.18 dB which indicates that the motor is running within the normal ± 10% limit for AGE.

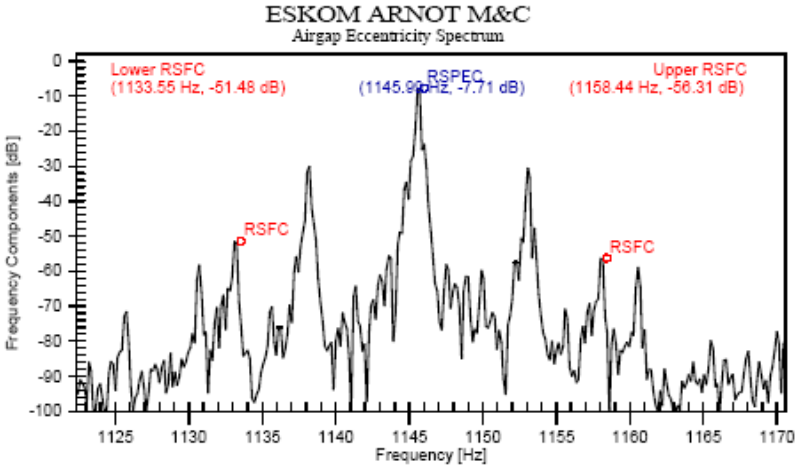


Figure 4

6 MOTOR ARNOT M&C B

6.1 Motor Design

Voltage	*6600V*	RPM/# Poles	*740/8*
HP	*3300*	Insulation	*Epoxy-mica*
Full Load Current	*352 A*	Manufacturer	*Westinghouse*
Machine type	*Induction Motor*	Rotor Slots	*80*
# Rotor Spider Arms	*Not known*	No-Load Current	*93.9 A*

6.2 MCSA Results

Current signature analysis (CSA) data was obtained on motor Arnot M&C B on October 12, 2006. A measure of the operating current was provided by connecting to the secondary side of the main CT using a 5A/1V current probe from Northern Design Ltd. Several sets of consequential BB and AGE tests were performed using an IRIS Power L.P. CSMeter. From

one of these tests (ID #137) the following motor performance parameters were determined from the CSMeter:
Load Current – 227.12 A Operating Frequency – 50.03 Hz

6.3 Discussion of Results

6.3.1 BB Analysis

From Figure 5 there are no signs of frequency components in the broken rotor bar domain.

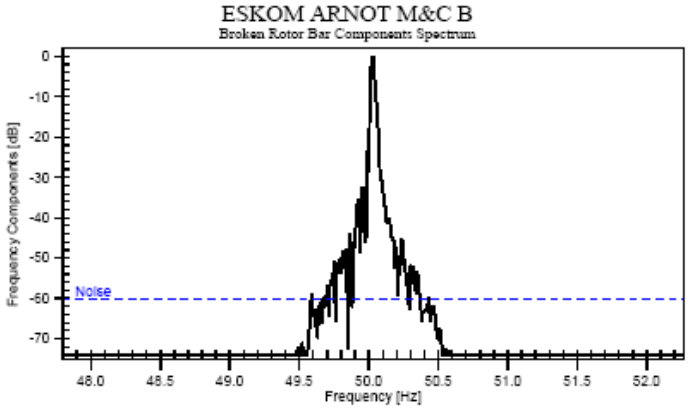


Figure 5

6.3.2 AGE Analysis

From Figure 6 (graph from test ID #133) the average difference, in dB, between RSPFC and the ± RSFC components = (52.06 + 54.01)/2 – 11.22 = 41.81 dB which indicates that the motor is running within the normal ± 10% limit.

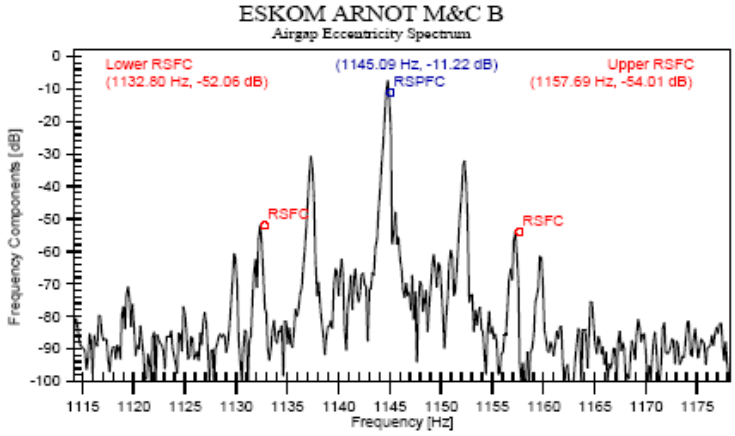


Figure 6

7 CONCLUSIONS AND RECOMMENDATIONS

7.1 Motor Arnot M&C

- From manual calculations and analysis it appears that this motor has approximately 1 broken rotor bar. A bi-annual test is recommended to develop a trend.
- At the next opportunity a two-test-comparison should be done to confirm the presence of broken bars. This requires two tests to be performed at significantly different loads.
- Air gap eccentricity for this motor appears to be within the 10% tolerance normally set by manufacturers.
- Keeping in mind the uncertainty about the accuracy of the motor nameplate speed it may be advisable to perform additional tests using a strobe light to measure the actual rotor speed and inputting this to the CSMeter. Please refer to Section 4.1.3 of CSMeter User Manual.

7.2 Motor Arnot M&C B

- There is no evidence to indicate the presence of either broken rotor bars or abnormal air gap eccentricity.

8 REFERENCES

1) CSMeter: CSView User Manual Version 1, February 2004.
2) Ian Culbert & Wendell Rhodes - Using Current Signature Analysis Technology to Reliably Detect Cage Winding Defects in Squirrel Cage Induction Motors: IEEE 2005 PCIC, Denver Colorado.
3) Ian Culbert, Hasnain Jivajee – New Current Signature Analysis Technology to Reliably Detect Cage winding Defects and Abnormal Airgap Eccentricity in Induction Motors, EXFOR 2005, Montreal, Canada.

APPENDIX

CSView 3.2, printed: Thursday, November 2, 2006

Broken Rotor Bars - Spectral Analysis

Motor Description:

Motor:	ESKOM ARNOT MC
Company:	Westward
Serial Number:	300068 01
Manufacturer:	AEI
Motor Type:	Induction Motor
Stator Type:	Form Wound
Year of Inst.:	1977
Stator Insulation:	Epoxy Mica
Frequency:	50.00 Hz
Rated Power:	2300.00 hp
Power Factor:	-
Rated Voltage:	3300.00 V
Rated Current:	352.00 A
No Load Current:	93.90 A
Rated Speed:	740.00 rpm
Rotor Slots:	80

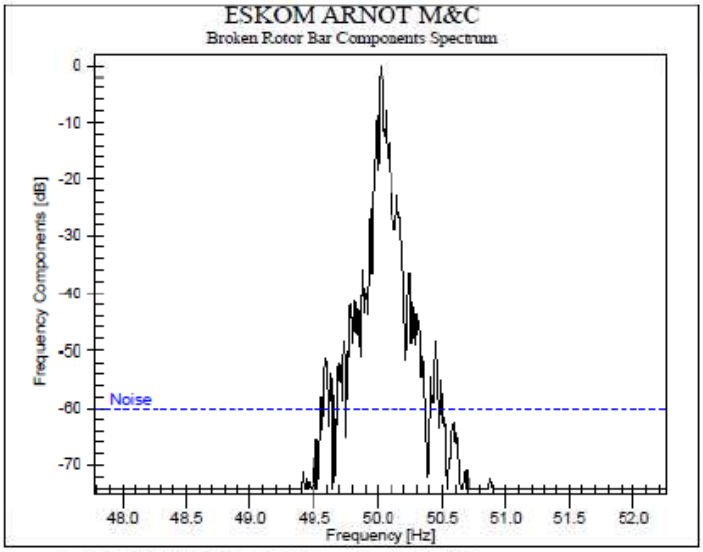
Mechanical Drive Components:
None

Diagnostic Summary:

Result:	BBE -
Lower Sideband:	
1st Peak Detected:	-
2nd Peak Detected:	
Upper Sideband:	
1st Peak Detected:	-55.30 dB at 50.49 Hz
2nd Peak Detected:	-

Measurement Conditions:

Measurement ID:	#121
Operating Slip:	
Operating Frequency:	50.02 Hz
Operating Speed:	
Reference Current:	223.55 Amps
Frequency Resolution:	10 mHz
Probe Name:	5A
Probe Type:	Passive Probe
Probe Ratio:	5.000
Amplifier/Attenuator Gain:	2.711
Noise Level:	0.00 dB
Main CT Ratio:	60.00



Data acquired Tue Oct 10 13:16:26 2006, by CSMeter serial number: 0440805

CSView 3.2, printed: Thursday, November 2, 2006

Airgap Eccentricity - Spectral Analysis

Motor Description:

Motor:	ESKOM ARNOT MC
Company:	Westward
Serial Number:	300068-01
Manufacturer:	AEI
Motor Type:	Induction Motor
Stator Type:	Form Wound
Year of Inst.:	1977
Stator Insulation:	Epoxy Mica
Frequency:	50.00 Hz
Rated Power:	2300.00 hp
Power Factor:	-
Rated Voltage:	3300.00 V
Rated Current:	352.00 A
No Load Current:	93.90 A
Rated Speed:	740.00 rpm
Rotor Slots:	80

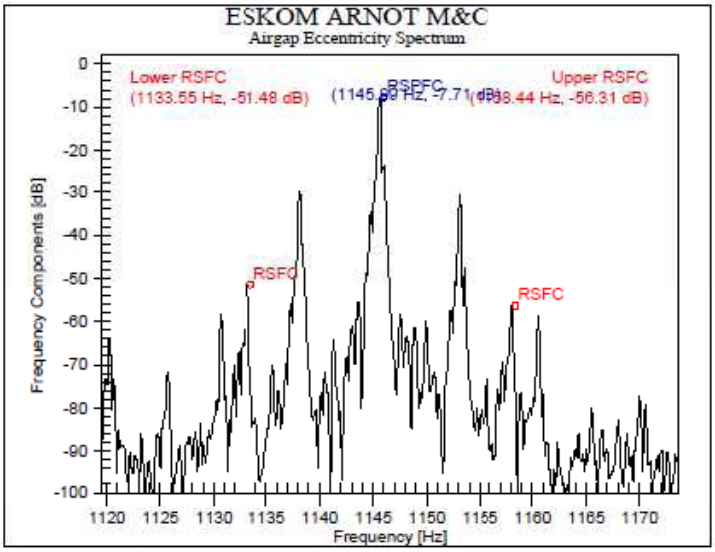
Mechanical Drive Components:
None

Diagnostic Summary:

Result:	Well within tolerance
Peak RSPFC:	-7.71 dB at 1145.99 Hz
Lower RSFC:	-51.48 dB at 1133.55 Hz
Upper RSFC:	-56.31 dB at 1158.44 Hz

Measurement Conditions:

Measurement ID:	#122
Operating Slip:	0.004
Operating Frequency:	50.02 Hz
Operating Speed:	746.8 rpm
Reference Current:	223.55 Amps
Frequency Resolution:	150 mHz
Probe Name:	Probe 5.00 x
Probe Type:	Passive Probe
Probe Ratio:	5.000
Amplifier/Attenuator Gain:	0.980
Noise Level:	0.00 dB
Main CT Ratio:	60.00



Data acquired Tue Oct 10 13:16:13 2006, by CSMeter serial number: 0440805

CSView 3.2, printed: Thursday, November 2, 2006

Broken Rotor Bars - Spectral Analysis

Motor Description:

Motor:	ESKOM ARNOT M&C B
Company:	Westward
Serial Number:	399971-01
Manufacturer:	AEI
Motor Type:	Induction Motor
Stator Type:	Form Wound
Year of Inst.:	1977
Stator Insulation:	Epoxy Mica
Frequency:	50.00 Hz
Rated Power:	2300.00 hp
Power Factor:	-
Rated Voltage:	3300.00 V
Rated Current:	352.00 A
No Load Current:	93.90 A
Rated Speed:	740.00 rpm
Rotor Slots:	80

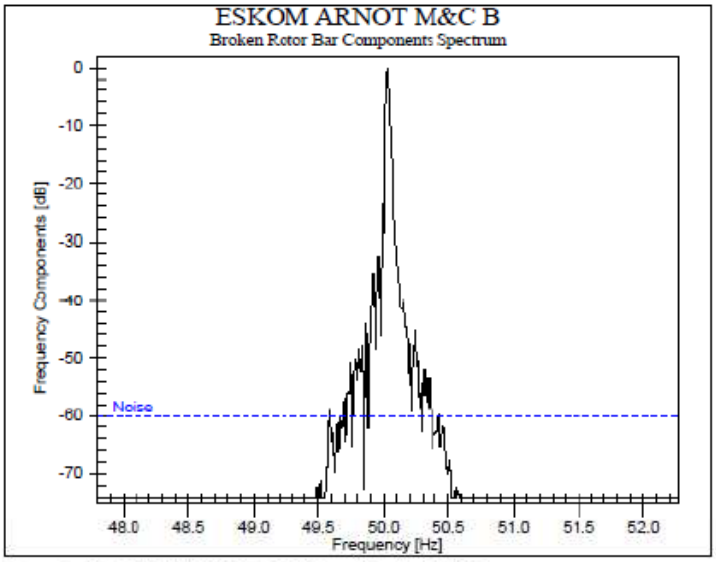
Mechanical Drive Components:
None

Diagnostic Summary:

Result:	BBE -
Lower Sideband:	
1st Peak Detected:	-
2nd Peak Detected:	
Upper Sideband:	
1st Peak Detected:	-
2nd Peak Detected:	-

Measurement Conditions:

Measurement ID:	#137
Operating Slip:	
Operating Frequency:	50.03 Hz
Operating Speed:	
Reference Current:	237.12 Amps
Frequency Resolution:	10 mHz
Probe Name:	5A
Probe Type:	Passive Probe
Probe Ratio:	5.000
Amplifier/Attenuator Gain:	2.711
Noise Level:	0.00 dB
Main CT Ratio:	60.00



Data acquired Thu Oct 12 13:17:22 2006, by CSMeter serial number: 0440805

IRIS Power Engineering, Inc. 1 Westside Drive, Unit 2, Etobicoke, Ontario, M9C 1B2, CANADA
Telephone: +1 (416)-620-5600 Fax: +1 (416)-620-1995 Web: www.irispower.com

CSView 3.2, printed: Thursday, November 2, 2006

Airgap Eccentricity - Spectral Analysis

Motor Description:

Motor:	ESKOM ARNOT MC B
Company:	Westward
Serial Number:	300071-01
Manufacturer:	AEI
Motor Type:	Induction Motor
Stator Type:	Form Wound
Year of Inst.:	1977
Stator Insulation:	Epoxy Mica
Frequency:	50.00 Hz
Rated Power:	2300.00 hp
Power Factor:	-
Rated Voltage:	3300.00 V
Rated Current:	352.00 A
No Load Current:	93.90 A
Rated Speed:	740.00 rpm
Rotor Slots:	80

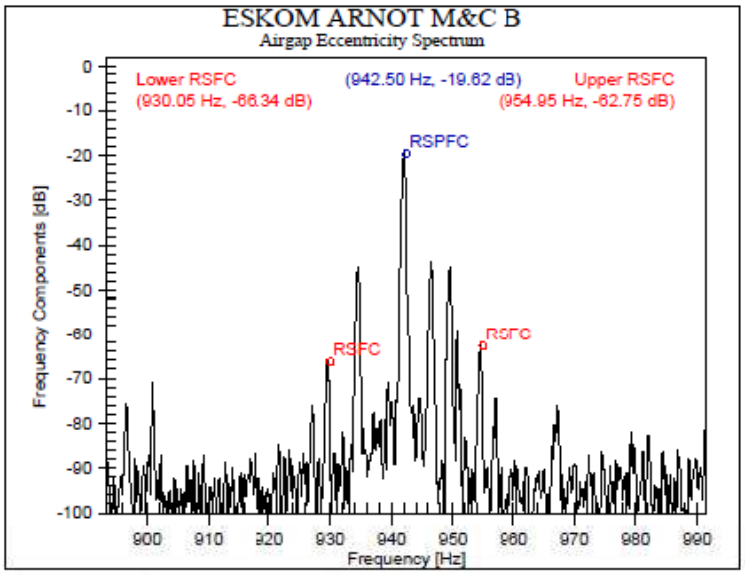
Mechanical Drive Components:
None

Diagnostic Summary:

Result:	Well within tolerance
Peak RSPFC:	-19.62 dB at 942.50 Hz
Lower RSFC:	-66.34 dB at 930.05 Hz
Upper RSFC:	-62.75 dB at 954.95 Hz

Measurement Conditions:

Measurement ID:	#135
Operating Slip:	0.009
Operating Frequency:	50.07 Hz
Operating Speed:	743.4 rpm
Reference Current:	490.13 Amps
Frequency Resolution:	150 mHz
Probe Name:	5A
Probe Type:	Passive Probe
Probe Ratio:	5.000
Amplifier/Attenuator Gain:	0.980
Noise Level:	0.00 dB
Main CT Ratio:	60.00



Data acquired Thu Oct 12 13:10:40 2006, by CSMeter serial number: 0440805

IRIS Power Engineering, Inc. 1 Westside Drive, Unit 2, Etobicoke, Ontario, M9C 1B2, CANADA
Telephone: +1 (416)-620-5600 Fax: +1 (416)-620-1995 Web: www.irispower.com

REFERENCES

[1] Ahmed M. and Henderson R., 'Medium Voltage Motor Reliability and Performance Enhancement', Eskom Resources and Strategy Research Division, Research Proposal.

[2] Ansoft RMxprt: AP0679911, 'A Three-phase Induction Motor Problem'. INTERNET: www.ansoft.com/devices/motor/3phase10.pdf, - Application Note, Cited December 2006.

[3] Bellini A., Filipetti F., Franceschini G., Tassoni C., and Kliman G.B., 'Quantitative Evaluation of Induction Motor Broken Bars by Means of Electrical Signature Analysis', IEEE Transaction on Industrial Applications, vol. 37, no 5 pp 1258-1255, 2001.

[4] Benbouzid Mohamed El Hachemi, 'A Review of Induction Motors Signature Analysis as a Medium for Faults Detection', IEEE Trans. on Ind. Electronics, Vol. 47, No. 5 October 2000.

[5] Benbouzid M.E.H., Kliman G.B., 'What stator current processing based technique to use for induction motor rotor faults diagnosis?' IEEE Power Engineering Review, August 2002.

[6] Bowers S.W., Piety K.R., and Piety R.W. and Colsher Richard J., 'Evaluation of the Field Application of Motor Current Analysis', INTERNET: http://www.compsys.com/ - Application Papers, Cited 30 March 2006.

[7] Bowers S.V. and Piety K.R., 'Proactive Motor Monitoring Through Temperature, Shaft Current and Magnetic Flux Measurements', INTERNET: http://www.compsys.com/ - Application Papers, Cited 28 May 2006.

[8] Daviu J.A., Guasp M.R., Folch J.R., Gimenez F.M. and Peris A., 'Application and optimisation of the discrete wavelet transform for the detection of broken rotor bars in induction machines', Applied and Computational Harmonic Analysis, Vol. 21, Issue 2, pp 268-279, September 2005.

[9] Elkasabgy N.M., Eastham A.R., Dawson G.E, 'Detection of Broken Bars in the Cage Rotor on an Induction Machine', IEEE Transactions on Industrial Applications, vol. 28 no. 6, pp 165-171, January/February 1992.

[10] Haji M., and Toliyat H.A, 'Pattern Recognition – a technique for induction Machines Rotor Broken Bar Detection', IEEE Transaction on Energy Conversion, vol. 16 no. 4, pp312-317, 2001.

[11] Hop D., 'The assessment of vibration produced in Squirrel Cage Induction Motors having cracked and/or broken bars', Master of Engineering Dissertation submitted at University of the Witwatersrand, July 1992.

[12] INTERNET: http://www.irispower/newsite/index.aspx?nav=CSMeter, Cited 14 May 2006.

[13] Kelk H. M., Milimonfared J., and H.A. Toliyat H.A., 'Interbar Currents and Axial Fluxes in Healthy and Faulty Induction Motors', IEEE Trans. on Industry Applications, Vol 40, No. 1, pp 128-134, January/February 2004.

[14] Kerszenbaum I. and Landy C.F., 'Investigation of the existence of significant interbar laminar currents in the three-phase in squirrel cage motors with rotor bar and/or endrings', The Transactions of the SAIEE, pp. 139 - 144, June 1983.

[15] Kerszenbaum I., 'The behaviour of three-phase squirrel cage induction motors with unbalance in the rotor; in particular two pole motors', Doctor of Philosophy Thesis submission at the University of Witwatersrand, July 1983

[16] Kerszenbaum I. and Landy C.F., 'The detection of broken bars and/or endrings in large squirrel cage induction motors', The Transactions of the SAIEE, pp. 22 - 27, July 1984.

[17] Kilbey Bill, 'Electric Motor Diagnostics Defect Frequencies and Data Collection Methods', INTERNET: http://www.compsys.com/ - Application Papers, Cited 30 May 2006.

[19] Kliman, G.B., Koegl, R.A., Stein, J., Endicott, R.D., and Madden M.W., 'Noninvasive Detection of Broken Rotor Bars in Operating Motors', IEEE Trans. on Energy Conversion, Vol. 3, No. 4, pp. 873 – 879, December 1988.

[20] Landy C.F., Reynders J.P. and Müller G.H., 'Condition Monitoring of Induction Motors', Electric Power Research Group, University of Witwatersrand, August 1996.

[21] Liang B., Iwnicki S.D., and Ball A.D., 'Asymmetrical stator and rotor faulty detection using vibration, phase current and transient speed', Mechanical Systems and Signal Processing, Vol. 17, Issue 4, pp 857-869, July 2003.

[22] McCully P.J. and Landy C.F., 'Evaluation of Current and Vibration Signals for Squirrel Cage Induction Motor Condition Monitoring', Proceedings of International Conference on Electrical Machines, pp 331 – 335, 1997.

[23] Menacer A., Mohamed-Saïd NAÎT-Saïd, Benakcha A/Hamid and Drid Saïd, 'Stator Current Analysis of Incipient Fault into Asynchronous Motor Rotor Bars using Fourier Fast Transform', Journal of Electrical Engineering, vol. 55, no. 5-6, pp 122-130, 2004.

[24] Milimonfared J., Kelk H.M., Nandi S., Minassians A. D. and Toliyat H.A., 'A Novel Approach for Broken-Rotor-Bar Detection in Cage Induction Motors', IEEE Transactions on Ind. Appl., Vol 35, No. 5, pp 1000-1006 September/October 1999.

[25] Müller G.H. and Landy C.F., 'Detection of broken rotor bars by axial vibrations produced in squirrel cage induction motors having interbar currents', South African universities Power Engineering Conference, pp 195 – 198, 1996.

[26] Müller G.H., 'A Novel Method to Detect Broken Bars in Squirrel Cage Induction Motors when Interbar Currents are present', Doctor of Philosophy Thesis submission at the University of the Witwatersrand, 1997.

[27] Müller G.H. and Landy C.F., 'Detection of Broken Rotor Bars in Squirrel Cage Induction Motors', Elektron, July 1998.

[28] Müller G.H. and Landy C.F., 'Detection of Broken Rotor Bars Part I – New Theory', Transaction of the SAIEE, pp 7-18, March 2003.

[29] Müller G.H. and Landy C.F., 'Detection of Broken Rotor Bars Part II – Experimental Verification', Transaction of the SAIEE, pp 19-28 March 2003.

[30] Müller G.H. and Landy C.F., 'Vibration produced in squirrel cage induction motors having broken rotor bars and interbar currents', Proceedings of International Conference on Electric Machines, pp 595-600.

[31] O'bannon Bob, 'Advanced AMS Machinery Manager - RBMview', INTERNET: http://www.compsys.com/ - Application Papers, Cited 28 May 2006.

[32] Pereira L.A. and Daniel da Silva Gazzana, 'Rotor Broken bar and Diagnosis in Induction Motors using Stator Current Signature Analysis and Fuzzy Logic', IEEE Industrial Electronics Society Annual Conference, pp 3019-3024, November 2004.

[33] Schoen R.R. and Habetler T.G., 'Effects of Time-Varying Loads on Rotor Fault Detection in Induction Machines', IEEE Transactions on Industrial Applications, vol. 31 no. 4, pp 900-906, July/August 1995.

[34] Schoen R.R., Lin B.K., Habetler T.G., Schlag J.H. and Farag S. 'An Unsupervised, On-line System for Induction Motor Fault Detection using Stator Current Monitoring', IEEE Transactions on Industrial Applications, vol. 31 no. 6, pp 1280-1286, November/December 1995.

[35] Siyambalapitiya D.J.T., McLaren P.G., and Acarnley P.P., 'A Rotor Condition Monitor for Squirrel cage Induction Motor', IEEE Transactions on Industrial Applications, vol. 23 no. 2, pp 334-340, March/April 1987.

[36] Sorensen Vern, 'Defining Analysis Parameter, Alarm Limit, & Fault Frequency Sets', INTERNET: http://www.compsys.com/ - Application Papers, Cited 15 June 2006.

[37] Tavner P.J. and Penman J., Condition Monitoring of Electrical Machines, New York: John Wiley & Sons Inc., 1987.

[38] Thomson William T. and Fenger Mark, 'Development of a tool to Detect Faults in Induction Motors via Current Signature Analysis', Iris Rotating Machine Conference, June 2002, San Antonio, TX - INTERNET: http://www.irispower.com/newsite/index.aspx?nav=techpaper; Cited 26 May 2006.

[39] Thomson William T. and Fenger Mark, 'Case Histories of Current Signature Analysis to Detect Faults in Induction Motor Drives' INTERNET: http://www.irispower.com/newsite/index.aspx?nav=techpaper; Cited 26 May 2006.

[40] Walliser R.F., 'An investigation into factors influencing the detection of broken rotor bars in single- and double-cage induction motors; with reference to interbar currents', Doctor of Philosophy Thesis submitted at the University of the Witwatersrand, 1993.

[41] Walliser R.F. and Landy C.F., 'Determination of interbar current effects in the detection of broken rotor cars in squirrel cage induction motors', IEEE Transaction on Energy Conversion, Vol. 9, No.1, pp. 152-158, March 1994.

[42] Zachas A., 'Evaluation of Heating Effects Due to Interbar Currents', Research Report submission for partial fulfilment for Master of Science degree at the University of the Witwatersrand, 2004.

Additional References

[43] Ayhan B., Chow Mo-Yeun, Trussell H.J. and Song Myung-Hyun, 'A Case Study on the Comparison of Non-parametric Spectrum Methods for Broken Bar Fault Detection', IEEE Industrial Electronics Society, Vol. 29, pp 2835-2840, 2003.

[44] Ayhan B., Chow Mo-Yeun and Song Myung-Hyun, 'Multiple Signature Processing-Based Fault Detection Schemes for Broken Rotor Bar in Induction Motors', IEEE Transaction on Energy Conversion, Vol. 20, No.2, June 2005.

[45] Botha M.M. – L H Marthinusen, Broken Rotor Bars, Elektron pg 27 -29, May 1993.

[46] Deng, X. 'Detection of rotor faults on induction motors by investigating the flux linkage of the stator winding', PhD Thesis, Aalborg University, Denmark, Dec. 1994.

[47] Dhuness, Kahesh, 'An investigation into aspects of the online detection of broken rotor bars in induction motors', Dissertation submission for partial fulfilment of the requirements for the Magister Ingeneriae degree at the University of Johannesburg, December 2006.

[48] EPRI, Electric Motor Predictive Maintenance Program, TR-108773-V2 Final Report, August 1999.

[49] Guru Bhag S. and Hiziroğlu Hüseyin R., Electric Machinery and Transformers, Third Edition.

[50] Lebaround A. and Bentounsi A., ‘Detection Improvement of the broken rotor bars of IM after supply disconnection’, Journal of Electrical Engineering, vol. 56, no. 11-12, pp 322-326, 2005.

[51] Penman J. and Stavrou A., ‘Broken rotor bars: their effect on the transient performance of induction machines’, IEE Proc.-Electr. Power Appl., Vol. 143, No. 6, November 1996.

[52] Schoen R.R., Habetler T.G., Kamran F. and Bartheld R.G. ‘Motor Bearing Damage Detection using Stator Current Monitoring’, IEEE Transactions on Industrial Applications, vol. 31 no. 6, pp 1274-1279, November/December 1995.

Associated Experimental References

[53] APPENDIX F: CMM CONSULTANTS EXPERIMENT REPORT

[54] APPENDIX G: IRIS POWER EXPERIMENT REPORT